Toward Cold Radical Chemistry with Cryogenic Buffer Gas Beams

by

M. I. Fabrikant

B.A., University of Nebraska Lincoln, 2007

A thesis submitted to the

Faculty of the Graduate School of the

University of Colorado in partial fulfillment

of the requirements for the degree of

Doctor of Philosophy

Department of Physics

2017

This thesis entitled:
Toward Cold Radical Chemistry with Cryogenic Buffer Gas Beams
written by M. I. Fabrikant
has been approved for the Department of Physics

Dr. Heather Lewandowski

Dr. Barney Ellison

Date

The final copy of this thesis has been examined by the signatories, and we find that both the content and the form meet acceptable presentation standards of scholarly work in the above mentioned discipline.

Fabrikant, M. I. (Ph.D., Physics)

Toward Cold Radical Chemistry with Cryogenic Buffer Gas Beams

Thesis directed by Dr. Heather Lewandowski

Creating cold molecular samples allows us to study chemical reactions that happen at temperatures characteristic of the interstellar medium. Additionally, cold environments can stabilize very reactive molecules like radicals, which can allow us to study difficult-to-observe reactions or intermediate states in the reaction process. Cryogenic buffer-gas beams (CBGB) have gained popularity as bright, low temperature molecular sources for spectroscopy and reaction studies. We have determined a method for efficiently loading a significant fraction of these new sources into a traveling-wave Stark decelerator, which uses time-varying inhomogeneous electric fields to decelerate polar molecules. We have also combined a CBGB with the decades-old technology of matrix isolation to create matrix isolated molecule samples, to help us achieve the goals of characterizing this new source and of investigating interactions of cold molecules .

Dedication

For my parents

Acknowledgements

This thesis could not have been written without the help of a network of scientists, craftsmen, and friends. I am particularly indebted to Dr. Lewandowski, who helped me devise this experiment, to Dr. Jonathan Weinstein, whose work kickstarted the theoretical ideas of this thesis, and to Dr. Gary Douberly, whose collaboration on the experimental side was timely and indispensable. I have also been extremely privileged to be able to discuss my research with my dad, Dr. Ilya Fabrikant, whenever what I'm doing happens to fall within his wheelhouse, and so I thank him for many crucially useful conversations over the course of some 25 years. I also thank him for his invaluable help with editing this thesis. The realization of the experiment should really be credited to the JILA support staff, namely the shop, whose employees Kyle, Todd, Kim, Tracy, Hans, and Blaine always figured out how to do the impossible, and who were very understanding about all the broken taps, drill bits, and saw blades. On the computational side, I have to thank Jim McKean who was similarly understanding about the times I crashed the yotta headnode. All of my work of course also builds and intertwines with that of my former and current labmates Noah, Travis, Yomay, John, Jason, Phillip, James, Kyle, and Cam, whom I thank for helpful conversations. Finally the companionship and support of my wonderful friends always helped me forget that physics existed at the right times, so particular thanks to Anne, who has always set such a good example for me, to Jon, who doesn't think he helped, but did.

Contents

Chapter

Tables

Table

Figures

Figure

Chapter 1

Cold Molecules

1.1 Motivations

The cooling of molecules to very low temperatures is a frontier of both physics and physical chemistry whose exploration promises to yield new insights into the physics of exotic environments and fundamental processes, as well as more practical progress toward study of basic chemical reactions, or measuring fundamental constants [1]. An entire field dedicated to cold molecules has sprung up in the past few decades with these goals in mind [2, 3, 4, 5, 6, 7].

1.1.1 Controlling Chemical Reactions

The collisions of cold atoms have long been an active area of study. As the techniques for cooling and trapping molecules and atoms improved, there has been a growth of interest in controlling atom-molecule and molecule-molecule interactions, both for the purposes of studying reactions in which the quantum state of each species was controlled, and to investigate the possibility of reactions that happen at low interaction energies, which are typically prohibited by an energy barrier. However, some reactions, like $F + H_2 \rightarrow FH + H$, are expected to proceed by tunneling at low energies, and might have large reaction rates at low temperatures [8][9]. Other reactions, such as the $CH + C_2H_4$ system [10] lack a barrier entirely, and have also been observed to have reaction rates that increase with lower temperature [11]. The enhancement of reaction rates in the former system depends on increased importance of the Van der Waals interaction between reaction partners, and can be observed only at temperatures of less than 0.2 K. In the latter

system, the barrier-less nature of the reaction manifests at temperatures of less than 10K, although there is some disagreement about the dependence of the rate coefficient on temperature[12] due to competing reaction pathways[13].

There are other avenues available for controlling the rate or outcome of a chemical reaction. For some time, there has been interest in using electric or magnetic fields to control products, filter reactants[14, 15], or directly influence how they interact by tuning parameters such as collision angle[16, 17]. Unfortunately, this is not possible above temperatures at which thermal motion of molecules either scrambles the selected quantum states or averages down the effect of the applied fields. However, below temperatures of about 1 K, the energy of the field interaction overcomes the translational energy of the molecules [18].

1.1.2 Relevance to the Interstellar Medium

The barrierless nature of many reactions relevant to cold chemistry has lead to the proposal that they dominate the neutral chemistry of dense interstellar clouds, whose temperature has been measured at 10-15 K [19]. Reactions in the interstellar medium of note include the formation of water from OH radicals interacting with hydrogen $OH + H \rightarrow H_2O$ [20], the creation of cyclic hydrocarbons [21], and the synthesis of molecular nitrogen[22].

$$N + OH \rightarrow NO + H$$

$$N + NO \rightarrow N_2 + O$$

This last reaction may play an important role in the eventual formation of the ammonia molecule (NH_3), which, in addition to being abundant in the ISM, can act as a useful diagnostic tool for measuring interstellar cloud temperature [23]. The temperatures of these clouds have the effect of stabilizing otherwise reactive molecules like free radicals and reaction intermediates [10, 24, 25]. The creation of environments on earth cold enough to sustain such intermediates would be valuable not only for replicating the chemistry of interstellar clouds, but also gaining insight into

the exact mechanisms and stages of chemical reactions. What is more, there is significant overlap between the chemistry of these intermediates and that of earth's upper atmosphere [26, 27, 28], so understanding this chemistry can have practical implications for processes like pollution and ozonolysis.

1.1.3 Fundamental Tests

In addition to chemistry considerations, molecules offer a convenient medium for the precision measurement of fundamental constants[29, 1] and values that test fundamental symmetries, most notably the electron dipole moment (EDM). Although the value of the EDM is very close to zero, narrowing the uncertainty of this value will give scientists the ability to rule out or confirm corrections to the standard model[30, 31, 32]. Any EDM measurement involves the application of an external field to an electron and measuring the shift of the electron energy eigenstate due to the interaction of its spin with the applied field. Compared to atoms, measuring the EDM of electrons bound to heavy polar molecules exponentially increases the sensitivity of the electron to the applied field, because of the large polarizability of the molecules[33]. Molecules are also useful as media for parity violation experiments and investigating Lorenz invariance[18]. For all of these applications, molecules must be cooled to increase as much as possible the coherence time of the prepared states.

1.2 Methods of production

Studying the systems described above presents several challenges to the experimenter. For any molecule of interest there must exist a detection mechanism, the ability to cool the molecule to the desired temperatures, and method of synthesis that can create the molecule in densities large enough to sustain cooling and detection. There are broadly two approaches toward satisfying all three of these critera- that of synthesizing molecules and cooling the molecules themselves (known as *direct* methods) and that of cooling atoms and assembling these atoms into cold molecules (*indirect* methods). These two approaches are somewhat complimentary, as the former, while successful in

creating molecules commonly found in nature, tends to reach temperatures of only a few K, whereas the latter method commonly reaches the ultracold regime of < 1 mK, but cannot be easily adapted toward the synthesis of chemically important molecules. Direct methods are making steady progress toward the ultracold regime, and are beginning to show promise for bridging the temperature gap. A selection of direct and indirect methods are outlined in more detail below.

1.2.1 Laser Cooling

Laser cooling has been a workhorse cooling mechanism for atoms for many years, and relies on translationally cooling particles by photon scattering. Traditionally, cooling molecules has proven much more difficult because of their rich internal structure, which prevents the existence of closed cycling transitions and necessitates the use of many repump lasers to pump molecules out of dark states [34]. This technique has been successfully employed for CaF [35], SrF [36], and YO[37], among others. Recently, the use of microwaves to mix dark rotational states with states that can be repumped has drastically simplified the laser cooling of YO molecules [38]. The temperatures reached by these methods can be as low as few hundred mK [39], demonstrating that direct methods can reach the ultracold regime.

1.2.2 Feshbach Resonance Assisted Association

Currently the ultracold regime is dominated by molecules assembled from ultracold atoms. Instead of cooling molecules directly, atoms are laser cooled and combined by tuning the response to either an optical or magnetic interaction to coerce the atoms into a bound state[18]. The technique has been successfully used to create ultracold samples of KRb[40, 41], LiCs[42], and Na_2[43] to name a few. Clearly, the disadvantage of this method is that only alkali and alkaline-earth atoms may be used as the molecular constituents, producing molecules that have only abstract relevance to natural chemistry. However, the samples produced are in high density and can be as cold as 100 nk [18, 2, 7].

1.2.3 Supersonic Expansion and Buffer Gas Beams

Supersonic expansion relies on forcing molecules to undergo many collisions with a noble gas atom in order to convert internal rovibrational energy into translational kinetic energy. Typically, this is accomplished by seeding a reservoir of noble gas with the molecule of interest and forcing it through a nozzle, usually 1-2 mm in size, into vacuum. The molecules collide inelastically with the atoms to reach rovibrational temperatures [5] of a few K. This process often happens in pulses, which reduces the gas load on the vacuum chamber. The parameters of reservoir pressure and temperature, aperture geometry, and choice of noble gas may all be varied to achieve different results. A schematic is shown in 1.1.

Figure 1.1: A schematic of the supersonic expansion process. Figure from [5].

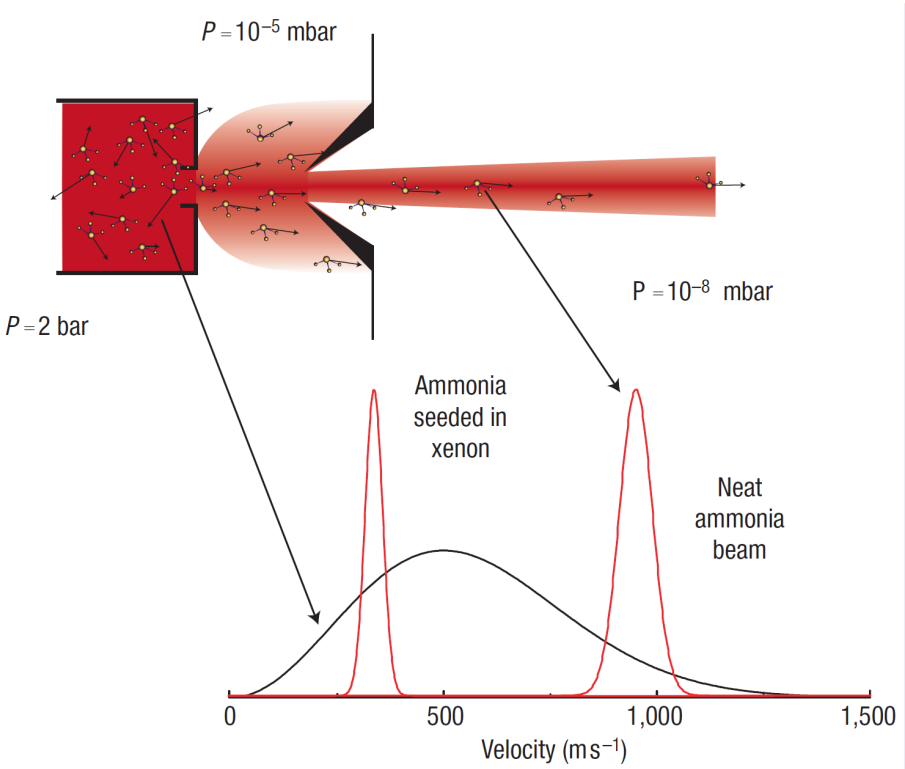

The result of this process is a beam of rovibrationally cold molecules with large longitudinal velocity. This velocity, which changes according to the type of noble gas used, is usually a few hundred m/s, which can limit interrogation times and make subsequent trapping nearly impossible.

The experiment must either stop the molecules while at the same time preserving their density and low temperature, or must find some other way to interrogate them for long enough times to achieve good signal to noise.

Buffer-gas beams were developed in part to address the disadvantages of large longitudinal velocities, and are one of the most intuitive methods of creating a beam of rovibrationally cold molecules. For this method, a volume is held at approximately the freezing temperature of a noble gas (a schematic is shown in Fig.1.2). This same noble gas is allowed to flow through the volume while the molecule of interest is introduced and allowed to thermalize with the noble gas. In the past, the most popular noble gas used was helium[44], as it reaches the coldest temperatures, but neon has recently emerged as an attractive buffer gas because of the ease with which it can be pumped. If lower temperatures are required, an additional cell stage can further cool the beam [45]. Molecules can be introduced into the cell via ablation, molecular beam insertion, capillary insertion, or discharge etching [46], although this thesis will focus only on ablation. The buffer-gas cooling method is suitable for a large variety of molecules, as long as the collision cross section between the molecule and buffer gas is large enough, and as long as the molecules can be introduced into the cell efficiently, and such that the method of introduction (such as ablation or injection) does not heat the molecules (either translationally or internally) so much that they can no longer be cooled to useful temperatures.

Figure 1.2: A schematic of the buffer gas cooling process. Figure from [47] Molecules are introduced via ablation into a cryogenically cooled cell filled with buffer-gas. The molecules thermalize and are entrained in the buffer-gas flow to create a cold molecular beam. Other methods of molecule insertion are available but not shown.

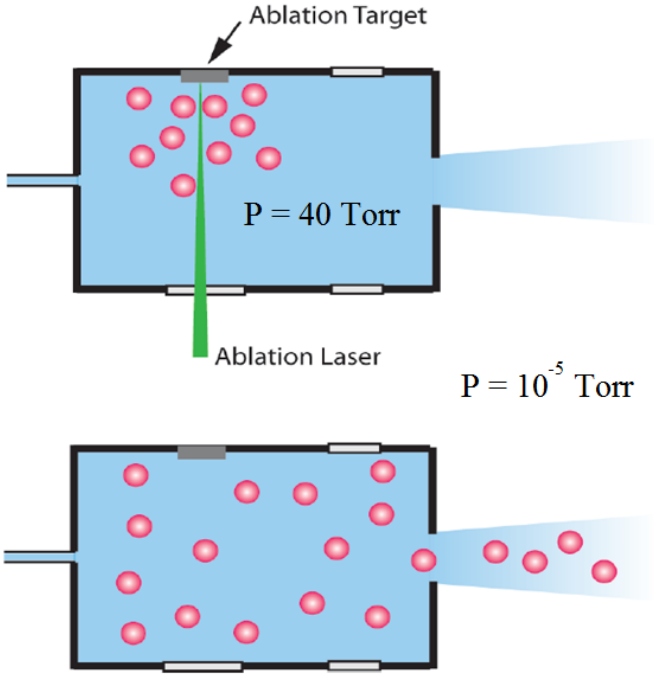

The velocity of a molecular beam produced by this source can, in principle, be much slower than that produced by a supersonic expansion. The range of possible velocities is large, as demonstrated by beams of NH_3 created at 130 m/s[48], whereas beams of CaH molecules have been created with velocities of just 40 m/s. However, it is often necessary to decelerate even a beam with this small of a velocity.

1.2.4 Merged Beam Experiments

One way to deal with large molecular velocity is not to reduce it at all. If the interaction partner of the molecules is set up as a beam of nearly co-propagating molecules, then the collision energy can be tuned to very small values by tuning the collision angle[49]. Even though no deceleration occurs, guiding apparatus must still be employed to preserve the molecule phase space. This

method is exploited by [50, 51, 52] and has successfully been employed to look at interactions of CH[53],H_2[54] to collision energies as small as 10 mK[55].

1.2.5 Deceleration

If a merged beam experiment is not suitable, molecular beams must be decelerated. Magnetic or electric fields are constructed in such a way that they create potential hills that reduce the kinetic energy of molecules riding up them.

Figure 1.3: A cartoon of the process of Stark deceleration. The ideas for magnetic and electric deceleration are the same- inhomogeneous fields acting on the electric or magnetic dipole moment of a particle create a potential hill that the particle must climb, thereby losing kinetic energy. Figure from [56].

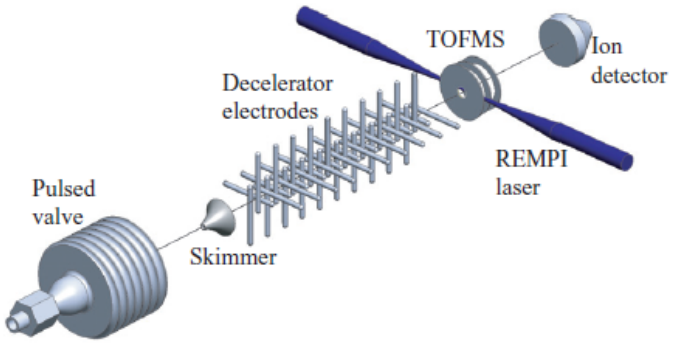

There are several options for doing this, depending on what molecule is to be decelerated, and on what "molecular handle" (i.e. magnetic or electric dipole) is to be used [57, 54, 58]. Deceleration is appropriate for a wide range of molecules, and to date been used for OH[59, 60, 61], NH[62, 63], ND_3[64, 56], among others. In principle molecules of any dipole moment to mass ratio can be decelerated given a long enough apparatus, but molecules with ratios of at least 0.08 Debye Amu^{-1} can be slowed with decelerators on the order of a meter long, (depending on the speed of the source). A disadvantage of these techniques is that the fields used are conservative and cannot compress the phase-space of the molecular distribution. This means that no internal cooling takes place,

and any temperature reduction of the translational degrees of freedom of the molecular packet is due to rejection of translationally hotter molecules. It is therefore necessary for molecules to be rovibrationally cold before deceleration, in order to fully reap the benefits of a cold, slow molecular sample.

1.2.6 Helium Droplets and Matrix Isolation

In contrast to methods that create rovibrationally cold molecules in beams to be detected with gas phase spectroscopy, there also exist methods which, although not technically gas phase, can achieve comparably cold samples whose detection signatures are similarly narrow in linewidth. These methods include capturing molecules in helium droplets [65, 66] and freezing them in solid matrices [67, 68, 69]. In particular, matrix isolation can completely "freeze" out the rotational modes of a molecule at the cost of coupling it to the trapping potential of a noble gas matrix, and somewhat shifting its electronic and vibrational modes. On the other hand, helium droplets can lower the temperatures of *all* the degrees of freedom of a molecule to as low as 0.4 K [65], compared to only a few K for the coldest molecular hydrogen (H_2, D_2, and HD) matrices [70]. Trapping molecules in helium droplets and matrix isolation are uniquely useful for stabilizing reactive molecules that would otherwise be difficult to detect spectroscopically[71]. We choose to make use of the matrix isolation method and will discuss it more extensively in Ch.5.

1.3 This Thesis

This thesis will present progress along two separate paths toward the ultimate goal of combining two of the methods discussed in this chapter- the coupling of a buffer-gas beam into a Stark decelerator. The buffer-gas beam remains a relatively novel molecular source, and its potential to create a variety of species for the purposes of investigating molecule interactions remains largely unexplored. Our work has shown that the buffer-gas source is promising for creating bright, slow beams of molecules that could be electrostatically trapped if combined with a decelerator. After giving an overview of our molecule of interest, this thesis will explain how we use simulations to

determine the best method of adapting this novel source to the inherent limitations of the Stark decelerator. The following chapters will document the our successful implementation of a buffer-gas beam in our lab and our construction of an intermediate experiment that can detect the molecular beam output of the buffer-gas cell, as progress toward decelerating and trapping it.

Chapter 2

The CH molecule

2.1 Motivations for using CH

Because our group creates diffuse beams of cold molecules, any physics/chemistry we investigate will be most relevant in the interstellar medium (ISM). We therefore often focus on molecules that are abundant in the ISM, and are especially interested in unstable molecules that are difficult to study or may not exist under normal (hot, dense) conditions. CH is important as an observed constituent of the ISM, a free radical, and a simple hydrocarbon. As a radical, CH is difficult to create in the laboratory, but plays an important role in interstellar medium chemistry and combustion chemistry: CH participates in archetypical reactions such as hydrogen exchange with deuterium[72]

$$\mathrm{CH}(X^2\Pi) + \mathrm{D_2} \rightarrow \mathrm{CD}(X^2\Pi) + \mathrm{HD}, \tag{2.1}$$

the formation of more complex hydrocarbons [73]

$$\mathrm{CH} + \mathrm{H_2} \rightarrow \mathrm{CH_3} + h\nu, \tag{2.2}$$

and simple combustion reactions [53]

$$\mathrm{CH}(X^2\Pi) + \mathrm{C_2H_2} \rightarrow \mathrm{C_3H_2} + \mathrm{H}$$

$$\mathrm{CH}(X^2\Pi) + \mathrm{C_2H_2} \rightarrow \mathrm{C_3H} + \mathrm{H_2}$$

In contrast to chemistry that is more relevant to that which occurs on earth, two-body barrierless reactions such as eq.2.1 are expected to be dominant in the ISM[74]. CH reactions have been studied in merged beam experiments [10], and at temperatures as low as 23 K [75], but those experiments did not achieve the simultaneous low temperatures and low translational velocities needed to be able to control the interaction energies and study these reactions.

2.2 CH structure

The structure of CH has been known for some time from astronomical observations [76], and is shown in Fig.2.5. We will focus primarily on the $X^2\Pi$ ground state, which has orbital configuration $1\sigma^2 2\sigma^2 3\sigma^2 1\pi^1$. The coupling of angular momenta in the CH ground state will have implications for both our ability to decelerate and detect it. For many polar molecule ground states, these couplings are well described by Hunds case a), shown in Fig.2.1. Because we are dealing with a linear polar molecule in a Π state, the total electronic orbital angular momentum cannot be conserved. However, the linear nature of the molecule means that the *axial* component of the orbital angular momentum L *is* conserved, by symmetry. Therefore, although L is not a good quantum number, its projection onto the internuclear axis, Λ, is. What is more, if the spin-orbit interaction is relatively strong, the total spin S will tend to precess about the internuclear axis, meaning that both S and Σ will be conserved. Finally, the rotation of the molecule about its center of mass will produce another angular momentum R, which will combine with $\Omega = \Lambda + \Sigma$ to give the total angular momentum J.

Figure 2.1: The coupling of angular momenta for Hund's case a). From [77]

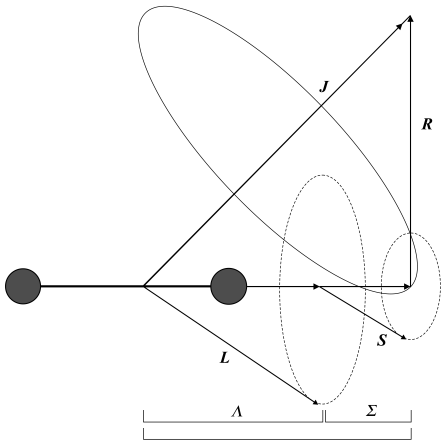

However, for the CH ground state, the spin-orbit coupling is actually very weak, and is therefore better described by Hunds case b), although it will be useful to consider both representations when we analyze the effect of electric fields on the molecule.

Figure 2.2: The coupling of angular momenta for Hund's case b). From [77]

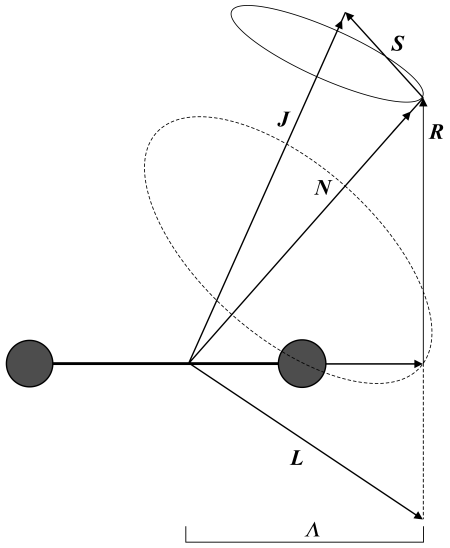

In the B case, because of the weak $L - S$ coupling Ω is no longer a good quantum number. Instead L couples with the rotation R to form N, which couples with S to form J. To summarize the coupling scheme for Hund's case B:

$$\mathbf{R} + \mathbf{L} = \mathbf{N}, \qquad N = 1, 2, 3...$$

$$\mathbf{N} + \mathbf{S} = \mathbf{J}, \qquad J = N - 1/2, N + 1/2,$$

$$\mathbf{J} + \mathbf{I} = \mathbf{F}$$

The good quantum numbers for CH are then Λ, N, S, J, I, and F. Therefore we can write the rotational level splittings (or fine structure) as [77]

$$F_1(N) = B_\nu \left((N+1)^2 - \frac{\sqrt{(4N^2 + Y(Y-4))}(N+1))}{2} \right)$$
$$F_1(N) = B_\nu \left((N+1)^2 - \frac{\sqrt{(4N^2 + Y(Y-4))}N)}{2} \right),$$

where B_ν is the rotational constant, A is the spin-orbit constant, and $Y = A/B_\nu$. In many papers, (including our own [78]) it is common to refer to the fine structure of the CH ground state as containing, say, $^2\Pi_{1/2}$ or $^2\Pi_{3/2}$ states, and although this is not incorrect, it is a little confusing, since Ω is not defined and it would make more sense to group the fine structure levels by N [77]. A picture of the fine structure, from [77] is show in Fig.2.3 and shows the grouping of levels into integer N, with each level being split by the spin-rotation coupling.

Figure 2.3: The fine structure of CH, from [77], showing the spin-rotation splitting of the lower lying N states.

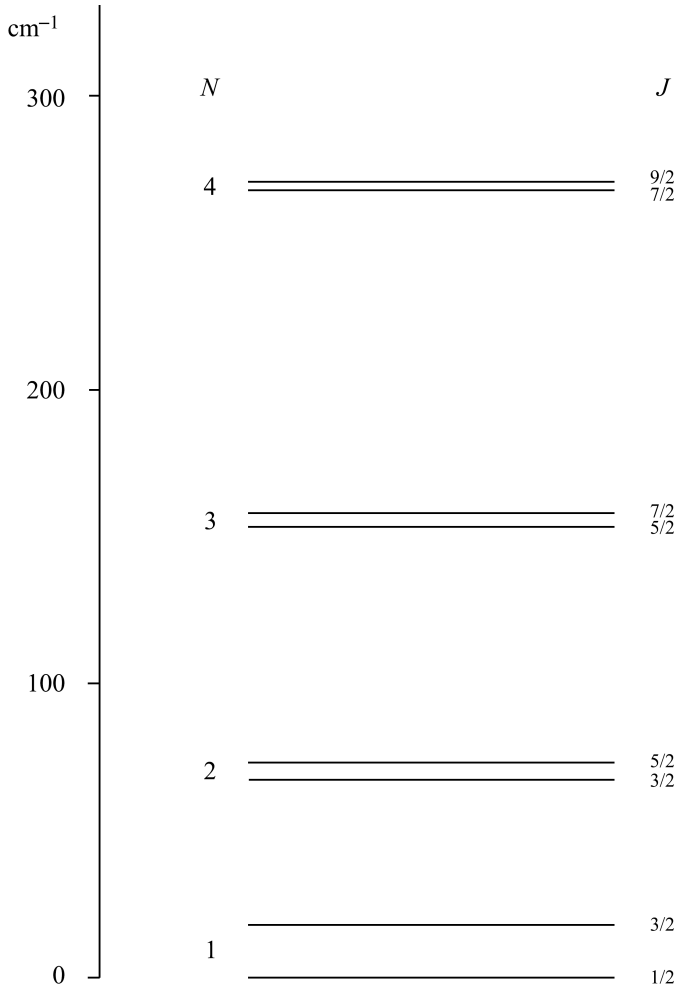

Because L can be either aligned or anti-aligned with the internuclear axis, the projection Λ can have two signs, only one of which we would be able to decelerate. In CH, the coupling of L with the rotation R further splits each of the fine structure states in Fig.2.3 into two Λ -doublets. A Stark manifold is shown in Fig.2.4. It is clear from the figure that only the state whose energy decreases with higher $\mathbf{E}$ is suitable for deceleration and trapping, since the other will simply fly into the high voltage electrodes and be lost.

Figure 2.4: The Stark manifold of CH showing the stark shift for each of the Λ doublet states in the $J = 1/2$ branch of the rotational ground state.

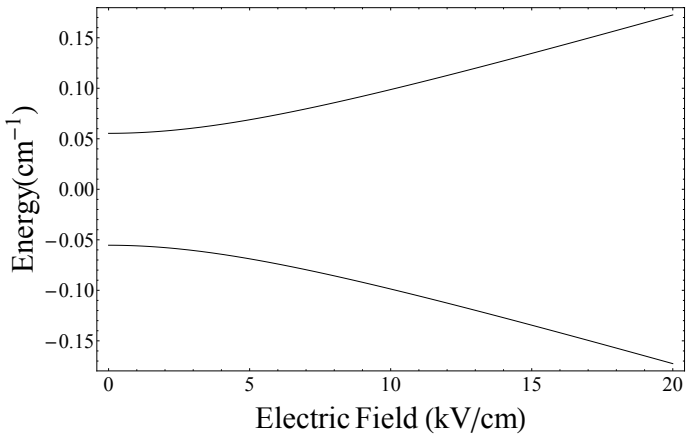

2.3 CH detection

The electronic potential energy surfaces were measured by [79] and are shown in Fig.2.6. This structure of CH lends itself to several state-selective detection methods. The first category might be labeled state-selective absorption, either via direct absorption spectroscopy or cavity ring-down spectroscopy. Both the A←X and B←X transitions have been used for absorption spectroscopy [78, 80], but if both laser wavelengths are available, the B←X is preferable, because of the superior Franck-Condon overlap, evident in Fig.2.6. In addition to absorption, a laser induced fluorescence can also take advantage of these two transitions [81].

Figure 2.5: Experimentally measured electronic level structure of CH. Minimum electronic energy values are from [82]. The ionization energy of 10.64(1)eV (85817 cm^{-1}) is not shown.

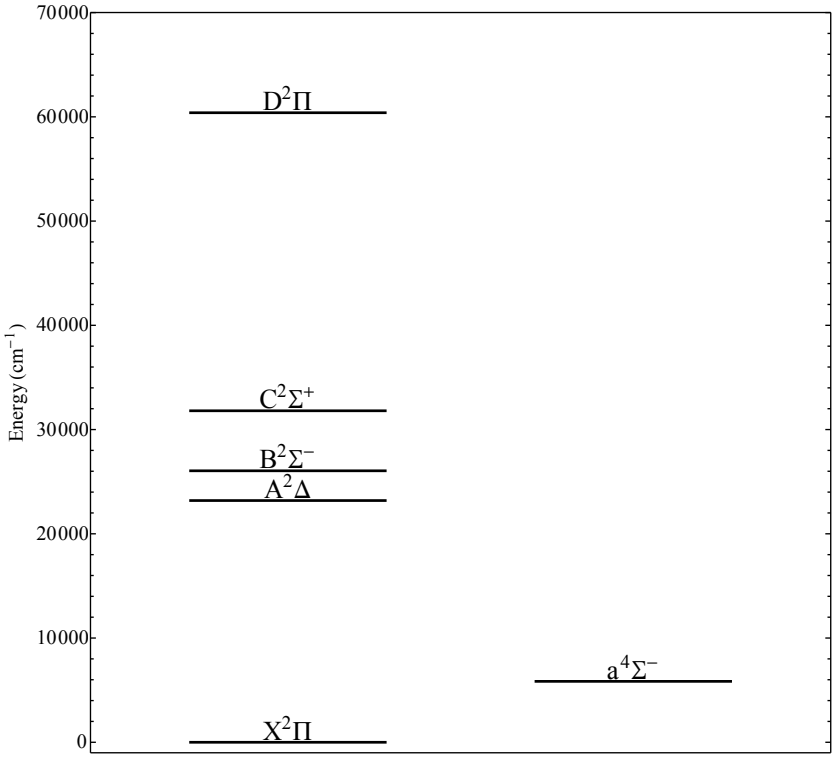

State	Minimum Electronic Energy T_e (cm^{-1})	Vibrational Constant ω_e (cm^{-1})	Rotational Constant B_e (cm^{-1})	Centrifugal Distortion D_e (cm^{-1})
$X^2\Pi$	0	2858.5	14.457	0.00145
$a^4\Sigma^-$	5844	3145	15.4	
$A^2\Delta$	23189.8	2930.7	14.934	0.00154
$B^2\Sigma^-$	26044	1794.9	12.645	0.00222
$C^2\Sigma^+$	31801.5	2840.2	14.603	0.00156
$D^2\Pi$	60394		13.7	

Table 2.1: A summary of the available experimentally measured diatomic molecule constants for the CH electronic levels shown in Fig.2.5. Values from [82]

.

Figure 2.6: potential energy surfaces of CH. Note that the equilibrium distance for the X and B states are extremely close, resulting in a large Franck-Condon overlap. The ionization energy of 10.64(1)eV (85817 cm^{-1}) is not shown. Figure from [79].

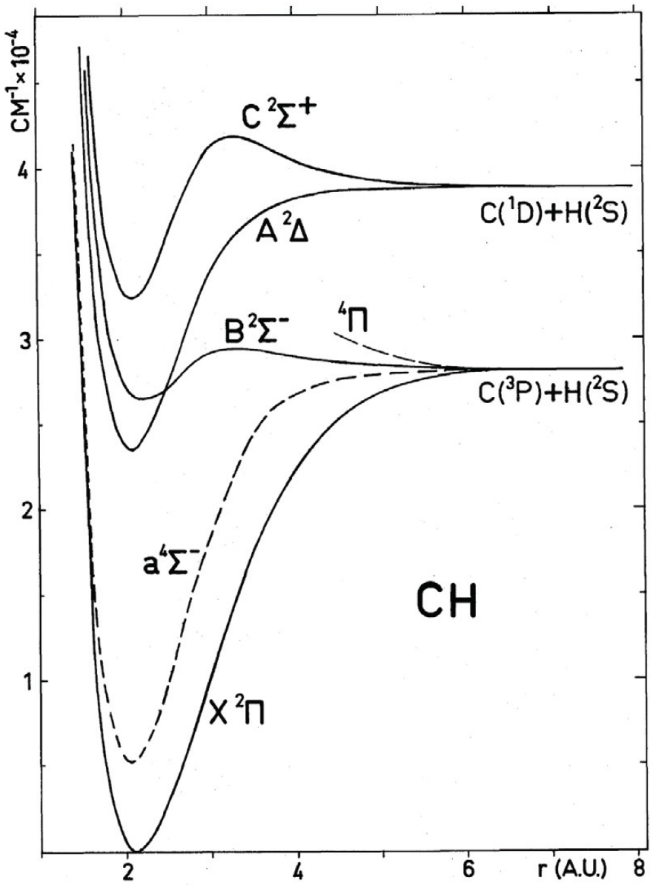

Another method that exploits electronic transitions is resonance enhanced multiphoton ionization (REMPI). Ionization schemes can be very attractive because of possible large signal to noise enhancement, since the collection efficiency, once molecules are ionized, approaches 100%. [83, 84] take advantage of such a method by using both the C and D levels as intermediate states. If the D state is used, the C state is very close to halfway in energy toward the D state, meaning that the first photon in a 2+1 REMPI scheme would be near resonant with it, causing an enhancement in the signal [84]. Our group has spent some time developing and improving on a source of 118 nm (10.5eV) light, which has been used to detect other molecules with 1+1' REMPI [85, 86]. In

this case, a primary excitation to either the A or B states may be used, combined with subsequent ionization by the 118nm photon.

As we will see below, a "quick and dirty" method that serves to simply confirm the presence of CH is to create CH in a highly excited state an observe the fluorescence to the ground state (either from the A or B state) with a visual spectrometer. However, as this method is not state selective, we use it only as a diagnostic tool.

In addition to exploiting the electronic and rotational structure, CH also has one vibrational mode at 2861 cm^{-1}[87]. This will be discussed further in ch.5.

2.4 Making CH

From a naive perspective, it might seem that making CH should not pose too much of a challenge, since hydrocarbons are so ubiquitous. However, because CH is so reactive, the real challenge comes when one tries to make CH from one of these materials in high enough densities to detect with the available methods.

2.4.1 Electrical Discharge

Since CH has three lone electron pairs and is extremely reactive, the best way to make it is one which involves breaking apart a stable precursor, (although other methods, such as formation as the product of a chemical reaction, have been successful [88]). One of the easiest ways to break apart molecules is by electrical discharge. Discharge works by placing molecules inside a large electric field, accelerating many electrons (and in turn, ions), from one discharge plate to the other, bombarding the molecule with energy and breaking it apart[89]. Because the energy distribution is not narrow or selective in any way, there is no way to predict what molecules are made other than empirically.

We attempted to make CH this way, using methane (CH_4) as a precursor, based on the work of [90]. We constructed a small vacuum chamber containing an electrode that could be charged to several kV. We tried the DC method first, in which charge builds up on the discharge electrodes

until the breakdown voltage is reached, as well as a pulsed discharge, in which voltage is applied for only a few tens of microseconds. The advantage of the second method is that the breakdown happens more predictably, and we can trigger our spectrometer off the high voltage pulse in order to reduce noise. This chamber was filled with methane (CH_4) after which a DC voltage was applied to the electrodes. The resulting fluorescence was observed with an Ocean Optics visible spectrometer.

Figure 2.7: Visible spectrum of the discharge of methane. The lines at 431 nm from fluorescence of CH from the A to X state show that some CH is being produced, but very inefficiently, as we creating both C_2 and electronically excited hydrogen.

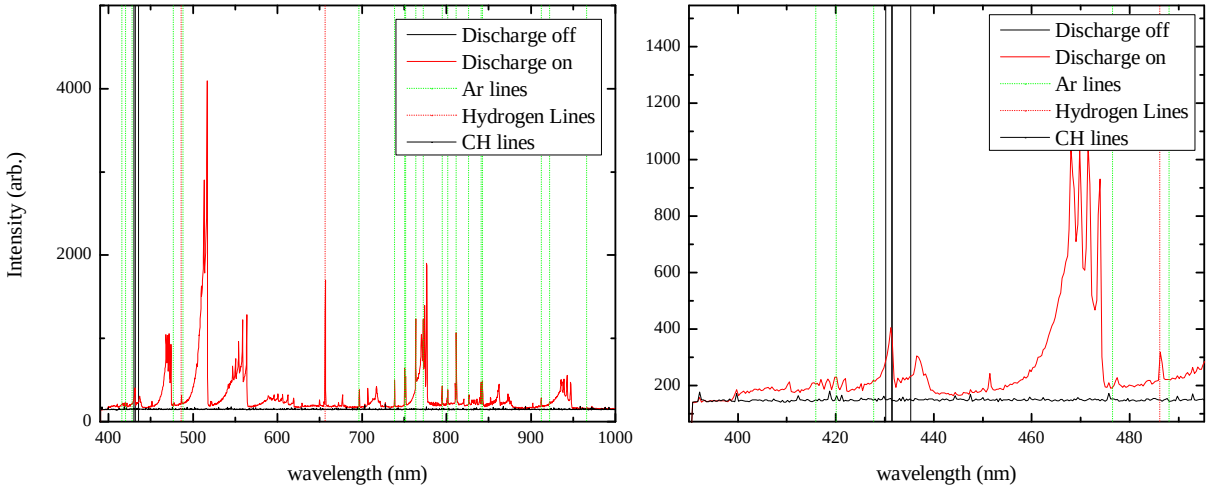

The peaks at 431 nm clearly show the presence of CH. However, the spectrum is dominated by the peaks in the 400-600 nm region, which are the "C_2 Swan System", see (Fig.2.8) [91]. Since we are making C_2, it is clear that this is at best an inefficient method for making CH, since we are dumping enough energy into the methane to break all of the C-H bonds and allow the C atoms to react with each other to create excited states of C_2.

Figure 2.8: The Visible spectrum of C_2, from [91].

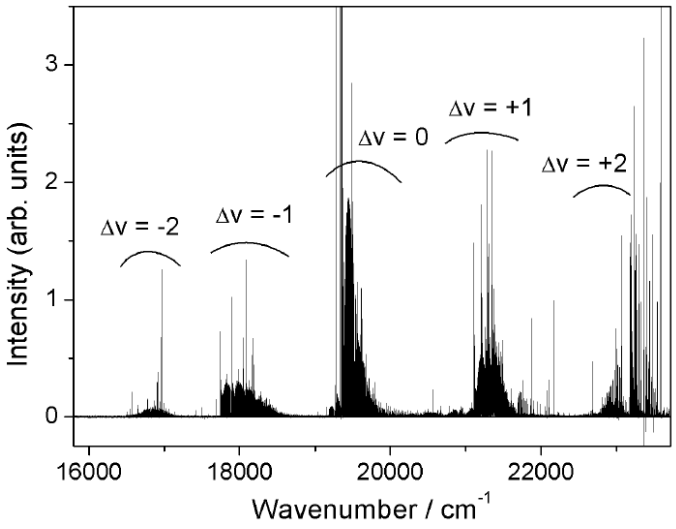

2.5 Dissociation of Haloforms

Most CH sources use haloform molecules as precursors [92, 93, 94]: these are methane molecules in which three of the four carbon atoms have been replaced with halogens (ie, of the form HCX_3). The thinking behind using haloforms is that the lone hydrogen atom is strongly bound to the carbon atom, compared to the relatively weak halogen bonds. For instance, the bond strength of C-H is 80.86 kcal/mol, whereas for C-Br it is only 67 kcal/mol. The expectation is therefore that the halogen bonds will break preferentially, generating higher densities of CH.

We investigated both the discharge and photolysis of bromoform, which has been used in [93]. For both methods we prepare a mixture of bromoform in argon by heating it to 60°C, which results in a 4% gaseous mixture. This is flowed through a pulsed valve and is either discharged at 1kV, or flows through a quartz capillary upon which is focused a 193 nm excimer laser firing at 10mJ/pulse. In both cases we were able to observe the fluorescence with a visual spectrometer, and both processes yielded similar results, shown in Fig.2.9. It appears once again that these are very inefficient processes which dump energy unnecessarily into the creation of C_2, although we again do make some CH.

Figure 2.9: Visible spectrum of the discharge of bromoform. 5 mL of bromoform was heated to 60°C creating a vapor pressure of 40 Torr in 4psig of Ar (a 4% mixture). The duration of the discharge pulse was 100 us, at 1 kV

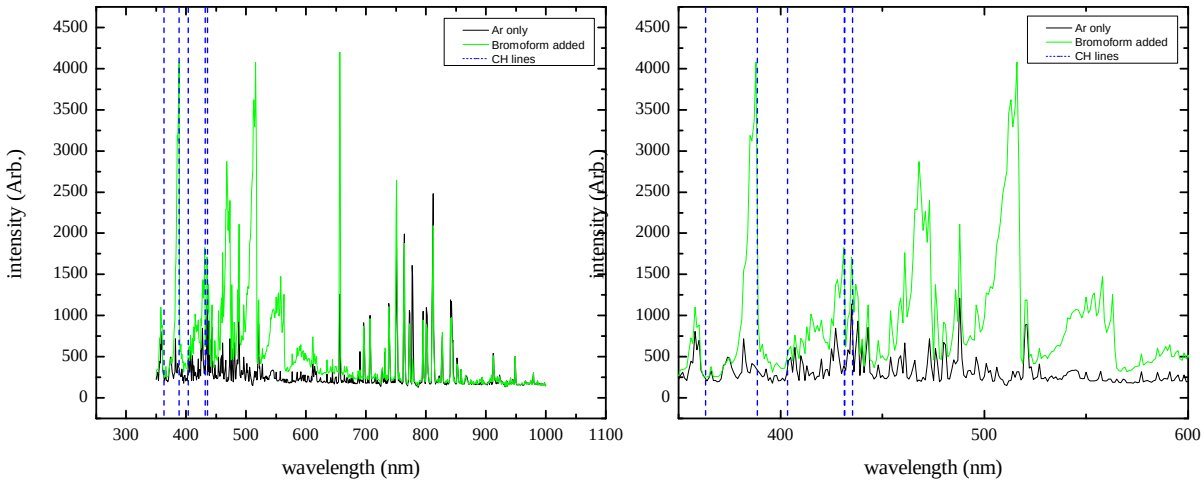

Our collaborators in [78] had the most success making CH by ablating the precursor CHI_3 (iodoform). The bond strength of C-I is only 50 kcal/mol, so in principle it should yield even higher densities of CH when dissociated. Iodoform is usually synthesized as a yellow powder and can therefore be difficult to form into an ablation target. It is possibly for this reason that they did not have much success with iodoform in its pure form. However, when our collaborators dissolved the iodoform in acetone, covered the beaker in aluminum foil, and let the concoction sit on a shelf for several months, the resulting substance (which "had the consistency of day-old chewing gum"), when ablated with a a 532 nm laser at 100 mJ/pulse in a buffer-gas cell yielded high enough densities to detect via absorption spectroscopy of the B←X transition.

Figure 2.10: Spectra of $X^2\Pi(v'' = 0, N'' = 1, J'' = 1/2)$ cryogenic CH molecules. The main figure shows the Q-branch transitions; the frequency offset is 25723.4 cm^{-1}. The inset shows the P-branch transition plotted on the same scale; its frequency offset is 25698.2 cm^{-1}. The spectra were obtained from 1 to 2 ms after the ablation pulse. The experimental measurements are shown as points, the fit to a Gaussian (two Gaussians, in the case of the Q-branch transition) is shown as a solid line. The data were taken at a cell temperature of 5 K, ablation energy of 0.1 J, and helium buffer gas density of 1×10^{16} cm^{-3}.

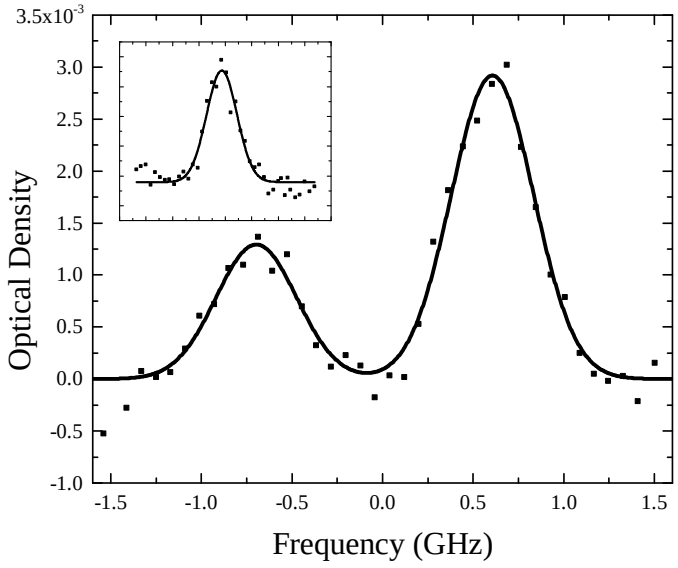

We have since managed to recreate this CH precursor "goo" (Fig.2.11, and happily on a much shorter timescale than months. After dissolving the iodoform in acetone and covering with aluminum foil, the mixture may be heated to increase the reaction of I_2 with the aluminum. The black substance that is created is "gooey" because of remaining moisture, probably water dissolved in the acetone. If the mixture is heated gently at about 90 C it can be reduced to a hard glassy substance that is much more vacuum friendly (since it outgasses less).

Figure 2.11: A picture of the CHI_3 ablation precursor, glued to a copper plate and ready for cell installation.

From the data in Fig.2.10, we were able to conclude that we created 10^{11} CH molecules in the upper lambda-doublet state. They created these molecules in a buffer-gas cell (with no extraction aperture) with volume $10 \times 10 \times 2.5\ cm^3$, which works out to $N = 4 \times 10^8 mol/cc$ assuming uniform cell density.

Chapter 3

Simulations of Stark Deceleration of Buffer-Gas Beams

3.1 Stark Deceleration

Although buffer gas beams show great promise for creating bright beams of cold molecules, in order for our group to exploit these beams for collision experiments and for us to be able to compare them directly with their supersonic expansion predecessors, we need to be able to couple them into a Stark decelerator [1] . We therefore propose the experiment represented in Fig.3.1 which loads a buffer gas beam source into a Stark decelerator. We use CH as our candidate molecule in simulations, since in addition to the other interesting qualities discussed in this thesis, its dipole moment of 1.46(6) D[95] is very close to that of the Lewandowski group workhorse deceleration molecule NH_3 (1.42 D).

[1] Portions of this chapter were previously published in [78]

Figure 3.1: Proposed experiment for decelerating and trapping buffer gas beams. The use of these beams creates the opportunity for many detection methods at different stages of the deceleration process.

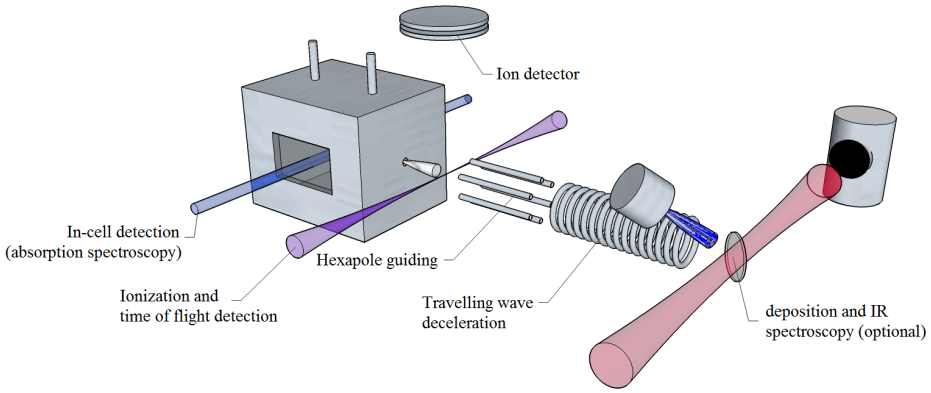

Since the processes by which molecular beams are cooled often cause them to acquire a large translational velocity, [5] they must be decelerated to rest before trapping experiments can be performed. Our group does this with the use of Stark decelerators, which rely on the Stark shift (Eq.3.1) of a molecule to create a longitudinal potential hill, which removes translational energy from the beam.

$$U_{stark} = \pm\sqrt{(\frac{\Delta U_{inv}}{2})^2 + (|\overrightarrow{\mu}||\overrightarrow{E}|\frac{MK}{J(J+1)})^2} \mp \frac{\Delta U_{inv}}{2} \tag{3.1}$$

Historically, this has been done with pulsed Stark deceleration, whereby pairs of charged rods create stark potential hills directly in front of the molecular packet, a schematic of which is shown in Fig.3.2[5].

Figure 3.2: Schematic of the pulsed deceleration process. From [96]

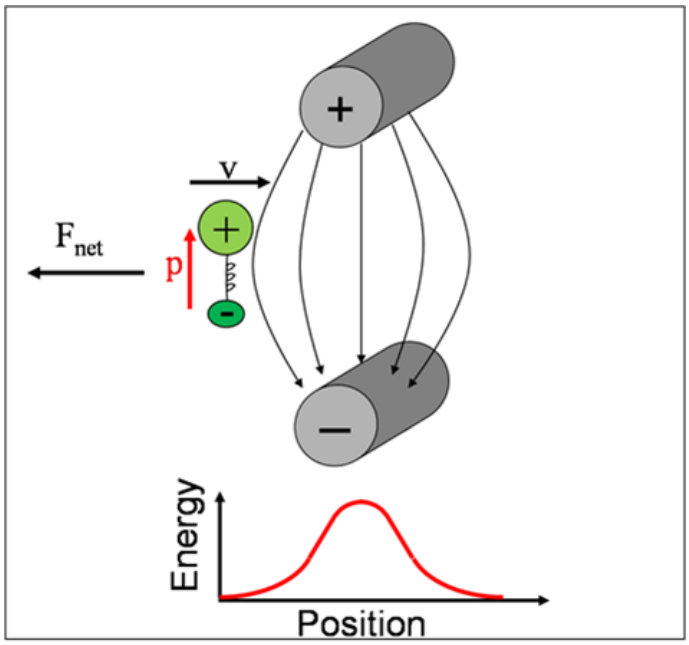

As the packet rides up these hills, the potentials on the rods are switched so that the packet is always losing energy. The rods have the effect of squeezing the packet in alternate transverse dimensions, so that the transverse Stark potential averages out to a confining transverse potential. However, as the molecule packet slows down and spends more and more time between rod pairs, it has more opportunities to "leak out" through the sides, causing large losses in molecule number, not just from lack of confinement but because of active transverse over-focusing by the electrodes.

For this reason, our group has been working for several years on a "traveling wave" Stark decelerator (TWD), which uses 8 sets of charged rings (Fig.3.3) to create a longitudinal potential well Fig.3.4, which slows down continuously, effectively causing molecules to ride up a long potential hill until they are stopped at the end of the decelerator.

Figure 3.3: A travelling wave decelerator uses rings instead of rods to slow molecules. The rings are grouped into sets of eight such that each set creates a longitudinal potential well.

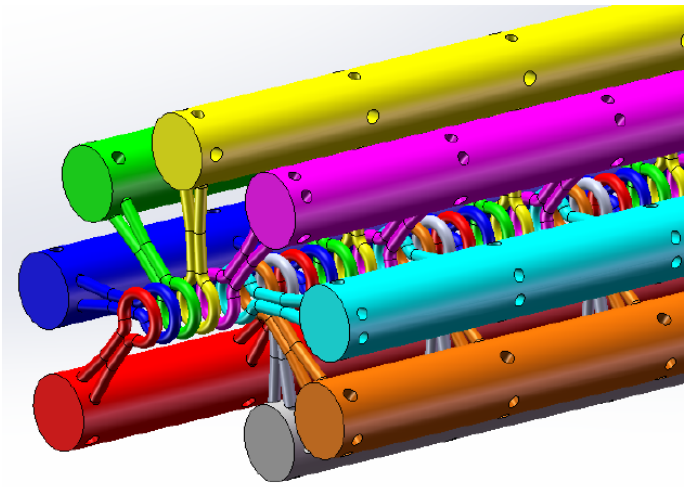

Our decelerator is designed such that the potential on each electrode will be given by

$$U_n = U_a sin\left(\frac{2\pi n}{8} - \omega t\right), \tag{3.2}$$

where U_n is the potential on electrode i, $U_a = 12\ kV$. This configuration creates the Stark potential shown in Fig.3.4, and the time dependence ensures that this potential well moves down the decelerator with a speed that matches the incoming molecule velocity v, so long as the applied frequency ω satisfies

$$\omega = \frac{2\pi v}{8d}, \tag{3.3}$$

where d is the ring spacing.

Figure 3.4: Longitudinal potential

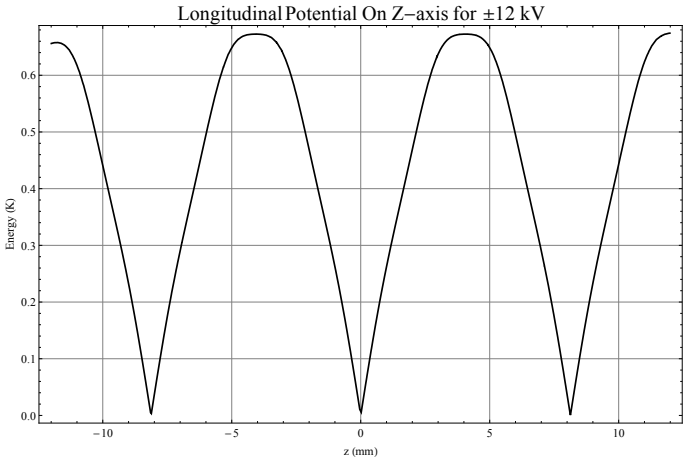

Because every 8th electrode is connected to the same rod, the potential well is repeated many times over the length of the decelerator, meaning that molecules could be trapped in any of these wells at a time. The wells move in unison down the decelerator as the phases of each sine wave on the electrodes are varied. A consequence of this is that the decelerator can sustain only a narrow range of longitudinal velocities. To illustrate this further, I show a picture of the longitudinal phase space (Fig.3.5) of our decelerator, which shows the "separatrix," or the phase space trajectory which separates molecules bound by the potential wells in Fig.3.4 from those that are not trapped.

Figure 3.5: The bound longitudinal phase-space volume created by the TWD potentials in Fig.3.4. We see that to be captured a particle must not only be physically inside the moving potential, but that each well supports only a finite range of particle velocities.

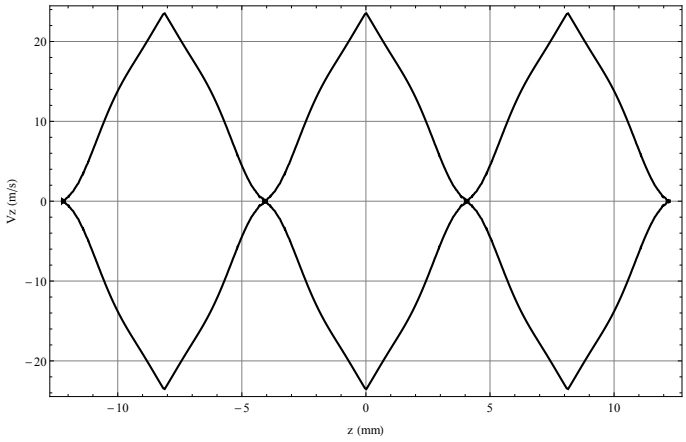

We see that molecules that are exactly matched to the longitudinal movement of the well will sit in the well center, whereas those within a small range of this velocity will oscillate within the well. However, if the velocity of the molecule becomes too large or too small, it will ride over the potential from one well to the next, and will not be effectively decelerated.

Because the electrodes are now rings, the molecules would see a true transverse trapping field at all times, so that we would expect transverse losses from such a decelerator to be much smaller. We illustrate this by showing a *transverse* separatrix of the TWD in Fig.3.6

Figure 3.6: transverse separatrix of the TWD, from [96]. Because this separatrix is not constant with longitudinal position Z, we show slices where Z is at the center of a ring ("ring-aligned"), halfway in between rings ("gap aligned") and the average of both.

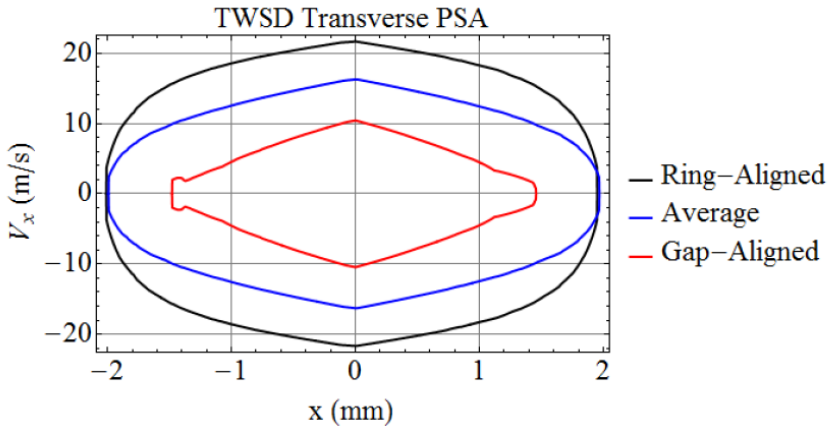

As of this writing, the mechanical aspects of this decelerator have all been assembled, but the electronics have yet to be perfected. Therefore, while this is happening, we have endeavored to test the efficacy of this decelerator with simulations.

The material differences between slowing a supersonic beam and a buffer gas beam arise from their different phase space distributions. To illustrate this, we show a typical phase space distribution of a buffer-gas beam compared to the more standard alternative of supersonic beams in Fig.3.7.

Figure 3.7: Comparison of the longitudinal phase space distribution for a supersonic beam vs a buffer gas beam. The distributions on the right show what the molecule phase space looks like after traveling through a field-free region.

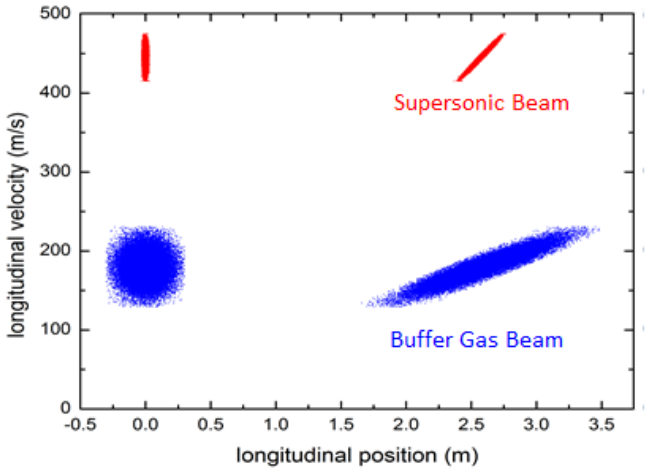

We see that the buffer-gas beam's initial phase space is much more extended in space and (relatively) in velocity. The large spatial extent of the beam is a consequence of the large cell aperture required for good extraction. In addition, to prevent a hydrodynamic boost [5], there should not be too many collisions near the aperture of the cell. This has the effect that the relative velocity spread of the beam is large. These large spreads pose a coupling problem, as the TWD can only accept a narrow range of velocity classes a time.

We choose to solve this problem by noticing that after the beam undergoes free flight, the packet of molecules deforms in phase space (Fig.3.7), since fast molecules increase their distance with respect to the average molecule, and the slow ones lag behind. This causes the phase space of the packet to rotate and stretch out, with the upshot being that the velocity width of a part of the packet at any given point tends to 0 with larger freeflight time, (although the total velocity width stays the same). If the packet were allowed to undergo freeflight for a long time and then enter the decelerator, molecules entering at any time would be all of a single velocity class. Mitigating the transverse expansion that the molecules undergo during this free flight requires the addition of hexapole guiding.

As discussed above, the velocity acceptance of the decelerator is a consequence of the movement of the Stark potential wells along the decelerator. This means that as TWD slows molecules down, the accepted velocity decreases. Since our goal is to accept many different velocity classes into the decelerator, the cleverest way to do this would be to slow the molecules down such that the accepted velocity of the decelerator at any given time was equal to the velocity of the entering molecules. This is represented schematically in Fig.3.8

Figure 3.8: Cartoon schematic of the acceptance method. The vertical line in each panel marks the position of the TWD. In the first panel the molecule packet exits the source. At time t_1 it has evolved in free-flight such that particle velocity is correlated with particle position, and the instantaneous velocity width is small. At time t_2 the fast part of the packet has been accepted and decelerated, by which time the entering molecules have matching velocity. The process repeats until the entire packet enters the decelerator.

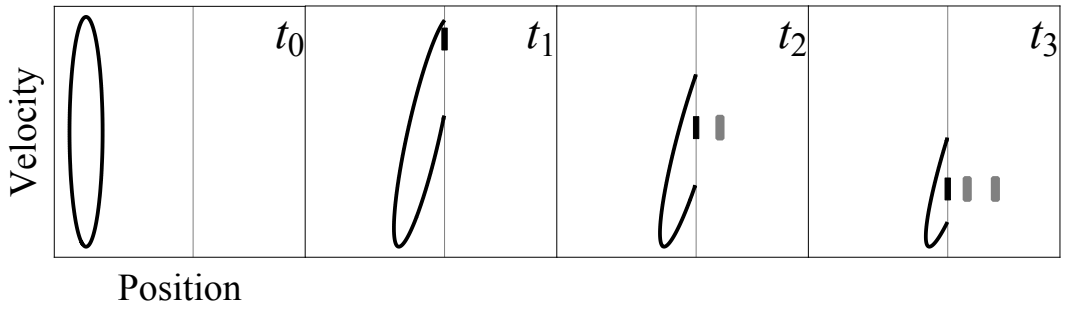

To aid our mathematical formulation of the acceptance, we define an "acceptance function" A(t) that determines the central accepted velocity of the decelerator. The acceptance function which describes the process of Fig.3.8 is that which matches the velocity of the molecules as they arrive, namely

$$A(t) = H/t \tag{3.4}$$

where H is the length of the hexapole (the distance that molecules travel under the influence of no longitudinal fields). Although this acceptance method is ideal, it poses some problems. For one, the acceleration that the molecules undergo, given by the time derivative of the acceptance

function, starts out as very large. When the molecules experience large accelerations, the shape of the potential well in the rest frame of the molecules deforms. The shape of the well acquires a linear offset, shown in Fig.3.9:

Figure 3.9: Comparison of the TWD potential well for two deceleration magnitudes.

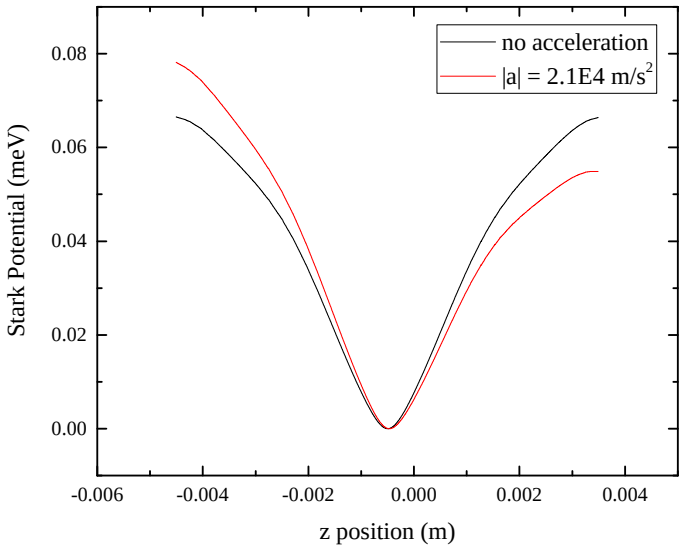

Intuitively this linear offset may be explained as the same thing that happens when running with a cup of coffee. If you manage to run at a constant velocity with the coffee and then try to stop too quickly, the coffee sloshes over the front rim of the cup, and the number of coffee molecules is diminished, potentially devastating the day's caffeine intake. The coffee cup can only sustain small accelerations; the same is true of the TWD potential well. Any constant acceleration applied to the well is the result of a constant force, which creates a linear potential that deforms the well and causes the effective well depth to decrease.

We also can illustrate the problem of large accelerations by looking at the phase space generated by these potentials. We look specifically at the "separatrix," or the phase space trajectory that marks the boundary between trapped orbits ("phase stable") and orbits in which the molecules simply travel over the wells and through the decelerator (phase unstable). Fig.3.10 shows separatrices for the same accelerations as those in fig.3.9:

Figure 3.10: Comparison of TWD separatrices for two deceleration magnitudes: $|a| = 0$ (larger curve), and $|a| = 2.1 \times 10^4$ m/s^2 (smaller curve).

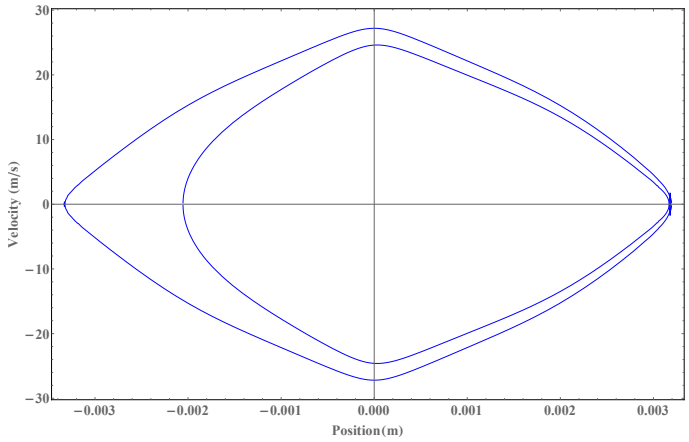

As the acceleration increases, the available phase space volume will decrease, and fewer molecules will be phase stable. It may therefore be advantageous to use a more standard linear deceleration scheme that approximates the nonlinear version.

For a deceleration method in which the acceleration experienced by the molecules was constant, we might guess that the best acceleration to use would be the smallest acceleration that is sufficient to bring the molecule to the desired velocity within the declerator, i.e. one that satisfies

$$a = \frac{V_f^2 - V_i^2}{2S} \tag{3.5}$$

where V_f and V_i are the final and initial velocities and S is the decelerator length. However, since the molecule packet contains molecules with many initial velocities, the choice of V_i is not trivial. We now let V_i be the velocity of an "index molecule", whose velocity becomes the central accepted velocity of the potential well. The velocity of the wells and the index molecule would then be given by

$$V(t) = -a\left(t - \frac{H}{V_i}\right) + V_i \tag{3.6}$$

We refer to Eq.3.6 as the linear "acceptance function", in contrast to the nonlinear acceptance

function $V = H/t$. We can get an idea of the limiting acceptance functions and their associated accelerations by plotting V_a for several different index molecules, shown in Fig.3.11:

Figure 3.11: Comparison of linear and nonlinear acceptance functions. The linear acceptance function is sufficient to decelerate a 210m/s index molecule, which is 3σ above the center velocity and therefore puts an upper limit on the acceleration required. The inset shows the deformation of the potential well experience by the molecules at different times.

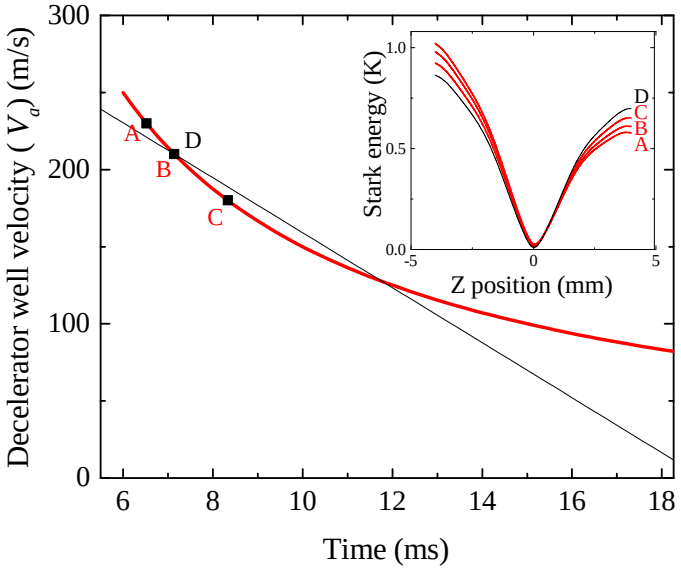

3.2 3D Monte Carlo simulations

In order to determine which deceleration schemes work best, we generate 3 dimensional potentials for 24kV sine waves on the decelerator electrodes using a commercial finite element solver (COMSOL[2]), and use these to evolve trajectories of molecules with randomly generated initial phase space coordinates.

The decelerator electrodes are modeled in COMSOL as a string of donut-shaped electrodes. This is actually an approximation- in fact the electrodes are shaped more like hairpins with a circular bulb at the end (Fig.3.12). This is because the electrodes are made by bending and then

[2] COMSOL Multiphysics, version 4.3, www.comsol.com

electropolishing tantalum wire. The surfaces of these electrodes have to be mirror-smooth to avoid electron field emission on any protruding points. If we somehow tried to bend the tantalum wire into more of a tennis racket shape, we would not be able to ensure good surface quality at the junction. The hairpin shape introduces a defect in the transverse Stark potential.

Figure 3.12: TWD decelerator electrodes.

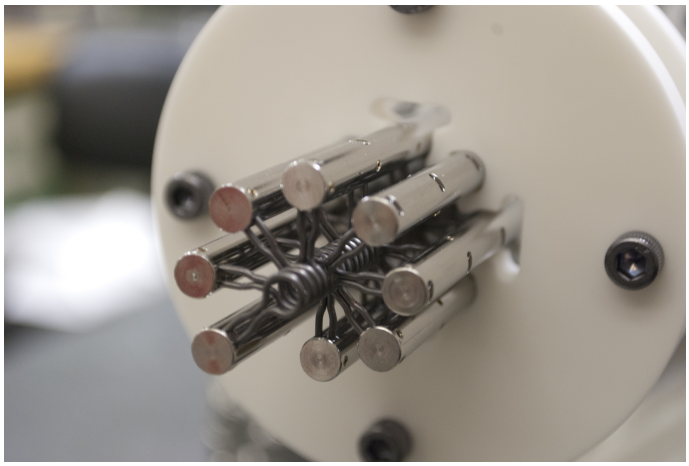

In the actual decelerator design, the hairpin "pinch" spirals around the longitudinal axis, which in principle should average out the transverse Stark potential defect. Simulations run by Nicholas Farrow show that this defect does indeed have almost no consequences for molecular dynamics simulations of our decelerator. His results are reprinted in Fig 3.13. We can be especially confident that the defect is unimportant because the agreement of the cylindrically symmetric and asymmetric COMSOL models does not get worse with smaller velocity, which we would expect if it were important, since the average transverse potential would become a poorer and poorer approximation as the time spent by the molecules withing each electrode increased.

Figure 3.13: Comparison of time-of-flight signals from molecular dynamics simulations of our decelerator using cylindrically symmetric electrode models and more realistic "hairpin" shaped models. From [96].

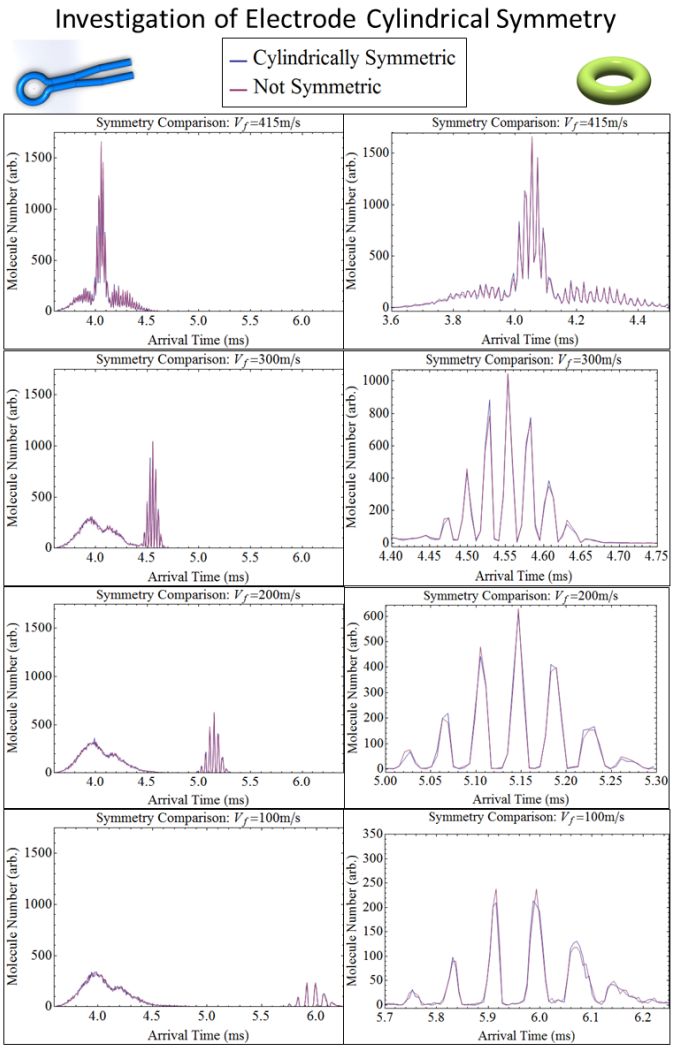

These initial molecule distributions are 6 dimensional Gaussians. We choose the widths in every dimension to be characteristic of typical buffer-gas beam parameters. We also run simulations for supersonic expansion beams for comparison; the parameters for both types of distributions are listed in Table 3.1.

Parameter	Buffer Gas Beam	Supersonic Beam
Average Forward Velocity	180 m/s	445 m/s
Longitudinal Velocity Spread	17 m/s (1σ)	10 m/s (1σ)
Longitudinal Position Spread	10 cm (1σ)	10 mm (1σ)
Transverse Velocity Spread	21 m/s (1σ)	1 m/s (1σ)
Transverse Position Spread	1.7 mm (1σ)	1.0 mm (1σ)

Table 3.1: Parameters of the buffer-gas beam used in simulations. The expansion out of the cell is assumed to be in the hydrodynamic regime. These parameters would correspond to a cell extraction time of about 2 ms and a cell aperture diameter of roughly 5 mm for a physical cell [47].

3.2.1 Hexapole Parameters

In contrast to the decelerator, we use analytical potentials for the hexapole part of the simulation, where the voltage on the hexapole is set to 400V. The dependence of preserved molecule number on the hexapole voltage was only briefly investigated and was found to increase at small voltages but to then quickly plateau. This is because the hexapole can only preserve the distribution of molecules in phase space, but cannot compress it. Because of the large aperture of the buffer-gas cell, many molecules will simply start outside of the decelerator phase space acceptance, and attempting to fit them inside it, either by collimating or focusing the molecular beam, will merely trade a large velocity spread for a large position spread or vice versa.

This point can be illustrated with a mini-simulation that includes only the initial Gaussian distribution being loaded into an analytial hexapole potential. Coupling into the decelerator is simulated with a hard radial cutoff at the end of the hexapole. In Fig.3.14, we show the results of such a simulation, which counts the number of surviving molecules at the end of a hexapole as a function of hexapole voltage. We see that the number increases steadily with voltage as the available phase space volume is filled, but then plateaus when the molecules being loaded into the hexapole contain too much energy to exhibit stable trajectories inside the hexapole phase space. Full simulations which include the decelerator, although too computationally expensive to run at

a similar resolution, show a similar leveling-off behavior with hexapole voltage.

Figure 3.14: Results from a small simulation sending a beam of molecules through an analytical hexapole potential, for several hexapole lengths. The number of molecules increases until the phase spaces are as well matched as possible, after which the number oscillates while the maximum number stays flat. The oscillation is a consequence of defocusing near the end of the hexapole, an its frequency depends on how the average radial distance of molecules varies with length. Since molecule trajectories will undergo more oscillations in a longer hexapole, the surviving molecule number varies more rapidly with voltage.

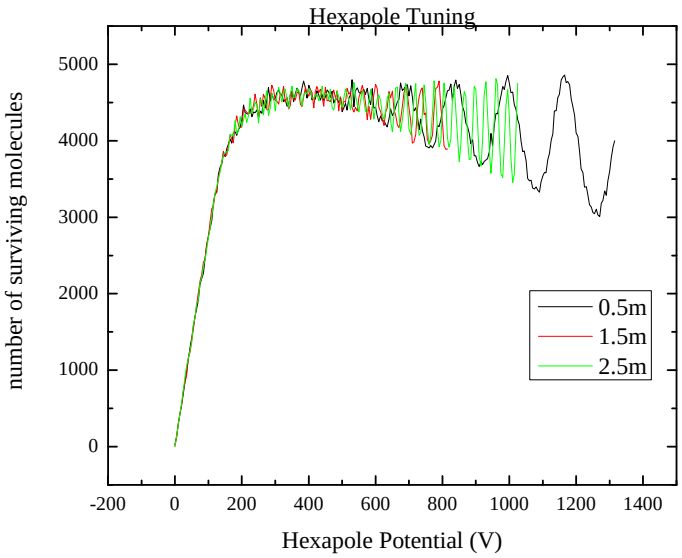

Armed with the results of Fig.3.14, we set the hexapole voltage to 400V, judging that this is comfortable above the "shoulder" of the plateau. This parameter was set for all simulations that included the decelerator. The result of one of these "full" simulations is shown in Fig3.15. As the molecule trajectories are evolved, any given molecule can meet with three different fates: it can hit an electrode, fly radially outward until it is too far away to ever be recaptured by any of the potentials, or it survives until the simulation times out. When any of these events happens, the phase-space coordinates of that molecule are frozen for the rest of the simulation.

Figure 3.15: A snapshot of the final phase space for decelerating molecules from 180m/s to 25m/s using a hexapole length of 1.5m

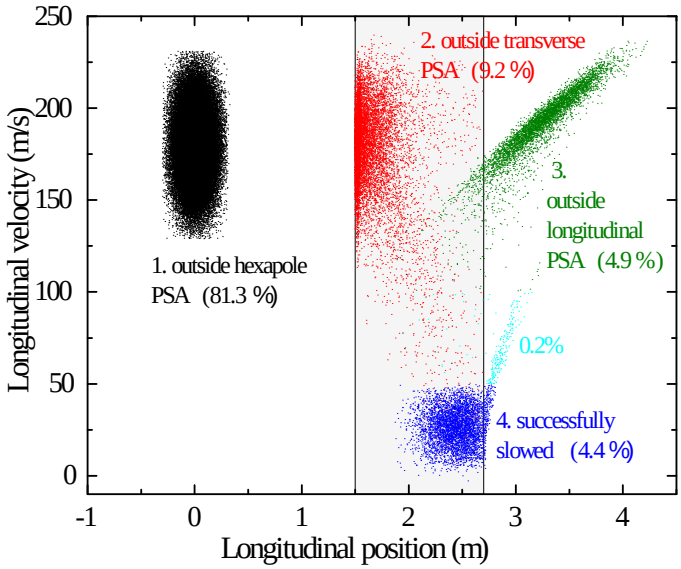

Fig.3.15 shows that most molecules are lost at the cell aperture. Because of the large aperture sizes necessary for efficient molecule extraction, most molecules start outside the hexapole phase-space and cannot be compressed into it, so this loss is inevitable and can really only be addressed with a larger diameter hexapole and decelerator. Another chunk of molecules is lost from out-of-phase loading of molecules into the wells. When this happens, molecules slosh from one well to the other instead of being decelerated, and to first order exhibit phase-space "rotation" similar to particles traveling through a field-free region.

We can also use these trajectories to extract simulated time-of-flight (TOF) signals, which is what we would measure in the lab. A TOF trace is shown in Fig.3.16, with the TOF of a supersonic beam simulation shown for comparison.

Figure 3.16: Times of flight for deceleration of buffer gas and supersonic beams. The relative signal heights of the two simulations should be ignored (although each simulation is internally consistent)- both simulations were run with the same number of molecules, whereas in the lab each source produces different numbers of molecules per pulse in different densities.

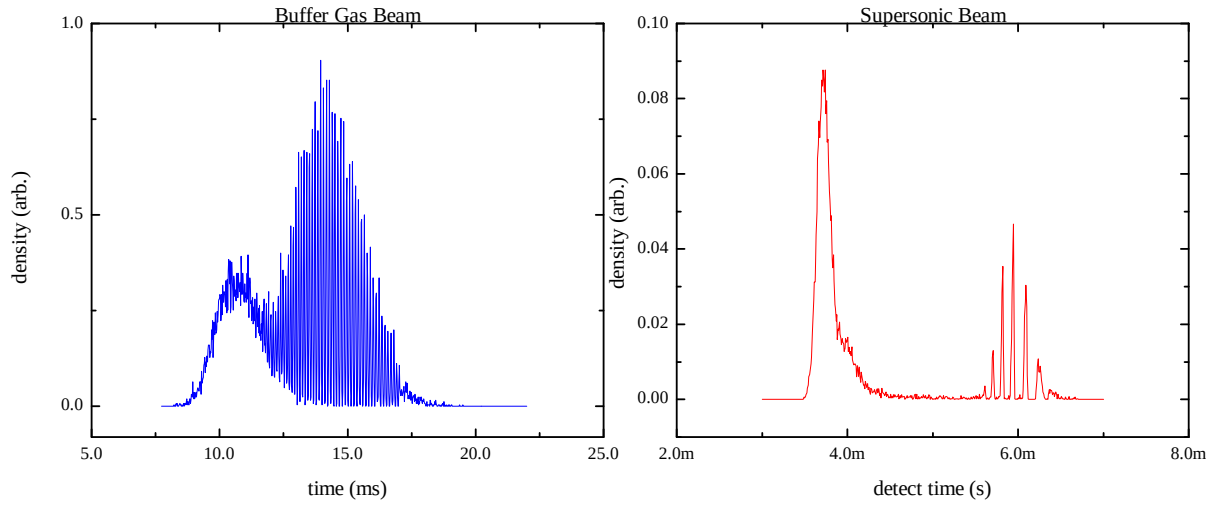

At early times, a glut of "unslowed" molecules is detected- these are the green molecules from Fig.3.15. At later times, the slowed molecules appear. It seems at first glance that the separation of slowed and unslowed molecules is worse for buffer gas beams, but in fact this is because the large velocity spread of the initial beam is mapped to a large position spread in the decelerator, which causes the molecule packets to fill a large time interval upon detection. The width in time for each individual well is about the same for both beams; there are just so many filled wells that the entire space between slowed and unslowed molecules is filled for the buffer gas beam case.

3.3 Theoretical Model

Because of the symmetry of this new type of decelerator, it is natural to question whether, despite good agreement with results in the past [97], the large computational cost of a three dimensional simulation is really necessary. For the previous generation of pulsed decelerators, agreement with 1D simulations has been poor [98] because of strong coupling between the transverse and longitudinal coordinates, and because of the poor suitability of using an averaged transverse

potential at slow velocities. The ring decelerator obviates the need to think about these problems, which suggests the suitability of constructing a theoretical model for acceptance.

We base the 1D model on the overlap between the phase-space distribution of the packet(PSD) and the phase-space acceptance (PSA) of the decelerator. We model the PDA as a bivariate gaussian distribution $G(z, V_z, t)$, where z v_z are longitudinal position and velocity variables. The number of molecules withing the PSA of the decelerator can be approximated by

$$n = \int_{V_a - \Delta v/2}^{V_a + \Delta v/2} G(H, V_z, t_0)\ dV_z(t_0), \tag{3.7}$$

where Δv is the width of the decelerator acceptance in the velocity coordinate. This width is not constant and changes as a function of the acceleration used, because of the well distortion discussed above. The acceleration a is the time derivative of $V_a(t)$ the accepted velocity at a given time.

To determine the size of Δv we compute the separatrix for different accelerations from $a = 0$ ("bunching") $a = -100\ \ km/s^2$ - the largest acceleration required to decelerate a molecule that was 3σ faster than average in the time allowed by a decelerator that was 624 rings long. To compute a separatrix, we use the following reasoning: the separatrix describes the largest *closed* phase-space trajectory. Because all the fields we are dealing with are conservative, these trajectories are constants of the hamiltonian, meaning the energy should not change along them. Therefore we can write

$$E = \frac{1}{2} m V^2 + U(z) \tag{3.8}$$

And solving for V gives:

$$V(z) = \pm \sqrt{\frac{2}{m}(E - U(z))} \tag{3.9}$$

These two functions of z, which we will call $V(z)_+$ an $V(z)_-$ are defined up to the energy constant E. If we vary the energy until the two halves of the function become continuous, i.e.

require that

$$min(V(z)_+) = max(V(z)_-) \tag{3.10}$$

Once E is determined then $\Delta V/2$ is given by

$$\int_{z_{min}}^{z_{max}} V(z)_+ \frac{dz}{z_{max} - z_{min}} \tag{3.11}$$

Figure 3.17: The velocity acceptance width shown as a function of acceleration

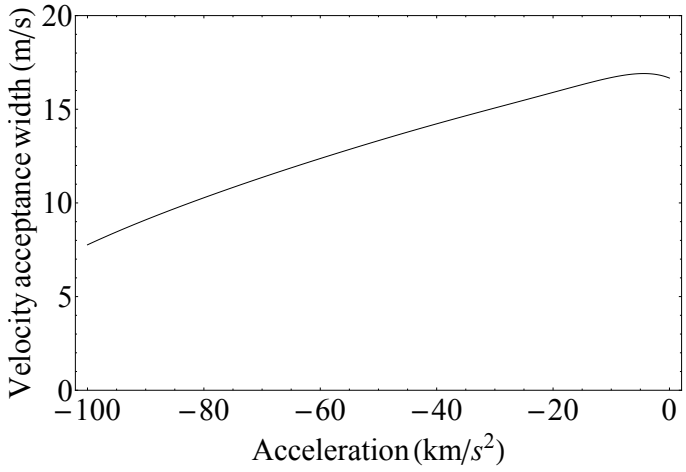

As far as acceptance in the *position* coordinate z, molecules can be accepted over a range of positions, but we approximate it as happening only at the decelerator entrance. To show this visually, we compare an actual separatrix (in this case for bunching) to the model separatrix in Fig.3.18.

Figure 3.18: Comparison of separatrices used in the simulations (blue) to those model approxiation (red). Both separatrices are superimposed on the PSD of the molecular packet after it has undergone 1m of free flight. The inset zooms in on the two separatrices showing that the model really is an approximation, since it sweeps continuously through the entering packet in position, an since the velocity width is averaged velocity width of the simulation separatrix.

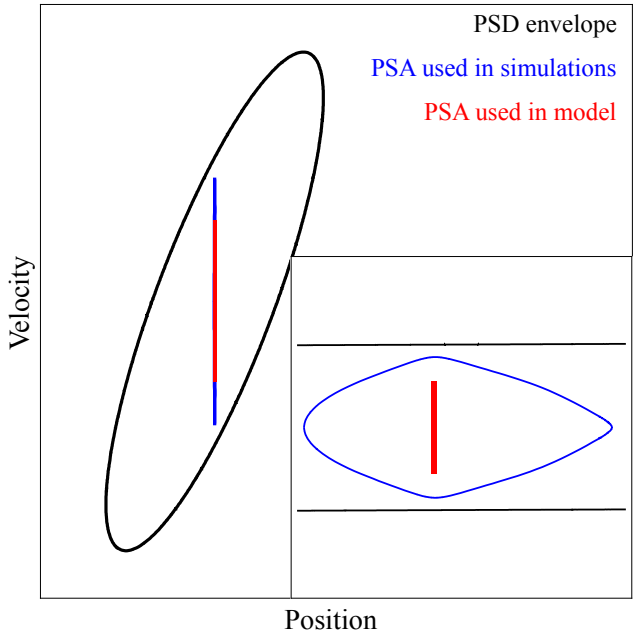

Finally, since molecules are accepted over a range of times we have to do a further integral over all later times to get the total number of molecules accepted:

$$N = \int_{t_0}^{t=\infty} \int_{V_a(t)-\Delta v/2}^{V_a(t)+\Delta v/2} G(H, V_z, t)\ \mathrm{d}V_z(t)\ \mathrm{d}t. \tag{3.12}$$

With an infinitely small separatrix width in position and a continuous integration over all times, we are essentially approximating the acceptance as a continuous sweep through the PSD. In fact this acceptance happens in bunches- as mentioned earlier if molecules are not accepted at the right point of the well movement, they will slosh from well to well and exit the apparatus undecelerated. Building in a phase-dependent acceptance may be one avenue for improving the model, although this approximation was not significant for the parameter space we explored.

We stop here and do not consider any loss mechanisms inside the decelerator itself. The validity of this assumption is supported by Fig.3.15, since over 95% of molecules are not lost within the decelerator itself. Therefore we expect that the results of Eq.3.12 should be proportional to the number of molecules decelerated in our simulations.

3.4 Comparison of the Model to Simulation Results

Using this formalism, we compute the number of molecules accepted into the decelerator for many linear acceptance functions. We can see from Eq.3.6 that each such function is defined once H and V_i are chosen. We would expect that the choice of a larger H would generally result in more molecules being accepted, since this would both decrease the instantaneous velocity spread of the PSD at the decelerator entrance and increase Δv because of the smaller accelerations needed. We might also expect that the best index molecule to use would be the molecule at the center of the initial phase space distribution, i.e. one with initial phase-space coordinates of $(z, V_z) = (0m, 180m/s)$. This choice is especially tempting, since this choice would suggest that we could in general ignore the "distriubution" part of the PSD and concentrate on just one molecule.

In Fig.3.19, we plot the results of theoretical model on top of simulations that count the number of decelerated molecules for many different index molecules. Each simulation was run several times so that we could get an idea of how the size of the distribution maps to the error in the number of molecules decelerated. We can immediately see that: 1) the agreement of the model with simulations is startlingly good, which confirms that the cylindrical symmetry of the TWD allows us to disregard the transverse dimensions of the decelerator. 2) This agreement also confirms our assumption that molecule losses within the decelerator itself are rare, since we are comparing molecules accepted (theoretical model) to molecules decelerated (3D simulations). 3) Both of our naive assumptions seem to be incorrect- increasing the hexapole length does not always translate to more molecules captured, and the best choice of index velocity is not always the average velocity of 180 m/s - in fact, for a 1.5m hexapole we get almost a factor of two improvement by using an index velocity of 210 m/s.

Figure 3.19: 3D simulation results plotted on top of theoretical model calculations, for three different hexapole lengths. The model calculations have been scaled to be the same height as the maximum of the simulation results. The good agreement suggests that 1D calculations are suitable for predicting how many molecules will be decelerated, obviating the need for computationally expensive 3D simulations.

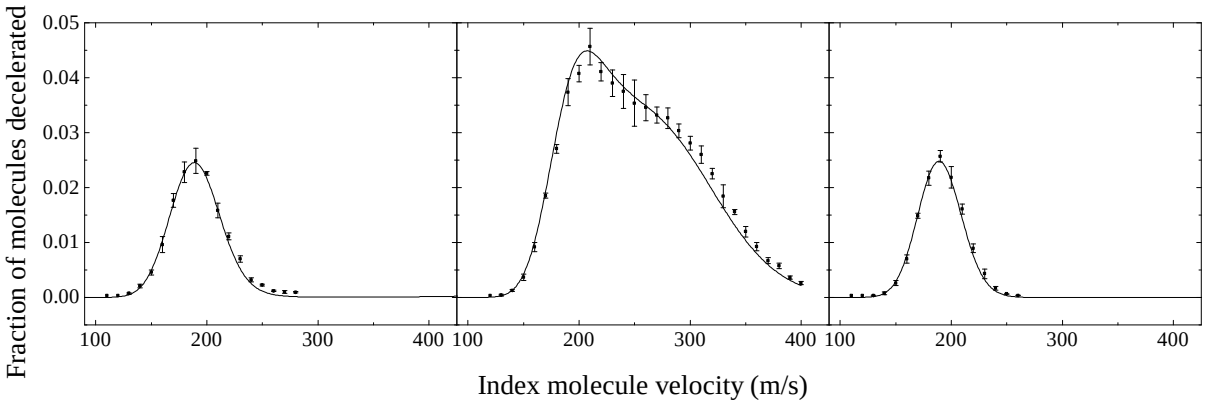

We can explain point 3 by considering the turn-on time of the decelerator. In the simulations, the decelerator turns on as soon as the index molecule arrives at the entrance (t_0). We again consider the overlap of the PSA of the decelerator and the actual phase-space volume occupied by the molecular distribution. Qualitatively, this overlap is influenced by three factors: 1)how closely Va(t) approximates H/t, 2)whether t_0 is early enough to capture a majority of molecules at the decelerator entrance, and 3)how large Δv is for the acceleration used. The first and third factors are similar for 180 and 210 m/s index molecules, but since the decelerator turns on when the index molecule arrives, using a 180 m/s index molecule means that 50% of the molecules have already passed the decelerator entrance. Using a 210 m/s index molecule decreases the number of molecules that escape the acceptance region before t_0.

Figure 3.20: This figure shows the portion of the initial PSD that has been accepted into the decelerator for linear and H/t acceptance schemes. The gray regions show the PSD of the molecular beam as it enters the decelerator after traveling through a 1.5 m hexapole guide. These gray regions are identical in each frame. The black regions show which molecules will be accepted after the acceptance process is complete. The top row shows the overlap for linear acceptance schemes, while the bottom row shows the overlap for H/t acceptance schemes.

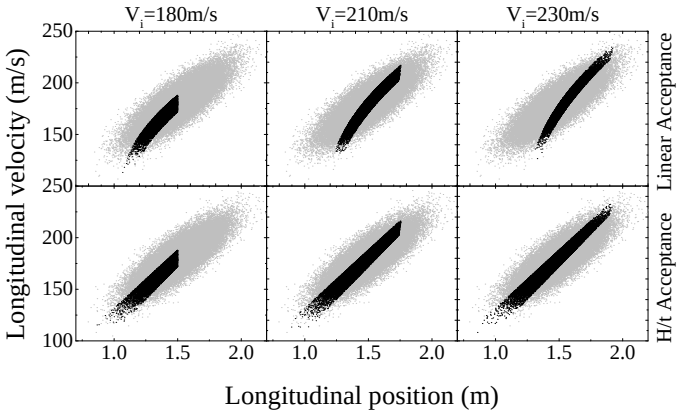

We show a visualization of the overlap between the PSD and the accepted molecules in Fig. 3.20. We see that for linear acceptance functions, using a 210 m/s molecule more effectively samples the high-density center of the incoming PSD, resulting in more molecules accepted. Typically, decelerators are operated such that they turn on when the synchronous molecule, which is analogous to our index molecule, reaches the entrance of the decelerator. Fig. 3.20 suggests that a better mode of operation could be to turn the decelerator on immediately after the molecular beam exits the source. However, most molecules that are faster than the index molecule will exit the decelerator before they reach the final velocity. The number of molecules rejected this way cancels out most of the benefit of turning the decelerator on earlier.

To illustrate the agreement between the 1D and 3D results in a different way, we compare separatrices used in the model and the simulations, as well as final phase space positions of the simulation molecules (Fig. 3.4) in an individual well.

Figure 3.21: A comparison of the 3D simulation results, 3D separatrices, and 1D model separatrices. One 3D separatrix is superimposed on one filled well from the beginning, middle, and end of the decelerated molecule PSD. The 1D model approximates the PSA as a continuous region in the position coordinate, so we show only the velocity boundaries (horizontal lines). The difference can only be discerned when the scale is increased to show individual wells. We see that the model separatrix does accept molecules between individual wells, which, although unphysical, results only in a consistent overestimate of how many molecules can be accepted. This accounts for the excellent agreement between the model and simulations in Fig. 3.19 after a constant scaling.

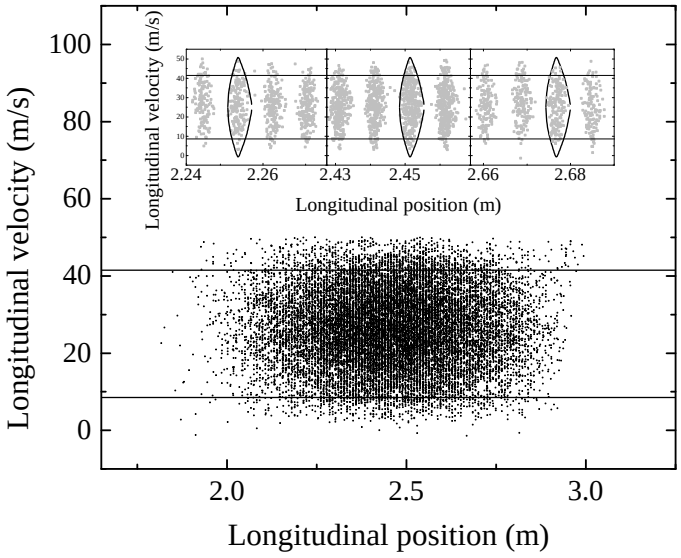

We also tested deceleration schemes using a deceleration function that matched the incoming velocity of the molecular beam (i.e., H/t). The results of that model are shown in Fig. 3.4.

Figure 3.22: 1D model predictions of the fraction of molecules decelerated using the $1/t$ chirp for hexapole guide lengths of 0.5 m, 1.5 m, and 4 m. The number of rings required to decelerate the molecular pulse using a particular hexapole guide length are shown for a index molecule with a velocity of 231 m/s (dashed line), which is 180 m/s plus three times the longitudinal velocity width.

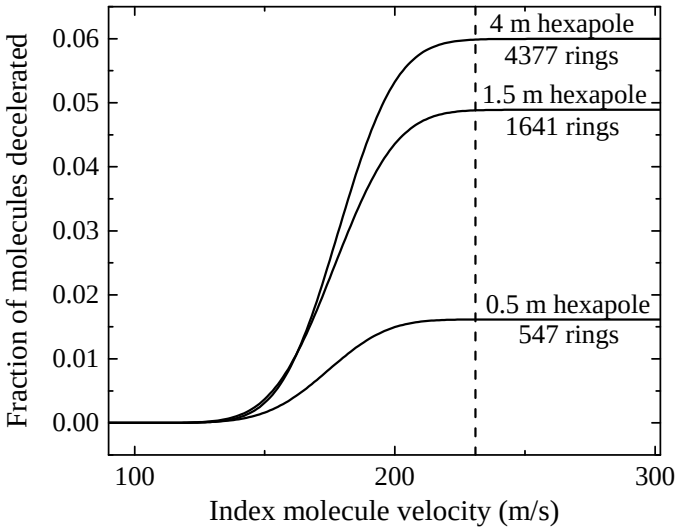

For the H/t chirp scheme, the index molecule sets only the time the decelerator turns on. Thus, if it turns on before most of the molecules reach the decelerator entrance, the number of molecules decelerated should be independent of the exact index molecule velocity (that is, the decelerator turn on time). This effect can be seen as a plateau in the number of molecules decelerated for large index molecule velocities (Fig. 3.4). Unlike the results for the linear simulations, the number of molecules accepted does reliably increase with hexapole length just as we would expect, since a choice of large index molecule velocity will ensure that the entire packet is accepted. As the molecular beam becomes more correlated in position and velocity with longer hexapole lengths, the PSA will better match the incoming molecular beam PSD. The increase saturates once the overlap of the PSD of the molecular beam and PSA of the decelerator is a maximum. This occurs at a fraction of 6%. (Note: 90% of the molecular beam is outside the transverse PSA regardless of the correlation length.)

There is one problem we still have not considered associated with using a $1/t$ chirp, which comes to light when we consider the longitudinal phase-space trajectory, $V(z)$, experienced by these molecules. If we know that $V(t) = \frac{H}{t}$, then we can integrate this to obtain

$$z(t) = Hln(t) + C \tag{3.13}$$

We require that at time t_0 the index molecule (with velocity V_0) has traveled the distance of the hexapole H, meaning $z(t_0) = z(\frac{H}{V_0}) = H$, which gives

$$C = H - Hln\left(\frac{H}{V_0}\right). \tag{3.14}$$

We plug this back into $z(t)$ and invert the function to get $t(z)$:

$$t(z) = \frac{H}{V_0} exp\left(\frac{z}{H} - 1\right), \tag{3.15}$$

which we can plug into $V(t) = H/t$ to get

$$V(z) = V_0 e^{1-\frac{z}{H}}. \tag{3.16}$$

Immediately evident from these trajectories is that molecules can only be slowed to a stop with an infinitely long decelerator. The dependence on hexapole length also means that the number of rings must be considered when implementing $1/t$ chirp schemes. In contrast, any length may be chosen for a linear chirp scheme with the caveat that shorter decelerators will require the use of larger accelerations. However, for the $1/t$ chirp, the number of rings is a fixed value depending on the hexapole length and the initial and final velocities. The number of rings required for a $1/t$ chirp is given by

$$N_{rings} = \frac{H \ln \frac{V_0}{V_f}}{\Delta d}, \tag{3.17}$$

where Δd is the ring spacing. Thus, to realize the large gain in decelerated molecule fraction, one must build an unreasonably long Stark decelerator of several meters(Fig. 3.4), whose versatility

would be severely hampered, since the initial and final velocities cannot be varied.

The naive solution to this would be to simply switch to a linear chirp once all the molecules were accepted into the decelerator, and then slow them to the desired velocity. If we attempt this solution several new questions arise: How much decelerator length should we allocate to linear chirp? The molecules are now spread out over many rings; what should we consider the position of the index molecule to be now? What acceleration (which depends on the remaining deceleration distance as in eq.3.5) should be used? If this new can of worms seems familiar, it is because it is the same as the one we have been dealing with the whole time- we are merely trading the problem of large velocity spread for one of large position spread, and would have to consider different chirps based on an index molecule *position* instead of an index molecule velocity.

The linear chirp ends up being a practical compromise, especially since, if the length of decelerator is fixed at 600 rings, the linear chirp produces three times more decelerated molecules than a 1/t chirp.

Until now, we have evaluated the deceleration schemes based on total number of molecules decelerated. For experiments that use a slow controlled molecular beam, the total number or integrated flux is the important metric, but for experiments requiring loading molecules into a trap, density also plays a role. A table of the decelerated fraction, molecular density, and number of rings used for the different protocols is shown Table 3.2. The densities were calculated from the simulations by counting the number of molecules in the central well of the decelerator and assuming the molecules were uniformly distributed in the well volume. We note this underestimates the true peak well density. We expect that slowing protocols that make use of longer hexapoles would result in decreased well densities because longitudinal phase-space distribution spreads during the flight time in the hexapole. This idea is borne out in the case of linear slowing protocols; the peak density decreased for longest hexapole length, although the decrease is not very significant over the range explored.

Hexapole Length	Linear Deceleration			$\frac{1}{t}$ Deceleration	
	Density (mol./cc)	Fraction	Rings	Fraction	Rings
0.5m	1.7×10^9	0.025	600	0.016	547
1.5m	1.5×10^9	0.045	600	0.049	1641
4.0m	8.2×10^8	0.025	600	0.060	4377

Table 3.2: The fraction of the initial beam that is decelerated to 25 m/s, central well densities, and number of decelerator rings used for various correlation (hexapole) lengths for both linear and $1/t$ acceptance functions. The number of rings used to decelerated using the $1/t$ chirp was set by the final velocity of 25 m/s. The density in the central well was calculated by assuming 10^{11} molecules per initial pulse, and a uniform distribution within each decelerator well (which therefore represents a slight underestimate of the peak density).

Chapter 4

Cell Characterization

4.1 Buffer Gas Apparatus

Our apparatus employs a sumitomo [1] SRDK series two-stage cryocooler, which has the capability to cool the first stage to 40 K and the second stage to 4 K. All cooled components are anchored to the second stage except or the black body radiation shield, which lowers the heat load from black body radiation from the laboratory incident on 2nd stage components. Temperature measurements are made with the use of Lake Shore [2] temperature sensitive diodes, and components may be heated with high power resistors placed on the cell and cryopump. We will discuss cryogenic requirements later in the chapter, but for now we focus on the design of our buffer gas cell. We began our experiments using a cell we designed with the help of Jonathan Weinstein. The geometry we used first was very simple from a machining standpoint, being simply the intersection of three cylinders through a copper cube (Fig.4.1,4.2).

[1] Sumitomo RDK-415 pulsed tube cryostat, Sumitomo Corporation, http://www.sumitomocorp.co.jp/english/

[2] Lake Shore Cryotronics uncalibrated cryogenic temperature sensor, PN DT-670-B1-CU, http://www.lakeshore.com

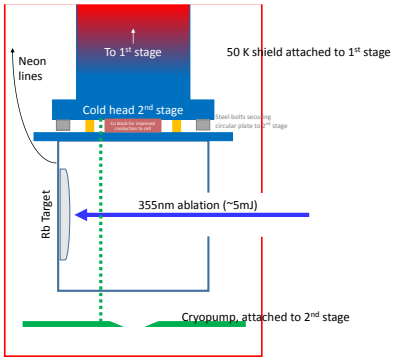

Figure 4.1: Our original cell set up for Rb absorption spectroscopy experiments.

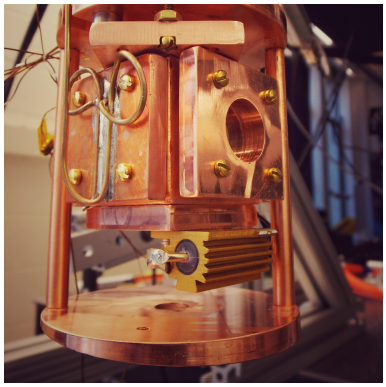

Figure 4.2: Picture of the absorption spectroscopy setup with old cell. When we eventually switched to a new cell design, the new cell -being almost the same size transversely- was simply swapped in. A cryopump is anchored to the second stage, for reasons discussed in sec.4.2

We eventually incorporated a new kind of cell design with a simpler internal geometry and extra features designed to improve signal stability. The new cell (Fig.4.3,4.4) is based on the design of the Doyle group, and incorporates parts made by them. This cell supposedly has several empirically important advantages in that it features a neon inlet and reservoir meant to direct the flow of neon downward in a smooth, vortex-free way, a spacer unit between the neon inlet and the ablation region, and a user friendly "mix-and-match" style assembly that allows us to easily tinker with the geometry. In general, we found that using the Doyle style cell produced less noisy signals and more predictable lifetimes and extraction efficiencies, which may be partly due to the fact that the simpler internal geometry made measurement of the cell parameters easier.

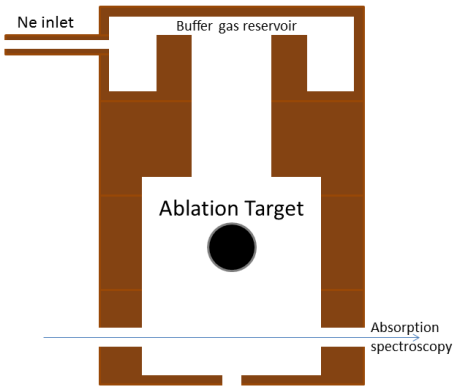

Figure 4.3: Schematic representation of our new buffer gas cell, based on the design of the Doyle group.

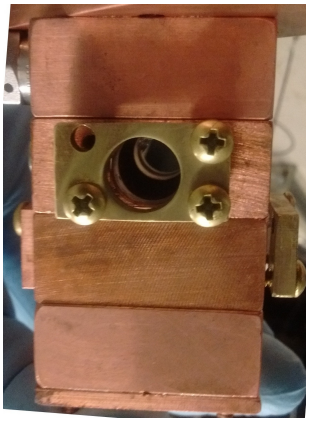

Figure 4.4: Realization of the Doyle-style buffer gas cell, looking on the absorption spectroscopy windows.

The cell stack starts with the neon inlet, below which is mounted the ablation target, with the ablation laser aligned into the page. Below the ablation target are two widows through which an absorption spectroscopy laser may be aligned. Finally, there is an aperture at the bottom of the cell. The dimensions of the cell and aperture must be designed to favor extraction of the buffer gas from the cell. To this end, we consider two timescales- the time for molecules to diffuse to the walls of the cell (T_{diff}), and the time for molecules to be "pumped out" through the aperture (T_{pump})[99].

$$T_{diff} = \frac{L^2 n \sigma_{X-Ne}}{4} \frac{2k_b T}{m_{Ne}}^{-1/2} \tag{4.1}$$

$$T_{pump} = \frac{L^3}{4A} \frac{k_b T}{m_{Ne}}^{-1/2} \tag{4.2}$$

Here, L is the characteristic length scale of the cell, A is the area of the aperture, n is neon number density, k_b is Boltzmann's constant, and T and m_{Ne} are the temperature and mass of the neon atoms. σ_{X-Ne} is the scattering cross section of the ablated species with neon.

[100] found that extraction efficiency generally increases with aperture size. Since the persistence time of molecules inside the cell is unimportant for our experiment, we use an aperture size

of 5.5mm, which gives pumpout times of < 1 ms. Our cells are not cubic, but for calculations we use the cube root of the volume as the characteristic length scale. The newer Doyle group cell has a length scale of $L = 27$ mm.

For good extraction we require $T_{pump} < T_{diff}$ [101]. If this condition is not met all the molecules will stick to the walls of the cell and will never be extracted from the cell. Since T_{pump} depends only on the collision rate between molecules and the aperture area, it has no dependence on the density of neon, which is assumed to be uniform in the cell. On the other hand, the T_{diff} depends on the mean free path of molecules in the cell, which is a result of collisions between molecules and neon atoms, and so depends linearly on neon density. At a constant flow rate ϕ through the cell density reaches an equilibrium, such that density and flow rate are related by:

$$\phi = nA\sqrt{k_b T/8m} \tag{4.3}$$

We will often use flow rate as a shorthand for density, since they are proportional to each other and since flow rate is the experimentally controlled variable.

Figure 4.5: A cartoon of the dependence of cell lifetime on flow rate, meant to show how, for some cell parameter choices, T_{pump} can compete with T_{diff} at low flow rates.

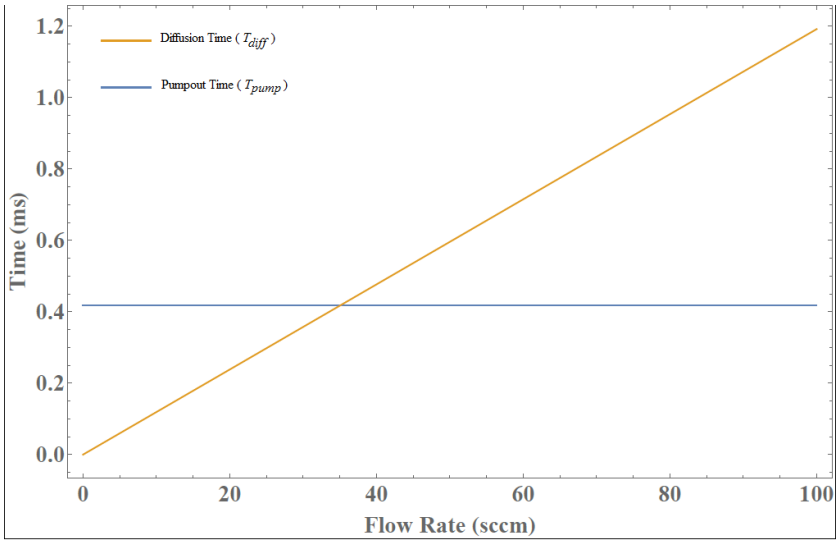

At first, the diffusion time grows linearly, as the time for the diffusion to the walls becomes longer. At some point the T_{diff} becomes larger than T_{pump} and the lifetime in the cell becomes independent of flow rate.

$T_{pump} < T_{diff}$ ensures that we will extract our molecules from the cell, but is not sufficient to ensure good cooling. We must also consider a thermalization time that ensures that the molecules reach the temperature of the buffer gas. We can get an idea of how long this might take in terms of the number collisions a species must undergo in order to thermalize. In each collision, the average kinetic energy lost by a molecule (assuming hard sphere collisions) is [47]:

$$\Delta T_m = -(T_m - T_b)/\mu \tag{4.4}$$

where T_b and T_m refer to buffer gas and molecule temperatures and μ is the reduced mass. After N collisions, the temperature of the molecule will be

$$T_m(N) - T_m(N-1) = -\frac{T_m(N-1) - T_b}{\kappa} \tag{4.5}$$

This is a discrete difference equation, but if we assume that the change in temperature per collision is much smaller than the molecule temperature (and therefore that the number of collisions N is large) then Eq.4.5 becomes

$$\frac{\mathrm{d}T_m}{\mathrm{d}N} = -\frac{T_m(N) - T_b}{\kappa} \tag{4.6}$$

where $\kappa = (m_m + m_b)^2/2m_b m_m$. The solution to this equation is

$$\frac{T_m(N)}{T_b} = 1 + \left(\frac{T_m(0)}{T_b} - 1\right) e^{-N/\kappa} \tag{4.7}$$

And since the molecules are originally much hotter than the buffer gas we have

$$\frac{T_m(N)}{T_b} = 1 + \frac{T_m(0)}{T_b} e^{-N/\kappa} \tag{4.8}$$

For CH in neon we have $\kappa \approx 2$, and for temperatures on the order of 1000 K we find that it takes about 20 collisions for the molecules to reach neon temperatures. Surprisingly, the number of collisions does not change much even for heavier species like C_6- here we benefit again from the use of neon, whose large mass compared to helium cools the entrained species much more effectively.

The mean free path of the molecules in the cell is given by [47]

$$\lambda = \frac{1}{n\sigma_{m-b}\sqrt{1 + m_m/m_b}} \tag{4.9}$$

where σ_{m-b} is the collision cross section between the molecule and the buffer gas atom. This cross section will be discussed later in the chapter, but for now can be estimated as on the order of 10^{-14} cm^2. We show plots of the number of collisions required to cool molecules from typical temperatures in Fig.4.6.

Figure 4.6: The number of collisions required to translationally cool CH (red) and C_6(green) from 5000 K (a typical ablation temperature) to 25 K (the coldest temperature we can reach with our cell).

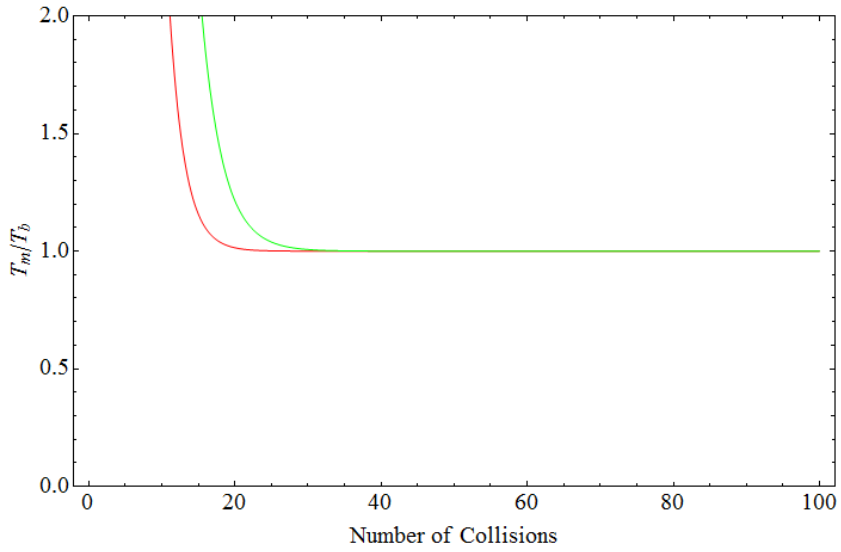

In Fig.4.6 we see that 40 collisions quickly cool the translational temperature of the molecules to the temperature of the neon buffer-gas. How many collisions actually occur in the cell? We can

estimate a lower limit on the collision rate r with

$$r = n\sigma V \tag{4.10}$$

where n is the neon density, σ is the collision cross section, and V is the relative collision velocity. Although this velocity starts out very large, owing to the hot temperature of the molecules, we can get a lower limit on the collision rate by using the most probable Boltzman velocity of the neon atoms. For typical cross sections and densities we obtain a collision rate of 8×10^6 collisions/s. For a T_{pump} of 1 ms, as we designed our cell to have, this gives almost 10^4 collisions, meaning that molecules are certainly thermalized by the time they leave the cell.

This formalism is a good predictor of translational cooling, but for vibrational/rotational cooling the vibrational/rotational relaxation cross sections should be used- these cross sections are generally smaller[47] than the collision cross section, which makes internal state quenching less efficient than translational cooling. However, since the number of collisions inside the cell is so large, and since vibrational and rotational relaxation cross sections are usually only 1-2 orders of magnitude smaller than the elastic collision cross sections, these degrees of freedom are also likely to be quenched in the cell.

4.2 Cryogenics

The temperature and pressure requirements of our buffer-gas cell are less demanding than those of conventional cells because of our choice to use neon instead of helium. However, the gas load is not insignificant. We already require the neon density to be high in order to maintain a small mean free path, however, in addition to this previous experimenters [99],[102] claim that the ablation technique requires even larger densities for good molecule cooling and extraction. The reasons for this are somewhat nebulous, although it is possible that since the ablation process is known to heat samples to several thousand K [103][104] the number of collisions required to thermalize the radicals becomes larger, decreasing the required mean free path even further. These

density restrictions require us to flow neon at flow rates on the order of 50-100 sccm. To handle this gas load, both for this and future experiments, it is sufficient to add a large piece of metal that is well anchored to the second stage of the cryocooler, which is as cold as possible to maximize sticking probability, which we will refer to as the "cryopump." We can make a rough estimate of the required cryopump size assuming that the probability of molecules sticking to be close to 1. This is actually a good approximation for neon, since we are so far below its freezing point. For a beam that is completely in the effusive regime, the angular spread of the beam can be as large as 120° [47]. If the cryopump is 2 cm away then we require a diameter of $2 \times 2\sqrt{3} = 6.9$ cm, or just under 3 in. Since our cell and beam parameters cause us to be much closer to the hydrodynamic regime our angular spread is likely smaller, although with this cryopump size we have the option to make our beam more effusive (for instance by increasing the size of the extraction aperture). This illustrates one of the main advantages of using neon over helium- since a helium beam would be operated much closer to its freezing temperature, the sticking probability is not close to 1, so a cryopump with a very convoluted surface area (like charcoal sorb) is required to ensure many collisions of the gas atoms with the cold surface.

Fig.4.7 shows the cryopump in action- neon ice has accumulated on it after several hours of cell operation. A heater located on the bottom of the cryopump allows us to sublimate the neon to prevent beam backscatter once the neon mountain gets too high.[3]

[3] Care must be taken when warming up any part of the apparatus after neon deposition- without cryopumping the pressure in the chamber spikes to a few torr and quickly destroys any ion gauges or auxiliary turbopumps that are still running.

Figure 4.7: A picture of the cryopump at work. Several hours of neon flow are required to build up this amount of neon.

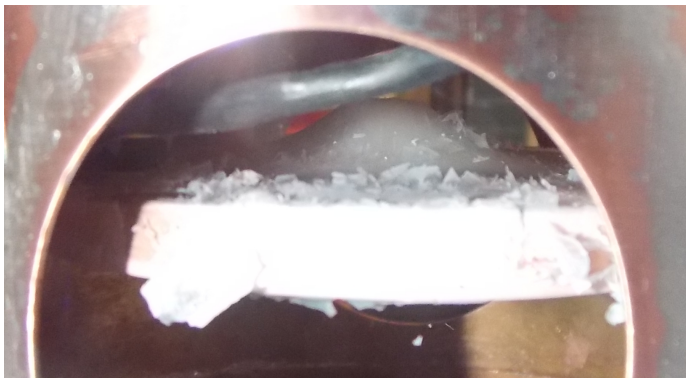

This is a much simpler way to handle the gas load than would be required by helium buffer gas beams- helium, being much harder to pump necessitates the use of extremely large surface area cryopumps, which can only be achieved with charcoal sorb that must be periodically reactivated.

4.3 Absorption Spectroscopy of Rb

We can test the properties of our cell by performing an absorption spectroscopy experiment. We installed a target of RbCl and ablated it with 532 nm light to produce Rb atoms. We then aimed a 780 nm diode laser through the cell and detected on the opposite side. A schematic of the experiment is shown in Fig.4.9

Figure 4.8: Schematic of the absorption spectroscopy setup.

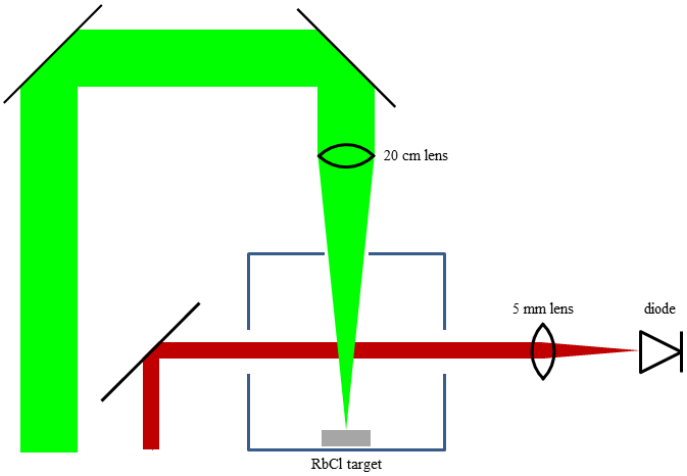

With each ablation laser pulse, the number of absorbers inside the cell spikes to a maximum, after which Rb atoms are pumped out through the aperture, causing the absorption signal to decay exponentially. A typical ablation pulse signal is shown in Fig.4.9:

Figure 4.9: A typical absorption spectroscopy signal for RbCl, monitoring the AC channel. In this case the flow rate is 40sccm.

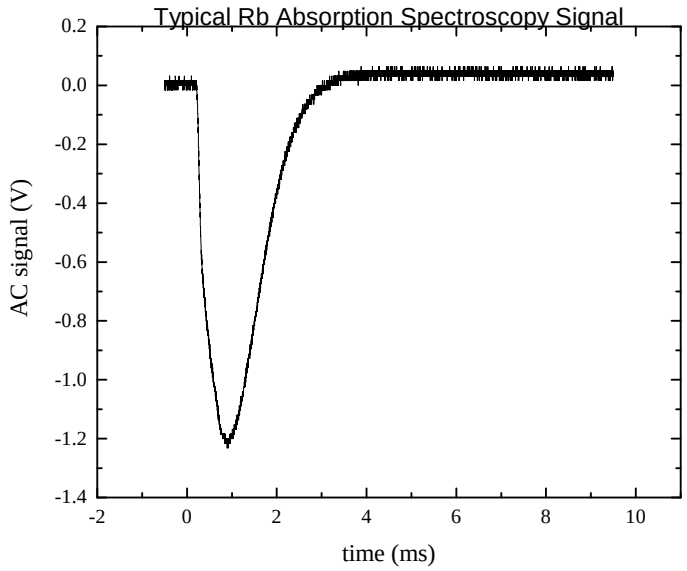

We fit this decay with an exponential to measure the signal lifetime. We can also perform the same experiment immediately outside the cell. If the molecules are being efficiently extracted

(meaning the cell lifetime is dominated by t_{pump}), the lifetimes inside and outside the cell should be similar. If we repeat these experiments at many different flow rates, we can get an idea of what mechanisms govern cell extraction. The results of these experiments are shown in Fig.4.10

Figure 4.10: Signal lifetimes as a function of flowrate

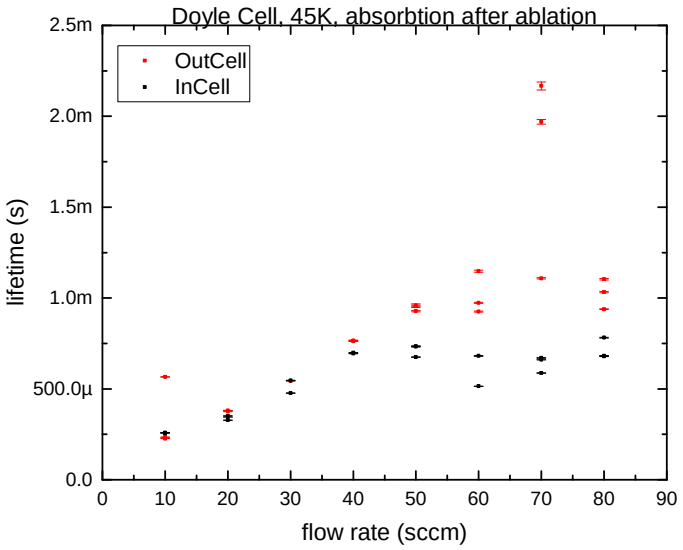

It is tempting to explain these data by assuming that the lifetime in the beginning grows linearly due to increasing diffusion times, and plateaus when the $T_{pump} < T_{diff}$. The only problem is that the diffusion time is proportional to the Rb-Neon scattering cross section. The guideline for designing buffer gas cells has been that the cross sections of most species with neon should be about 1×10^{-14} cm^2, and has been as small as 3×1^{-15} cm^2 [101], but in fact the scattering cross section is large enough that T_{diff} is usually too large to matter.

Measuring signal inside and outside the cell also allows us to see how the beam density changes upon leaving the cell by comparing the peak optical depth of Rb signals, extracted by combining the information from the AC channel (fig.4.9) with the DC offset and computing $OD = \ln(V_0/V)$. When we measure this for the cell, we get the dependence of OD on flow rate (fig. 4.11).

Figure 4.11: Optical depth of Rb as a function of flow rate.

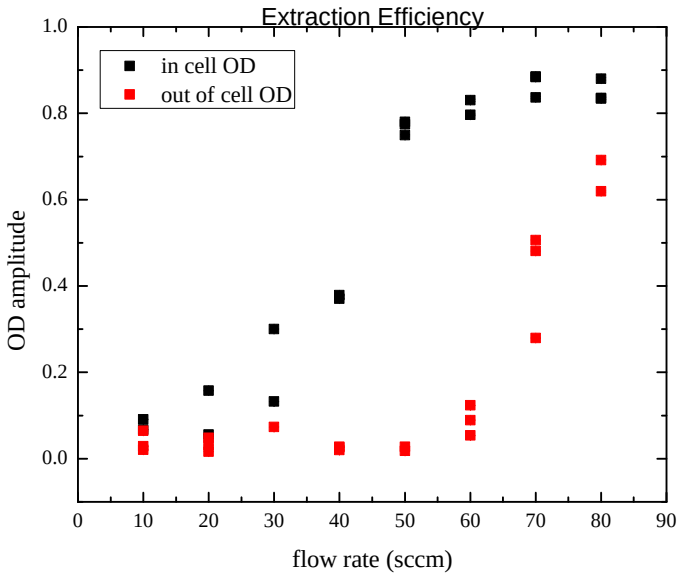

The extraction efficiency approaches 1 at higher flow rates, but in principle should be large whenever T_{diff} is larger than T_{pump}.

4.4 Scattering of Molecules by Neon

We can gain some insight into the order of magnitude of this collision cross section by considering the type of interaction involved when Rb scatters off of Ne. Qualitatively, because both species are neutral, the interaction between them is dominated by a strong repulsion at short distances due to the Pauli exclusion principle, and by an attractive Van der Waals interaction at large distances, which depends heavily on the polarizability of each atom. This interaction is empirically described by the Lennard-Jones potential [105], which has the form (for two neutral species):

$$V(R) = \epsilon \left[\left(\frac{R_0}{R} \right)^{12} - 2 \left(\frac{R_0}{R} \right)^{6} \right] \tag{4.11}$$

The Lennard-Jones parameters are known for Rb-Ne collisions, but the calculation is simplified when we consider that the collision energies, given by $K_b T$, are only in the range of $2-6$ meV (that is, 25-70 K). At these energies, the atoms do not penetrate to small R, so that only the long

range term need be considered, and the potential takes the form

$$V(R) = -\frac{C_w}{R^6} \tag{4.12}$$

where C_w is the Van der Waals constant. For a potential of this form [106] uses quasiclassical scattering theory to show that the cross section σ is given by

$$\sigma = A\left(\frac{C_w}{\hbar v}\right)^a \tag{4.13}$$

Where v is the collision velocity, and a and A are dimensionless constants that depend only on the power of the potential. For a $1/R^6$ potential $A = 8.08278$ and $a = \frac{2}{5}$. This result is valid as long as many collisional angular momenta contribute to the cross section so that the summation over partial waves required by the quantal calculation ([106]) and be converted into an integral. From a classical perspective, this is because the particle cannot penetrate into the center of the potential, because the impact parameter is too high, meaning the particle only sees the long-range interaction. This condition can be expressed as $l >> 1$, where l is [106]

$$\frac{\mu C_w k^4}{\hbar^2} >> 1 \tag{4.14}$$

In Eq.4.14, μ is the reduced mass of the colliding particles, and k is the wavenumber of the relative motion. Eq.4.14 is equivalent to

$$E^2 >> \frac{\hbar^6}{4\mu^3 C_w}, \tag{4.15}$$

and which in our case results in $E >> 10^{-6}$ eV. Another, more strict, condition requires that the particles remain far enough apart that the potential really does have Van der Waals form. This requirement can be expressed as

$$d >> \left(\frac{\mu C_w}{\hbar^2 k}\right)^{\frac{1}{5}} \tag{4.16}$$

The parameter d is of the same order as R_0 in Eq.4.11. For the Rb-Ne interaction this results in $E < 37meV$. The interaction energies for our experiment fall comfortably within these limits.

In Fig.4.12, we show the scattering cross sections for Rb with three different buffer gases- He, Ne, and Ar, with vertical lines showing typical operating temperatures for that gas. These cross sections are much larger- almost an order of magnitude for Rb- than those generally assumed.

Figure 4.12: Scattering cross sections of Rb with different noble gases, plotted on a log-log scale. The scattering cross section of Rb with Ne is about ten times larger than what is generally estimated to be for a wide range of molecules. At 590 K This calculation is 18% larger than the value measured by [107], who estimated their error at 10%. The measurement in [107] provides only a lower limit on the Rb-Ne scattering cross section.

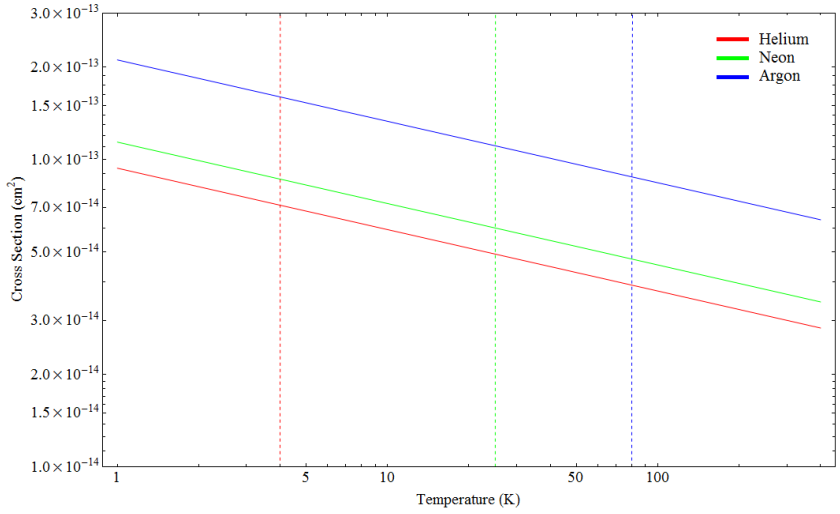

In this case the large scattering cross section is probably more due to the Rb than the Neon. Although neon is not very polarizable, being a noble gas, Rb is extremely polarizable because of its one valence electron[108], which causes the potential to be more attractive than the one we would expect for a Li-Ne interaction or, as a limiting case, a Ne-Ne interaction. [109] measured the Li-Ne cross section for thermal energies, from which they extracted a Van der Waals constant, and [110] did the same for Ne-Ne. We are concerned with this mainly so that we can extrapolate what the interaction might look like for molecule-neon scattering, since we will eventually be dealing with

large, rotationally hot, linear carbon chains in later chapters whose scattering cross section with neon we would at least naively expect to be big. As an example of molecule-neon scattering [111] measured Lennard-Jones parameters for acetylene-neon, for which we also plot cross sections in Fig.4.13 The C_w parameter for C_2H_2 (averaged over the approach angles, as would be reasonable for a rotationally hot molecule) is quite small, again due to the fact that C_2H_2 is not very polarizable. However, for a polar molecule it could be possible that the collision cross section becomes more significant. Lennard-Jones parameters have been measured for HBr, HCl, and H_2O, and the calculated cross sections are shown in Fig.4.13. We have also plotted the cross sections for large carbon clusters as a limiting (albeit nonpolar) example.

Figure 4.13: Calculation of scattering cross sections using Eq. 4.13, using Van der Waals constants from [112],[113], [114], and [115].

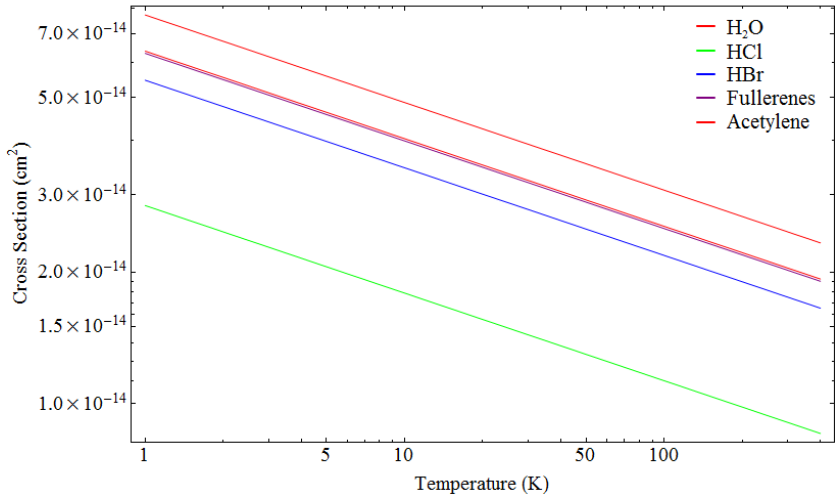

These cross sections are not significantly larger than that for Rb-Ne scattering. It could be that averaging over rotation misses some of what is going on, although this should be a good approximation if the timescale of the collision is fast compared to the molecule rotation, which is typical. Van der Waals constants can become really huge when dealing with polar molecules, as in [116], although once again [116] considers scattering with alkali metal atoms. Ultimately, the common assertion that the scattering cross section can usually be estimated as a few times

10^{-14} cm^2, regardless of molecule seems to be not unreasonable.

The upshot of these large cross sections is that, at least for the parameters of our cell, the diffusion time never gets small enough to compete with the pumpout time and thereby become an problem for beam extraction. In fact, when measured by [100] it has usually been on the order of tens of ms. Moreover, because the mean free path becomes so small at only moderate neon densities the distance that a molecule has to travel in the cell before it thermalizes (translationally) also becomes small- only a few mm [47], so that we can be somewhat confident that molecules have thermalized by the time they leave the cell.

Unfortunately, the relationship between T_{pump} and T_{diff} no longer describes our data. Below I show a figure similar to Fig.4.5, but in this case Eqs.4.1and 4.2 have been set to our cell parameters and with a suitable cross section for Rb-Ne at 45 K - 6×10^{-14} cm^2.

Figure 4.14: Theoretical dependence of signal lifetime on flow rate for our cell parameters and with a more realistic Rb-Ne scattering cross section.

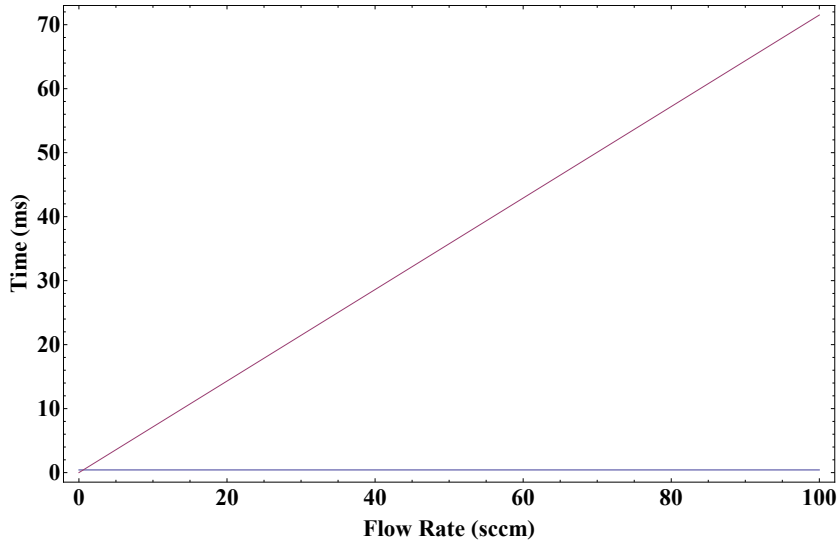

The sorts of trends in fig.4.10 for lifetime vs flow are not unprecedented. In [101] the author reports a signal vs flow rate plateau when looking at Ne beams seeded with ThO. What is more, in [99], very similar behavior is observed for T_{diff} vs T_{pump} when the author switches to a neon beam.

The reason for the failure of our data to agree with the T_{pump} vs T_{diff} model could possibly be that the assumption of uniform density inside the cell is not valid. The design of our cell (Fig.4.3) is such that the neon flow is aimed directly at the aperture, which makes this assumption unlikely to be true. It could be that we are building toward turbulent flow at higher flow rates which increases extraction time while it homogenizes the density of neon in the cell. Certainly the larger scattering cross section means that the Reynolds number, given by

$$R_e = \frac{2r_a}{\lambda_{b-b}}, \tag{4.17}$$

(where r_a is the aperture radius and λ_{b-b} is the mean free path) becomes large very quickly, such that flow is unlikely to be laminar, especially at the high densities we are aiming for in our cell. For our current cell parameters, R is on the order of 1000, which corresponds to a Knudsen number $K \approx 2R_e^{-1} = 0.002$. This puts us solidly in the hydrodynamic regime, suggesting that we at least have room to operate at lower flow rates, if achieving a laminar flow in the cell becomes important.

Chapter 5

Matrix isolation and FTIR spectroscopy

Coupling the output of a buffer-gas beam into a Stark decelerator presents many experimental and practical challenges, only some of which have been addressed by our simulations. We require a method of evaluating the quality of a buffer gas beam before investing significant effort in to building a hexapole guide, adapting our Stark decelerator to accommodate a cold head, and devising a state-specific detection scheme for our molecule of choice, to name just a few experimental hurdles. One way to address the detection issue is to use a "broadband" detection method, suitable for many different kinds of molecules. The workhorse detection method of the Lewandowski group has so far been ionization spectroscopy, but because this method hinges on addressing the electronic states of a molecule it requires UV laser wavelengths, which can vary by hundreds of nm for different molecules. For example, the relatively simple operation of switching from a molecular beam of OH to one of NH_3 requires changing the dye of our pulsed dye laser- a tedious process that can eat up a day of work in the lab and might result in covering the experimenter with carcinogenic laser dye. A more serious objection to this detection method is that if we are interested in characterizing a new molecule precursor, we would be blind to any unexpected ablation products because of the highly specific nature of ionization spectroscopy.

To address these issues, we turn to vibrational spectroscopy. Because molecular vibrational levels are much more closely spaced [105] than electronic levels, a blackbody infrared source is easily broad enough to interrogate the vibrational states of many different types of molecules. We have chosen to make use of FTIR spectroscopy, which gives us the additional advantage of being able to

measure absorption in all wavelength channels simultaneously.

It is true that using a high-enough energy ionization laser can ionize a broad range of molecules which can be sorted out later by time-of-flight mass spectroscopy, but wavelengths longer than those in the VUV range do not have enough energy to ionize most diatomic molecules that we are particularly interested in (NH, CH, OH)[85, 86]. What is more, for larger molecules this method would lack the ability to distinguish isomers, whereas IR spectroscopy would be sensitive to the shifts of vibrational modes caused by the presence of various isomers in the sample.

5.1 FTIR

Fourier transform infrared spectroscopy (FTIR) works by aligning a broadband source of infrared radiation into a Michaelson interferometer with a moving mirror (Fig.5.1). The infrared exits the interferometer and travels to an infrared sensor. The mirror moves and produces a phase shift, which modulates the intensity of each infrared frequency in a predictable way. Recording the signal as a function of mirror position produces data called an interferogram that is the Fourier transform of signal as a function of frequency. A sample may be introduced before the detector which further modulates the frequencies in the source- the two signals can now be compared to determine which frequencies are absorbed by the sample.

Figure 5.1: A schematic of our interferometer setup

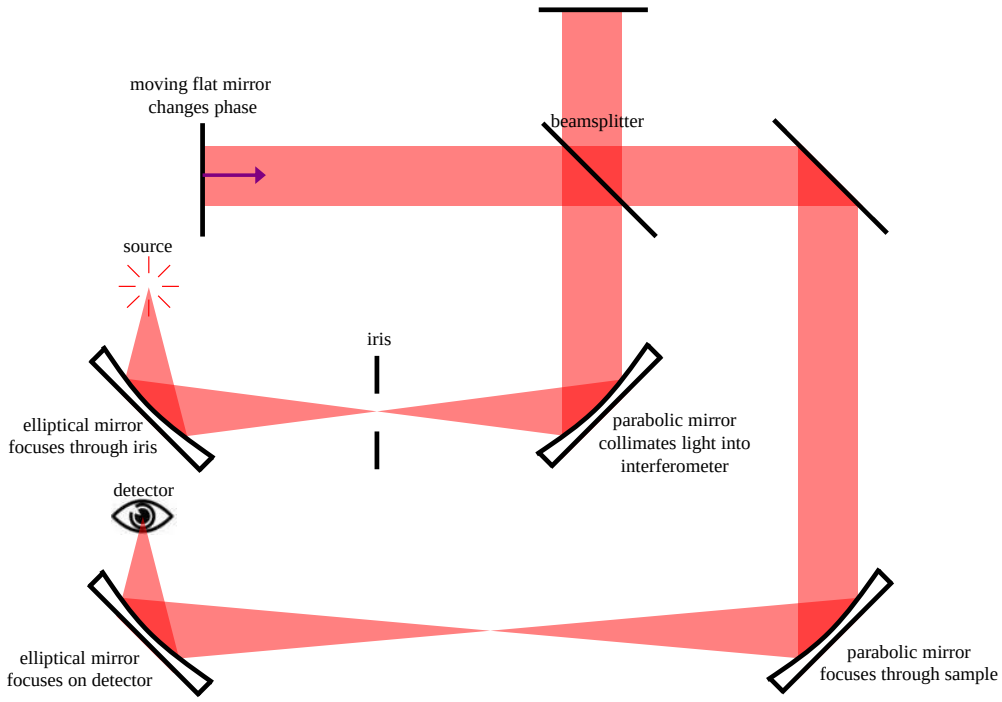

No laser is required to be tuned to the absorbtion frequencies of the sample, which in our case are unknown, as we are not certain of the molecules that will be produced by laser ablation. Scanning a tunable laser can also assure us that no absorption frequencies are missed, but has the disadvantage that most tunable infrared laser systems such as quantum cascade lasers have only limited wavelength range, and require much longer data collection times to scan through the entire region of interest[68].

5.2 Infrared Intensities

Physicists who do spectroscopy who are used to dealing with cross sections and linewidths may be unfamiliar with the IR spectroscopy concept of infrared intensity and the unit “km/mole”.

Infrared intensity A is defined as the integral over the frequency dependent cross section $\sigma(\nu)$:

$$A \equiv \int \sigma(\nu) d\nu \tag{5.1}$$

A should not be confused with the intensities I or I_0, which represent signal strengths with and without the presence of absorbers, respectively. It should also not be confused with Absorbance, which will be discussed later. According to Beer's law

$$\sigma(\nu))nl = \ln\left(\frac{I(\nu)}{I_0}\right) \tag{5.2}$$

substituting eq.5.2 into eq.5.1 gives

$$A = \frac{1}{nl}\int \ln\left(\frac{I(\nu)}{I_0}\right) d\nu \tag{5.3}$$

which has units of $\frac{1}{[mol/cm^3][cm]}[cm^{-1}]$, or $[cm]/[mol]$, which becomes $[km]/[mole]$ in SI units. It is worth becoming familiar with these units, as they are the default unit in which IR intensities are reported by databases such as NIST and HITRAN, and by computational software like Gaussian.

5.3 Matrix Isolation

Since we are using this experiment partially as a "buffer-gas source work" setup to test out new molecule precursors, we are cannot be sure of producing molecules in high density. To account for this, we choose to deposit the beam we make in the buffer-gas cell onto a matrix isolation window. To do this, we place an infrared-transparent window (typically CaF_2, but depending on which wavelengths we are interested in, these can also be KBr or even NaCl) below the aperture of our cell and cool it to well below the freezing temperature of our buffer gas. The buffer gas freezes onto the window, trapping the entrained molecules in the lattice sites (or between the lattice sites) of the resulting buffer-gas crystal. The concentration should be tuned such that it is highly unlikely that molecules will be trapped on adjacent lattice sites, which eliminates the strong molecular interaction broadening typical of absorption spectroscopy in solids.

To determine the limits on our allowed concentration, we consider first the requirement that molecules cannot be located on adjacent lattice sites of the neon crystal. Neon has a face centered cubic crystal structure [117], which means that any molecule deposited on a lattice site will have 12 nearest-neighbor lattice sites. Since we want to eliminate interactions between molecules, we would like to ensure that the nearest-neighbor lattice sites are NOT also occupied by molecules. If molecules/atoms are deposited randomly at lattice sites, the probability of all nearest-neighbor lattice sites being occupied by neon is

$$P_{noneighbors} = (1 - C)^{12} \tag{5.4}$$

where C is the fractional concentration of the molecule in neon. If we set this probability to be at least 99.99% then the concentration can be at most 8×10^{-5} to prevent interactions. We typically operate our cell with neon flows of 60 sccm, which works out to $2.7 \times 10^{19} atoms/s$. We have also measured our ablation pulses to produce 10^{11} CH molecules per shot, and we ablate at 10 shots/s, meaning we produce 10^{12} mol/s. Therefore our concentrations for *CH only* work out to $\approx 10^{-7}$. The caveats of this calculation include the fact that the concentration of molecules overall is higher, that we cannot be sure what the entrainment efficiency of the beam is, and that matrix FTIR experiments often use concentrations as large as 10^{-2}, and given all these we stress that this calculation is useful only as giving a rough order-of-magnitude estimate for when interactions might become significant.

In principle, the entrained molecules can be deposited indefinitely, increasing the amount of molecules to the point where we can detect them. However, in practice the molecular beam is impinging on the crystal at a large velocity (180 m/s), which results in fast crystallization and small crystal domains. These small domains can scatter away the infrared light and cause a sloping background (since shorter wavelengths are scattered more easily), Fig.5.2.

Figure 5.2: A spectrum showing wavelength-dependent scattering as a function of deposition time. The slope and offset seem to grow linearly with time, but this is likely because of small dynamic range.

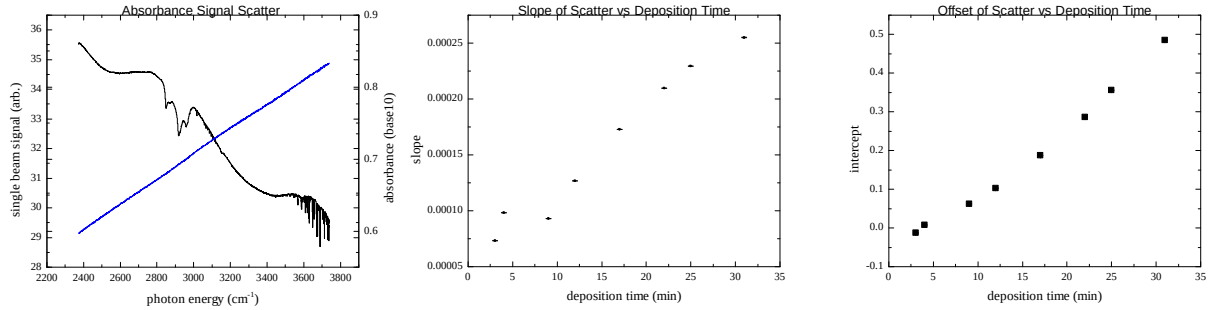

This scatter in principle sets a lower detection limit on the concentration of molecules in neon, but is difficult to quantify, as it depends strongly on the temperature of the window, the neon flow rate, and the velocity of the beam.

Although the lower limit on concentration due to scattering is difficult to analyze, we *can* set a lower detection limit on our CH production efficiency. For the calculations below, we will assume a typical linewidth for transitions to be 1 cm $^{-1}$, which is typical for matrix isolation experiments [25]. To begin, we can approximate the integral in Eq.5.3 as

$$\int \ln\left(\frac{I_0}{I}\right) d\nu = \int OD d\nu \approx OD\Delta\nu,$$

$$\Delta\nu = 1\ cm^{-1}$$

A complication is that our spectrometer measures base-10 optical density, i.e.

$$OD_{10} = Log\left(\frac{I_0}{I_\nu}\right) \tag{5.5}$$

We solve Eq.5.3 for n, and include conversion coefficients so we can use A in km/mole and OD_{10}. Units are included for clarity.

$$\boldsymbol{n}[cm^{-3}] = \frac{\boldsymbol{N_a}[mol/mole] \quad \mathbf{ln(10)} \quad \boldsymbol{OD_{10}} \quad \mathbf{1}[cm^{-1}]}{\mathbf{10^5}[cm/km] \quad \boldsymbol{l}[cm] \quad \boldsymbol{A}[km/mole]} \tag{5.6}$$

where n is number density in mol/cm^3, N_a is Avogadro's number, and l is the crystal thickness.

We assume that we consistently make the same number of CH molecules, which, as previously mentioned, is 10^{11} mol/pulse. In this case it is convenient, instead of finding the minimum molecule density, to find the minimum number of absorbing molecules. The most optimistic estimate assumes that all CH molecules are deposited inside the IR beam detection volume. Multiplying by a detection volume $V_{detect} = r_{min}^2 \pi l$, where r_{min} is the outer diameter of the infrared beam at its focus, we have

$$N_{absorb} = \frac{N_a \ln(10) OD_{10} 1}{10^5 A} \pi r_{min}^2 \tag{5.7}$$

The noise of our spectrometer ΔOD_{10} is about 2×10^{-4}, the infrared intensity of the CH ground state vibrational transition of is variously estimated to be ≈ 150 km/mole, and the IR beam size at the focus is 4 mm ø. Therefore, to achieve a signal-to-noise ratio of 1 we need 2.32×10^{12} CH molecules. Assuming we create 10^{12} mol/s, the number of absorbers is reached after just a few seconds.

The most pessimistic estimate would assume that the CH molecules were deposited over the entire CaF_2 surface, which has a radius of 2.54 cm. In this case the required number of CH molecules becomes 3.74×10^{14} absorbers, which we would deposit after 6 min. The required deposition time likely lies within these two limits.

5.4 Contaminants and Background Handling

The path of the infrared beam must inevitably pass through some amount of air outside of the vacuum chamber, which produces a background infrared signal. A characteristic spectrum is shown in Fig.5.3.

Figure 5.3: A typical background signal from our spectrometer. The IR beam is being aimed through the vacuum chamber and the deposition window.

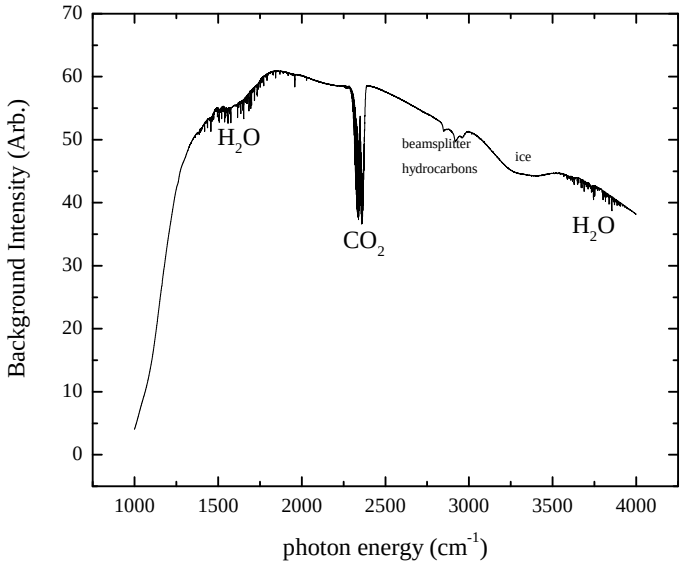

The strongest lines we see are caused by the vibration-rotation spectrum of CO_2. The lines are centered about the energy of the antisymmetric stretching mode, and produce two bands governed by the selection rule for transitions between rotational energy levels for linear molecules:

$$\Delta J = \pm 1, \tag{5.8}$$

which holds if there is no change in vibrational state [105]. This rule gives rise to two rotational bands- the P branch ($\Delta J = -1$), and the R branch ($\Delta J = +1$), and the spacing of rotational states in each band is given approximately by [68]:

$$E_J - E_{J-1} = BJ(J+1) - BJ(J-1) = 2BJ \tag{5.9}$$

Centrifugal distortion caused by coupling of vibration and rotation means that the spacing of both bands is not exactly the same. Because CO_2 remains linear in its antisymmetric stretch mode (i.e. it does not bend) the Q branch ($\Delta J = 0$) is forbidden. The CO_2 lines we see are shown in fig.5.4

Figure 5.4: A typical background signal from our spectrometer. The IR beam is being aimed through the vacuum chamber and the deposition window.

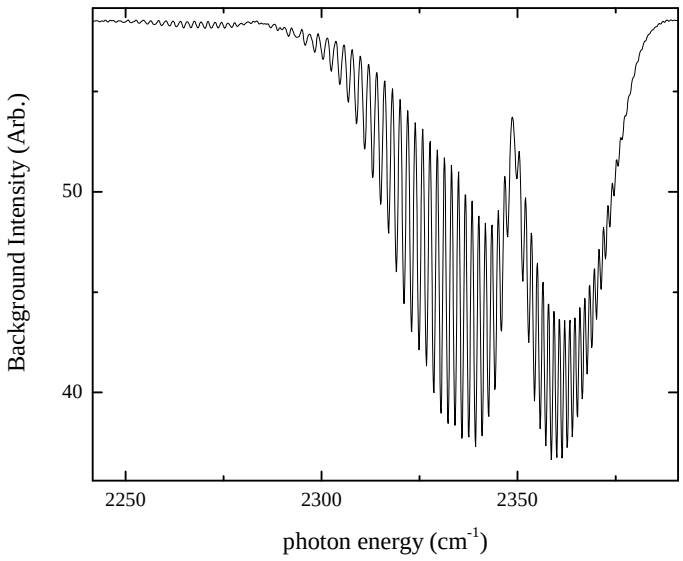

The two other sets of vibration-rotation bands that we see are H-O-H bending modes and O-H stretching modes of water. Because water is nonlinear, its vibration-rotation bands are not nearly as symmetric as those of CO_2, but we can still be confident that this is gaseous H_2O because of the line spacing.

In typical FTIR experiments, purging the inside of the spectrometer and the out-of-vacuum beampath is standard practice. We do purge the inside of our spectrometer with dry nitrogen, but because the vacuum chamber fits very snugly inside the spectrometer sample compartment we cannot purge the rest of the beam path very well. We are not overly concerned with these lines since they do not overlap with the molecule transitions we will be looking for. In fact the presence of these rotational bands is useful in separating out contributions from gas-phase molecules outside of the vacuum chamber and in-chamber contaminants, such as ice. The broad ice feature is due to once again to the water O-H stretch mode, but shifted from the effect of hydrogen bonding and broadened from collisions/interactions. If ice builds up significantly on the crystal, the experiment must be warmed to room temperature so that the water can be vaporized and pumped out. Ice buildup tends to happen because the vacuum chamber is continuously roughed, to prevent overpressures

during crystal cleaning. However, as the cryopumping of the cryocooler is extremely powerful-enough to reach base pressures of 5×10^{-8} Torr- the comparatively weak roughing line tends to act more like a leak for contaminants like water vapor. For our experiment, ice buildup becomes significant on timescales of about 1 month.

For molecules trapped in the matrix, rotational lines are generally frozen out. We occasionally detect the presence of contaminants like solid CO, CO_2, and H_2O, which we can assign to condensed phase contamination because of the presence of only vibrational modes (Fig.5.5).

Figure 5.5: Signatures of contaminants on the crystal surface. Such contamination can be avoided by evacuating the experiment chamber before cooling with a turbo pump, and not relying solely on the cryopumping ability of the cold head.

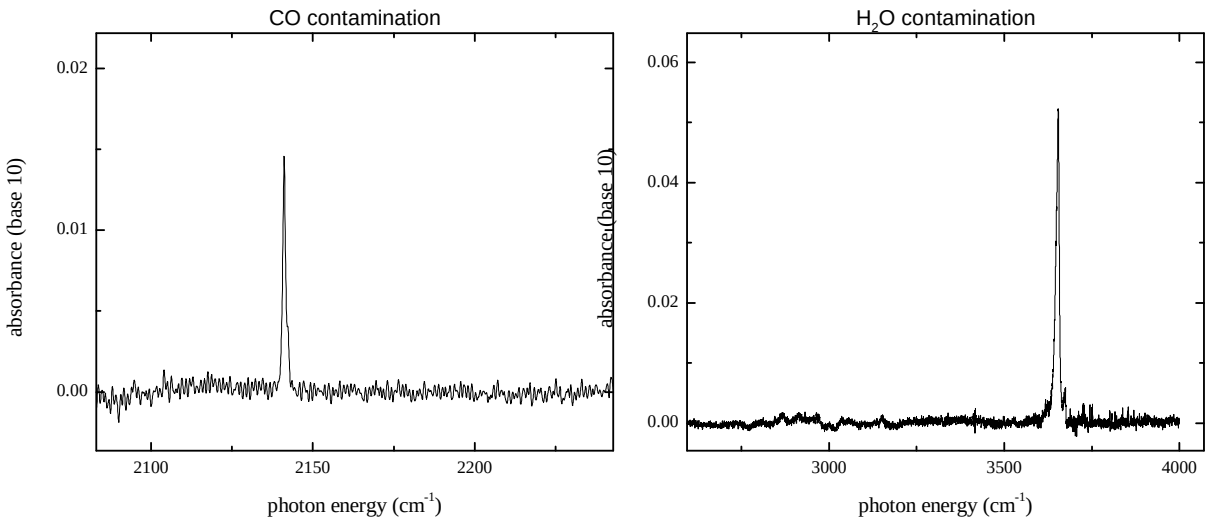

Another extremely irritating aspect of the background spectrum are the broad lines located around 2900 cm^{-1} (Fig.5.6). These seem to be a feature of the spectrometer and are, according to the good people at Thermo-Fisher, "some kind of glue" on the beamsplitter. This part of the spectrum is the C-H stretch region, and most hydrocarbons would show up here. The broadness of the lines does indicate some kind of condensed-phase material, and they are present even when the entire beam path is fully purged and no sample obstructs it.

Figure 5.6: Lines due to glue in the beamsplitter

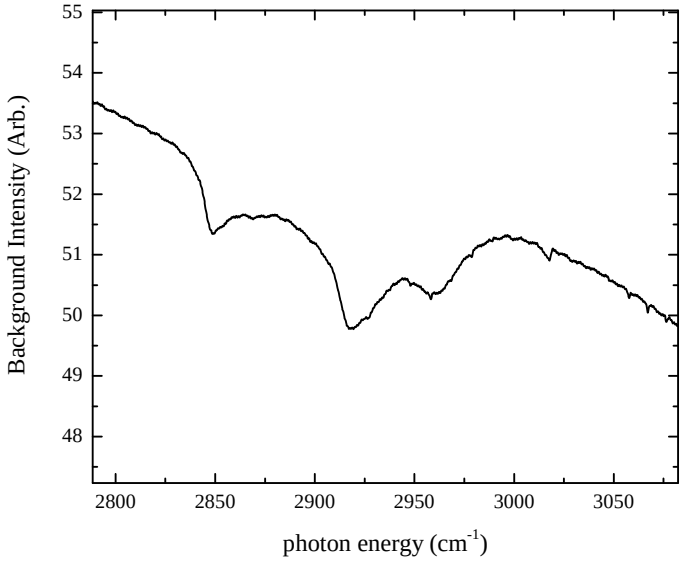

The last background feature that is important to take into account is the overall intensity envelope, which is a function of the spectral range of the IR lamp, as well as the size of the aperture in Fig.5.1 (diffraction around the aperture means that small aperture settings begin to cut out the far infrared).

We do not have a way of moving the deposition window out of the beam of the spectrometer, which means that we can take only one background every time we grow a crystal. We can move the spectrometer away from the vacuum chamber, but this is not ideal since we are not properly imaging the lamp intensity and the way it interacts with the three CaF_2 windows. Deposition with only one background trace works well for us because we have not had to look for lines in the CO_2 and water regions.

The background signal itself is measured in arbitrary units and is proportional to the voltage output of the IR detector. The spectrometer software calculates absorbance *Abs* and transmittance T according to

$$T = \left(\frac{S}{B}\right) \times 100$$
$$Abs = \ln\left(\frac{B}{S}\right),$$

where S and B are raw and background signals respectively, in arbitrary units.

In addition to this automatic background subtraction performed by the spectrometer, we also subtract away baselines due to scattering and shoulders of broad features. For all spectra shown in later parts of this thesis we perform this subtraction in order to be able to report just the peak height of relevant transitions, to isolate the contributions of just the molecules we are interested in.

5.5 Matrix FTIR of NH_3 Clusters

As both buffer gas beams and matrix FTIR are new technologies for our lab, we first tested our matrix isolation setup with a supersonic beam of ammonia (NH_3). A schematic of the setup is shown in Fig.5.7.

Figure 5.7: A schematic of a test setup to image ammonia clusters in a matrix. The source is a supersonic beam of ammonia seeded in argon at a concentration of 0.5%, which impinges onto a CaF_2 window cooled to 14 K. The beam makes use of a skimmer, which is not shown.

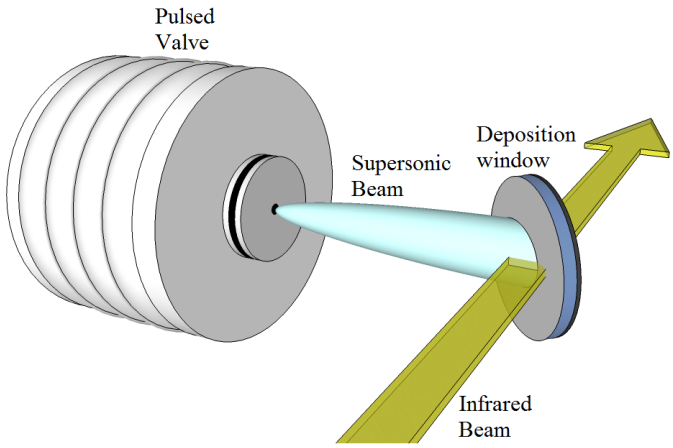

The experimental demands of this intermediate measurement are rather lighter than for a

buffer gas setup. Firstly, we can use argon as the cooling gas instead of neon, which a much higher melting point (84 K compared to 25 K). Secondly, we only have to cool the window and do not have to maintain a temperature difference between two cryogenically cooled objects, as we would for a buffer gas setup (discussed later in this chapter). Finally, the source allows us to prepare an exact mixture of gases whose concentration is controlled, while the choice of ammonia obviates the necessity of synthesizing the molecule from a precursor and will give us the opportunity of observing molecule clusters with strong vibrational transition strengths.

One other experimental perk of this setup is the fact that we do not have to use a black body shield to adequately cool the deposition window. This increases our optical access to the sample, and allows us to take pictures of the crystal (Fig.5.8).

Figure 5.8: A picture of a crystal of ammonia clusters in an argon matrix.

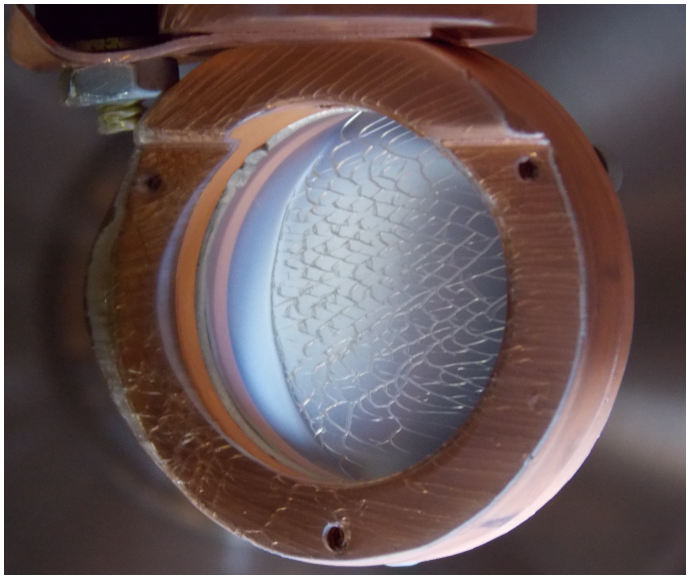

The vibrational spectrum of NH_3 in an argon matrix has been measured [118]. We show one of our own spectra with line assignments in Fig.5.9.

Figure 5.9: IR spectrum of NH_3 clusters in argon. Line assignments are from [118]. These spectra were gathered after depositing NH_3 for 60 min and firing the valve at 10Hz. Observed lines are tabulated in Tab. 5.1.

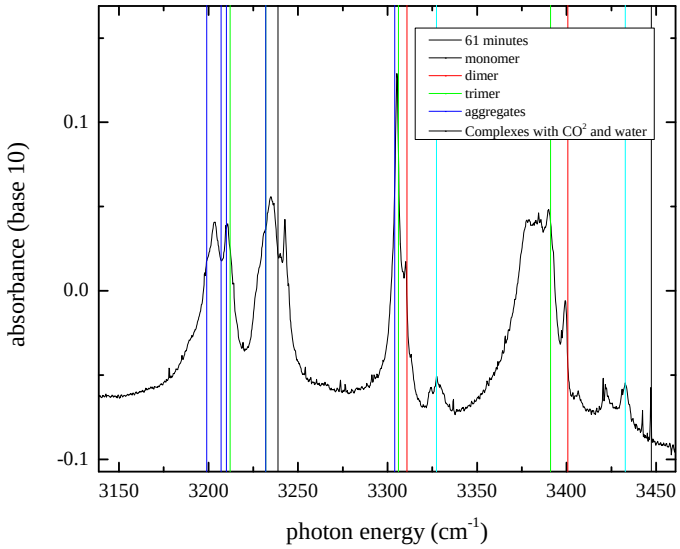

Line Position (cm^{-1})	NH_3 Cluster	Vibrational mode
3239	monomer	$2\nu_4$
3447	monomer	ν_3
3310	dimer	ν_1
3400	dimer	ν_3
3212	trimer	ν_1
3306	trimer	ν_1
3391	trimer	ν_3
3199	aggregate	
3207	aggregate	
3232	aggregate	
3304	aggregate	
3391	aggregate	

Table 5.1: A summary of the vibrational modes of ammonia clusters observed after deposition with a supersonic jet of ammonia seeded in argon into an argon matrix. Line assignments and modes are from [119].

The cluster lines exhibit significant broadening- at a concentration of 0.05% we are nowhere near below the concentration limit given by Eq.5.4, and because of ammonia's lone electron pair interactions can happen over a longer range. This also causes ammonia to cluster more easily, and clusters have larger IR intensities because of the ease with which they deform, which causes large changes in the magnitudes of their dipole moments. All this makes monomer lines difficult to isolate. We do, however, manage to pinpoint one monomer mode far away from the cluster modes for which IR intensities are known- the NH_3 monomer mode at 3447 cm^{-1}. This mode exibits a 0.087% shift away from the gas phase value, which is well within the expected bounds for Ar. The height of this peak is $0.036OD_{10}$, and its IR intensity is given as 7.1 km/mole, meaning that we have deposited 8.8×10^{15} NH_3 monomers within the detection volume. The OD of this peak

was shown to decrease for longer deposition times while other peak heights increased, suggesting that the monomers were forming clusters within the matrix, which is not surprising, given the concentration.

Figure 5.10: Traces showing IR spectrum of NH_3 clusters in argon at two different times. At some concentration monomers begin to react with each other to form clusters.

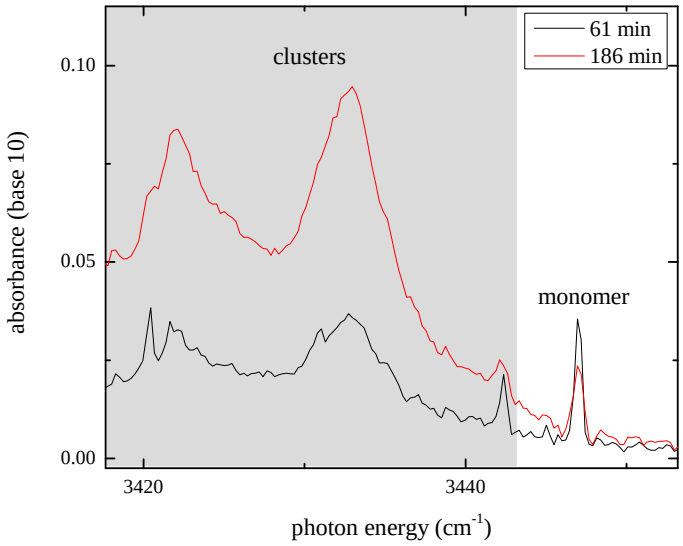

5.6 Isolation of Buffer Gas Beams

Figure 5.11: Apparatus schematic for isolating a buffer gas beam. The molecules are introduced into the cell via 532 nm ablation and are extracted by neon flow through an aperture, after which they are deposited onto an isolation window.

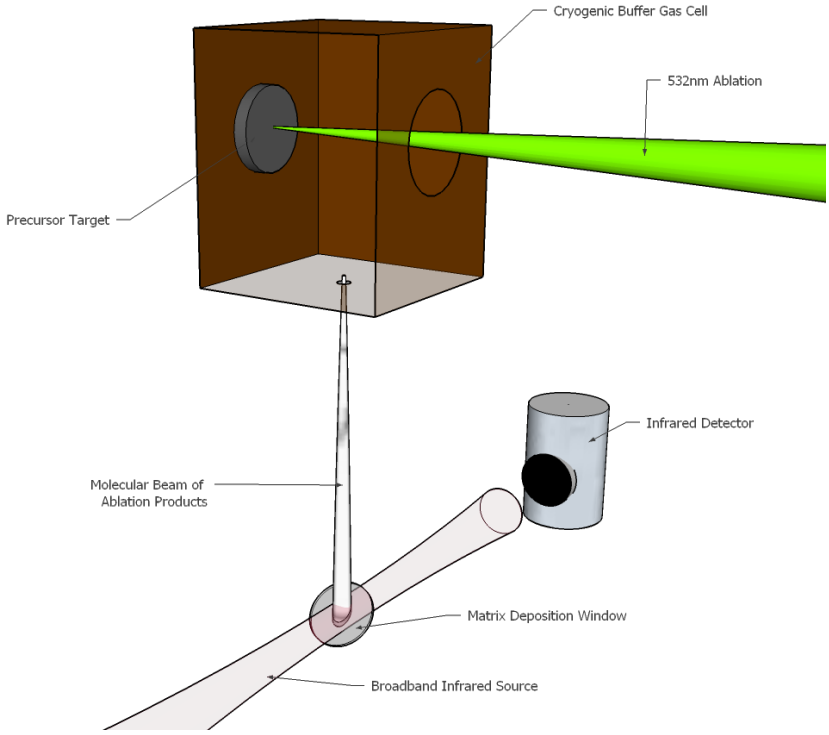

Figure 5.12: A picture of the apparatus modified to deposit buffer gas beams onto a matrix isolation window. In the figure one can see the strong coupling of the window to the second stage and the weaker coupling of the second stage to the cell.

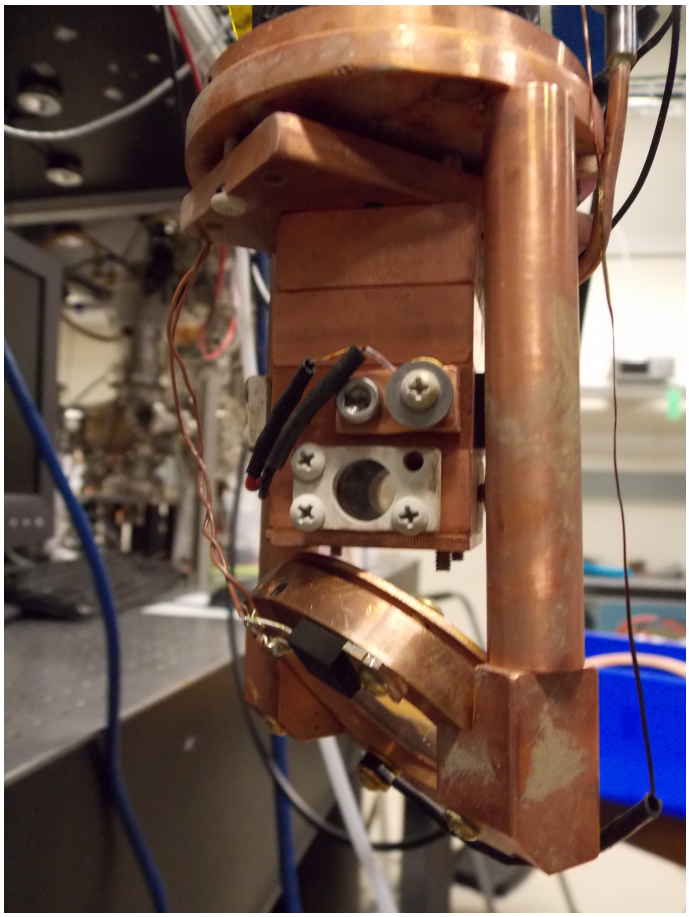

We show the realization and schematic of a setup that combines the elements required to create a buffer-gas beam and isolate it in a matrix. The setup shown in Fig.5.11 is similar to that of Fig.4.1, except that we have modified the cryopump to be used as a deposition window for a noble gas matrix seeded with the contents of our molecular beam. For the purposes of IR transparency, it is made, like the sides of our vacuum chamber, out of CaF_2. Most groups who do matrix FTIR experiments use other materials like CsI or KBr. These materials are too soft and hygroscopic for us to use, since our windows require frequent cleaning and the only way to clean a

hygroscopic window is by polishing [1] it. What is more, CaF_2 has desirable thermal conductivity properties. However, its cutoff in light transmittance near 6 μm means that we are insensitive to the "fingerprint region that characterizes the low frequency vibrations of complex molecules.

5.6.1 Cryogenics

The deposition window should be as cold as absolutely possible, which requires the use of a blackbody shield. The cryocooler is capable of dissipating 15 W of power when the second stage is held at 10 K, and the power delivered from blackbody radiation at room temperature is 420 W/m^2. This limit theoretically allows us to leave a huge amount of area open to lab radiation, but in practice poor conductance to all the components mounted on the second stage means that the difference between full radiation shielding and none can be as large as 10 K. Inside the blackbody shield, we see the second stage, which houses the cell and window. One complication of this experiment is that only one cold head is available for cooling both the cell and the window, which must be at very different temperatures. The cell must be hot enough so that there is no danger of freezing the neon onto the cell walls, whereas the window must be as cold as possible. It is tempting to think that the temperature of the window need only be below the freezing point of neon, at 25 K, but in fact the neon vapor pressure is still significant at temperatures below 25 K, enough that crystals will not immediately begin to grow at 25 K. What is more, at intermediate temperatures, the crystal is not "rigid," meaning that the bonds between atoms are not strong enough to isolate trapped molecules, which migrate through the crystal [69]. Therefore, we must actually cool the window to at least 1 K below the annealing temperature, which is reported as 10-12 K for neon[67]. We could relax this condition by working with argon, which has an annealing temperature of just 40K, but argon does not adequately cool the molecular beam. We could also relax this condition by cooling the cell *below* the melting point of neon as it still has appreciable

[1] Subsequent students take note- do not try to polish CaF_2! Even though it is much more robust and less hygroscopic than other salts, the polishing setup- usually an abrasive sandwiched between two lapping plates- uses water as a lubricant. The abrasive creates a large surface area for the water to attack, and the result will be a cloudy optic. In a pinch, hand polishing can work using high-grit sandpaper and acetone as the lubricant, but it is better to just live with the scratches.

vapor pressure there (Fig.5.13), but this makes it difficult to estimate the density of neon, and it would be preferable to work above this point. Furthermore, as we will see, controlling the cell temperature in our apparatus is a complicated proposition. The cell and window temperature are monitored by diodes from Lake Shore Cryotronics and high power resistors are mounted on both components to allow us heat them and adjust their temperature quasi-independently.

Figure 5.13: The vapor pressure of neon. Data from [120]. We could conceivably operate our buffer gas cell in temperature regimes below the melting point, but in that case the equilibrium pressure is influenced by the competition between neon in and out flow, and the sticking probability of neon with the walls. In these regimes the pressure should be measured directly to determine the neon density in the cell

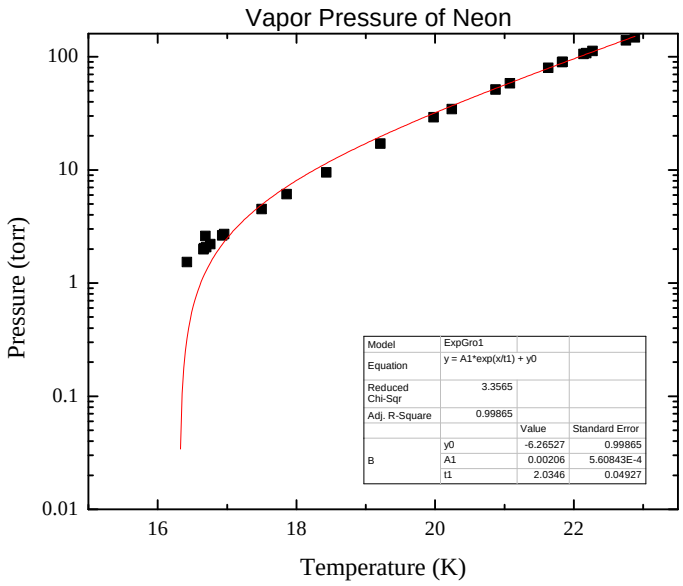

We attempted to tune the temperature of the cell by inserting a copper block in between the cell and the second stage. The laws of heat conduction suggest that the temperature difference between the second stage and the cell should go like the area of the copper block[121], that is

$$\Delta T = \frac{QL}{-kA}, \tag{5.10}$$

where Q is the heat dissipated, k is the conductivity, and L and A are the length and cross

sectional area of the copper block. However, as we show in Fig.5.14, changing the size of the block did almost nothing to change the final ΔT of the cell and second stage.

Figure 5.14: The intercept of the cell temperature vs second stage temperature as a function of copper block area. The slope of this dependence should remain constant while the intercept should go like the square of the copper block area. This is not borne out, likely because the force which compresses the block is not constant.

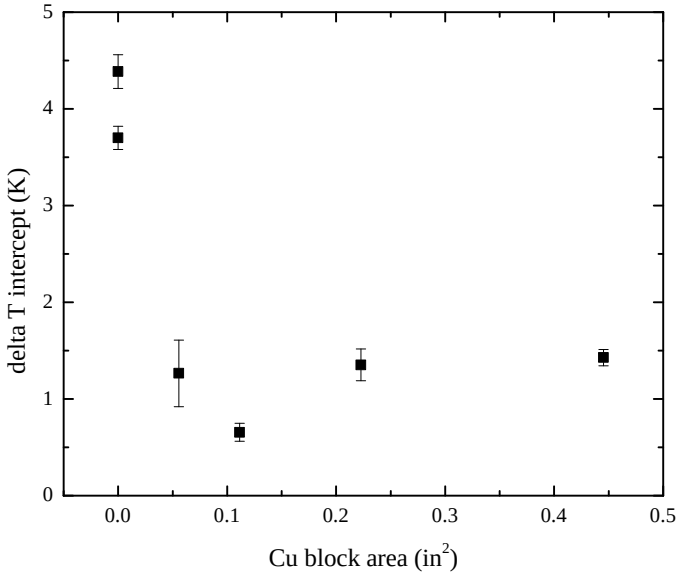

This is likely due to the difficulty of controlling the force with which the cell compresses the copper block. In future incarnations of this experiment, it may be worth it to redesign the cell housing in such a way that this force can be measured and fine-tuned. Lacking this, we ultimately had to resort to trial and error to cool the cell to a temperature that was cold enough to properly cool the entrained molecules and above the melting point. We ultimately ended up with a configuration that could sustain the temperature differences shown in Fig.5.15

Figure 5.15: Temperature difference sustained by the Cell and cryopump/Deposition window. This curve is not a constant of the apparatus and fluctuates somewhat depending on how well all components are tightened after modification and reassembly.

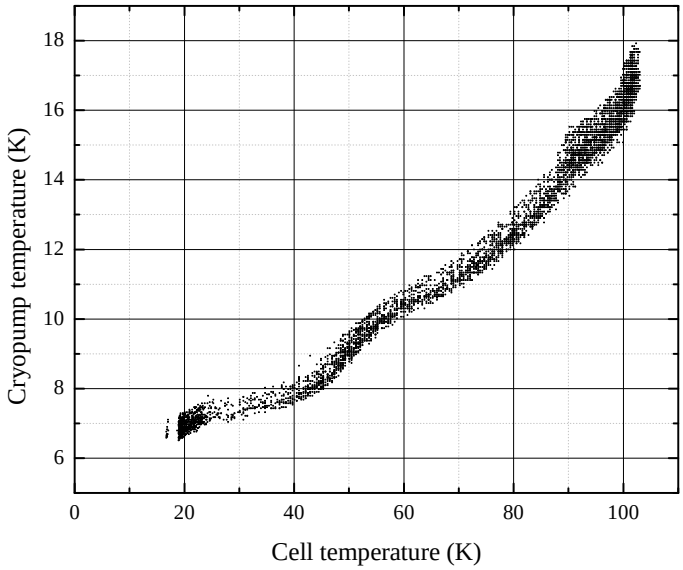

We also ran into cryogenics problems with the deposition window. As we mentioned, the temperature of the window must reach ≈ 10 K for crystal growth. Our deposition window is larger than usually used for matrix isolation (2") and the temperature sensor is mounted on the copper housing near its edge. According to this sensor, the copper housing was well within the correct temperature range (see Fig.5.15). However, during this time, we consistently failed to grow a crystal. After mounting a temperature sensor onto the window center it turned out the center of the window was not equilibrated with the edge, which pointed to poor contact with the window housing. At this point, the window was mounted in the copper housing according to Fig. 5.16, using two indium gaskets.

Figure 5.16: Cross section of old housing of the deposition window. A copper holder supports the window which is secured with a copper face plate and brass screws. Two indium gaskets actually made the contact between the copper housing and window poorer and failed to equilibrate the window center and edge.

These gaskets had to be compressed with extreme care, as any kind of uneven force would tend to fracture the CaF_2 crystal. Ultimately, we discovered that two gaskets were worse in terms of temperature equilibration than one. The best results were obtained by heating the entire copper housing, indium gasket, and window to the melting point of indium (157 C), and allowing the window to sink down into the melting gasket, and thereby matching the two surfaces perfectly.[2] Although the two surfaces now conform, the indium does not actually stick to the copper, so we add a viton gasket above the window to compress it to the bottom of the holder during installation.

Figure 5.17: Cross section of new window housing. This configuration gave the best results for equilibrating the window and copper holder temperatures, even though contact with the retaining ring surface area has now shrunk to nothing because of the viton o-ring.

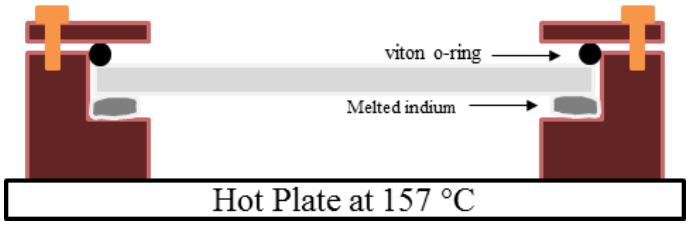

This gasket of course loses elasticity at cryogenic temperatures and is only used to prevent separation of the window and copper when the window is being mounted. With this procedure the

[2] The window must be heated along with the copper holder and indium wire, since dropping the window into a hot copper holder will cause it to shatter from heat shock.

edge of the window and the center finally became equilibrated and we were able to grow a crystal.

Chapter 6

Matrix FTIR of a Buffer-Gas Beam of Carbon Clusters

Detecting CH in a matrix FTIR setup can be a difficult proposition because of the reactivity of the molecule, the "average" strength of the transition, and the possibility of mixing the vibrational signal up with the CH-stretch mode of the precursors. We can learn a lot about our apparatus by attempting a simpler molecule instead. In our case, we chose to make a molecular beam of carbon clusters, made by ablating a graphite target.

Ablation of graphite will produce many different carbon clusters, some of which may take the form of long chains[122, 123]. Molecules that consist of long chains are likely to have large transition strengths, since vibrational transition strength is proportional to the change in dipole moment of the molecule, and since linear molecules can have bending modes in which the dipole moment changes more than for a compact molecule. Indeed, the transition strength of some molecules has been measured to be on the order of thousands of km/mole [124, 125]. The structure and vibrations of small [124, 126] and large [127] clusters are known, and have been measured in matrices [123, 128, 129], making for convenient line assignment. This makes carbon clusters a good molecule to work with for characterizing our apparatus.

Laser ablation has been successfully used to create carbon clusters in the past[122, 130], and we were able to reproduce the creation of carbon clusters ablating graphite. We mount a graphite target into the sample holder and ablate at 532 nm using 4 mJ/pulse power. The spectra we observe are affected by the scattering background due to crystals of poor optical quality (we show a photo in Fig.6.1, but we subtract it in order to determine relative signal strength. A spectrum is

shown in Fig.6.2.

Figure 6.1: A view of the neon crystal through the vacuum chamber and black body radiation shield. The fast crystallization of the neon on the window creates an opaque neon matrix (which is nonetheless transmissive enough for us to see absorption signals.

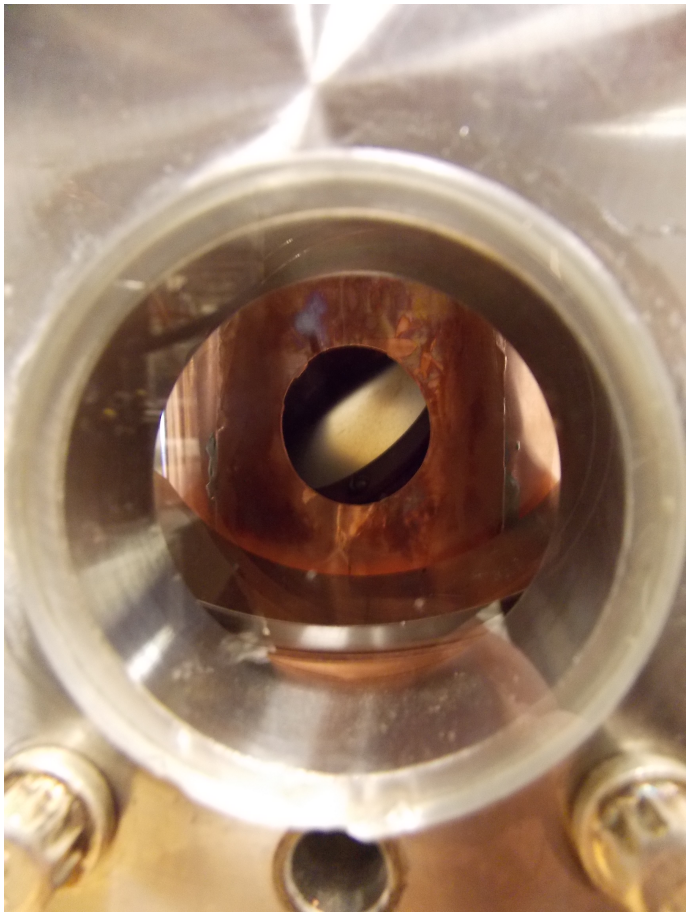

Figure 6.2: FTIR spectrum of carbon clusters embedded in neon. A graphite sample was ablated at 4 mJ/pulse while neon was flowed through a buffer gas cell at 70 sccm. The cell temperature was 34 K.

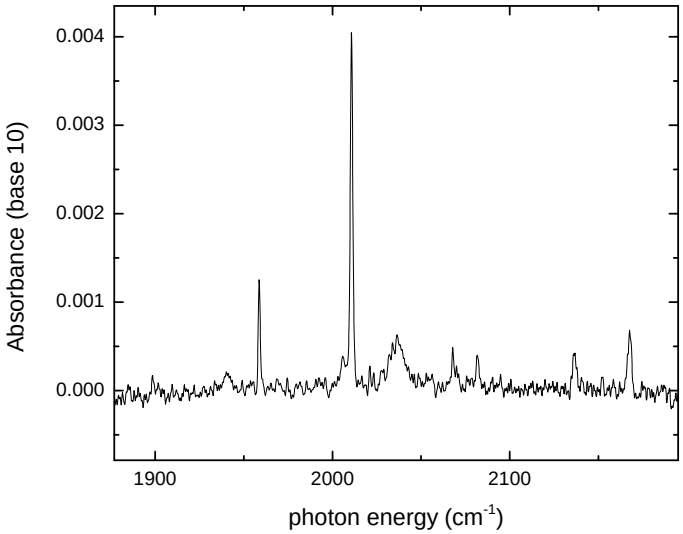

6.1 Peak Growth

We initially expected that peak height would grow linearly, as more and more clusters were deposited onto the crystal. However, we observed that the peak height would plateau on a timescale of about 15 min (Fig.6.3

Figure 6.3: The height of the $C_9(\nu_6)$ peak at 2010 cm^{-1} as a function of deposition time. The plateau in signal should be caused by a drop in cluster production, since the peak height is nowhere near 100% transmission.

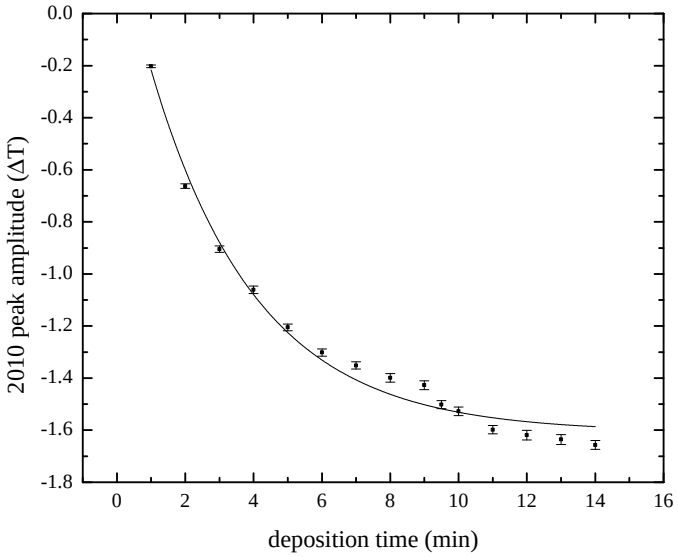

We suspected that the signal plateau was caused by "exhaustion" of the target by the ablation laser. Most groups who create molecules via ablation address this by rotating or translating the ablation target, but working at cryogenic temperatures forbids the use of any kind of moving target housing. Although we tried to raster the position of the laser spot by hand, it was difficult to do this consistently, and we eventually began to observe decreased signal sizes after weeks of operation. When we disassembled the target the surface appeared to have undergone significant chemical changes (Fig.6.4)

Figure 6.4: A picture of the surface of the graphite target after undergoing many hours of ablation. The target is 5 mm across, and the laser is focused to about a 50 um spot size.

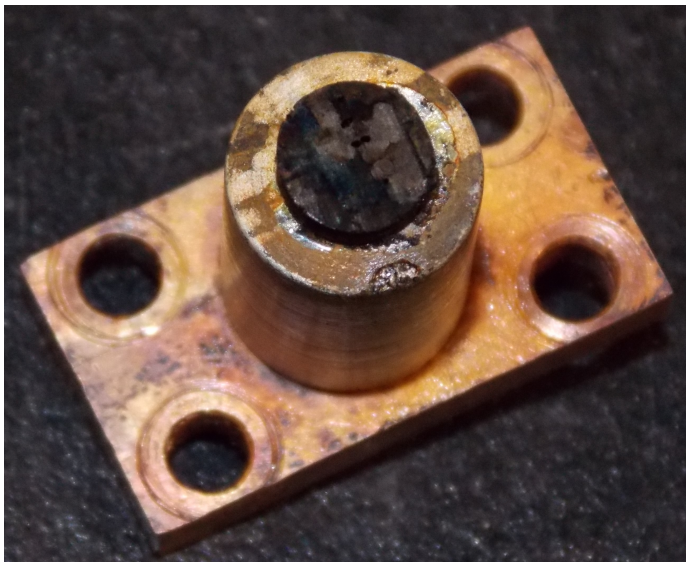

It is interesting that many of the features on the target surface are much larger than the laser spot size, pointing to the face that only a little laser fluence is required to "destroy" the target through heating. Many groups who ablate targets often have to resort to moving either the target or ablation laser in order to present a fresh portion of precursor to the laser spot. In our case, the low temperature of the cell prohibits easy sample movement, so moving the laser spot is our only option. We installed stepper motors on the mirror mount just before the lens and caused the laser spot to move across the sample during deposition. This had the effect of making line intensity grow, if not linearly, then on a much longer timescale than previously. This seems to have affected all vibrational modes uniformly, but new lines appear as they emerge above the noise. A spectrum of clusters with scanning is shown in Fig.6.5. We summarize the modes we observe in Tab.6.1.

Figure 6.5: FTIR spectrum of carbon clusters embedded in neon, now with ablation laser scanning across the sample. A graphite sample was ablated at 2 mJ/pulse while neon was flowed through a buffer-gas cell at 60 sccm. The cell temperature was 34 K.

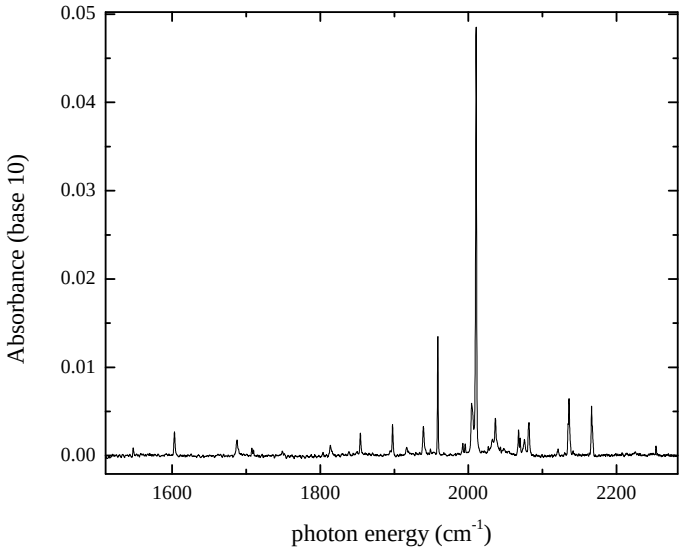

As we mentioned in Ch. 5, part of our motivation behind using matrix isolation to detect molecules is the potential to improve our signal to noise by continuously depositing molecules in the isolation crystal and waiting for adequate peak growth. It is therefore heartening that, barring "exhaustion" of the ablation sample, the carbon cluster vibrational signals do indeed continue to grow, and that we are not yet limited by scattering of the incident beam, or by other effects like crystal sublimation.

Line Position (cm^{-1})	Molecule	Vibrational mode	IR intensity (km/mole)
1603	C_9	ν_7	394[123]
1813	C_{13}		
1853	C_{11}	ν_8	
1897	C_7	ν_5	1307[123]
1939	C_{11}	ν_7	
1958.7	C_6	ν_4	1073[123]
2004	C_{12}		
2010	C_9	ν_6	6520[123]
2036	C_3	ν_3	772[123],612[131]
2068	C_8	ν_5	1989[123]
2081	C_9	ν_5	704[132]
2135	C_7	ν_4	4652[123]
2166	C_5	ν_3	1649[131]2539[123]

Table 6.1: A summary of the vibrational modes of carbon clusters observed after ablation with laser scanning an deposition onto a cold window. IR intensities are quoted where available.

Taking into account the IR intensities reported for carbon clusters in [123] we can extract the relative abundances of each cluster in each vibrational mode. These are shown in fig.6.6

Figure 6.6: Peak absorption of each cluster scaled by the infrared intensity and normalized to the largest abundance. It should be noted that calculations of the IR intensity of the C_9,ν_6 mode have yielded results different by many orders of magnitude. [132] measured the intensity *relative* to the height of the peak at 2010 cm^{-1}, which was used to calculate the abundance of C_9 from this mode, although there is clearly some error.

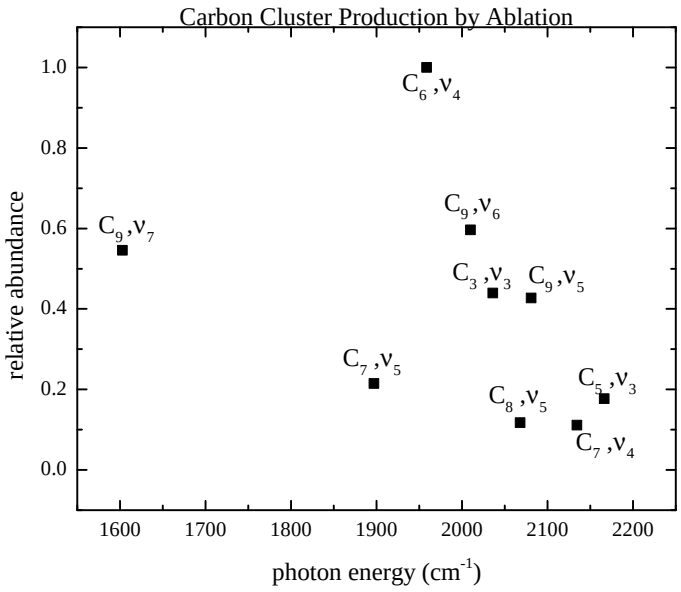

It seems that ablation produces similar amounts of each type of cluster. Using the results of Ch. 5 to extract the number of absorbers we find that we make 2×10^{13} C_6 molecules (most abundant) and 1.6×10^{12} C_9 molecules (least abundant). We know from our work in Ch. 2 that we make large amounts of C_2, but as its vibrational modes are not IR-active, we are not sensitive to them. Studies of carbon cluster production with laser vaporization have been conducted, but have achieved very disparate results in the relative abundances of the clusters produced [122], [133] (at first glance these sources use much larger ablation energies, but they are unfocused, whereas we focus 2 mJ/pulse onto a small spot size).

6.2 Reactions

Occasionally, if there is a leak in the vacuum chamber or if the neon lines have not sufficiently been pumped out, there can be contamination of the system with other gases. Early on in our carbon cluster investigations, we deposited a crystal that had significant CO_2 contamination. As discussed in Ch.5 a crystal is below the annealing temperature will be rigid enough to prevent molecule migration and reaction, but since we have a heater on the window holder we can control this to some extent. In this case, after depositing the CO contaminated carbon cluster beam, we heated the crystal to just above the annealing temperature at 10 K, and then re-froze it to take another spectrum. The results are shown in Fig.6.7.

Figure 6.7: Reactions in a crystal of C clusters in Ne with CO contamination, after annealing to 11 K and re-freezing. The CO peak is completely depleted and new peaks appear, although we were unable to assign them with certainty. We believe there were also some reactions involving just clusters, as some cluster peaks are partially depleted while the C_9 peak grows. No deposition or ablation occurred during the annealing/re-freezing process.

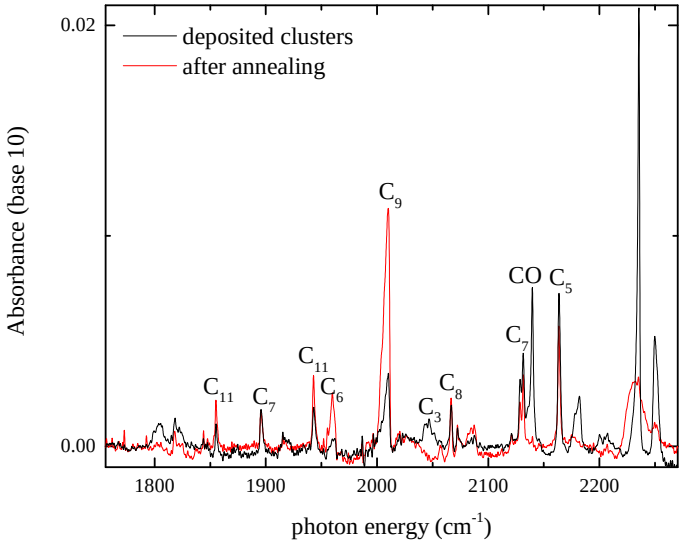

Unfortunately, we were unable to assign many of the peaks which participated, but it seems that at least some of the carbon clusters combined or fragmented to form C_9. This instance was not

really a controlled-enough experiment to be able to characterize any one reaction, but we believe this is a good proof-of-principle case that reactions can be studied using this source with a matrix isolated environment. Better candidates for such work might include simpler molecules with fewer vibrational modes with reaction partners whose abundance in the crystal could be more precisely controlled. In particular the CH+O_2 reactions discussed in Ch.2 would be almost ideal because of CH's one vibrational mode, although the amount of O_2 would have to be estimated, since O_2 is not IR active.

6.3 Conclusions and Further Work

We have created a buffer-gas beam of molecules, deposited it into a neon matrix, and observed the vibrational spectra of the constituents. The apparatus is promising for its ability to characterize the content of molecular beam output, and is therefore an excellent source work experiment, since it has the capability to identify many beam constituents without the experimenter knowing they would be present beforehand and testing for the existence of each one with a species-specific protocol. We have also shown that this is a suitable environment for observing reactions of molecules on the matrix surface.

6.3.1 Characterization

This is of course just the beginning realization of this experiment. Much more work needs to be done toward stabilizing molecule signals and characterizing the experiment parameters. One problem that we consistently run into is our lack of knowledge about how radicals are distributed over the window surface. Knowing the angular distribution is vital for coupling such a beam into a decelerator, since it sets limits on the hexapole parameters, ultimate molecule density per well, etc. It certainly looks as though the entire window is covered, but we suspect that much of the neon that flows out of the cell does not actually stick to the window on its first collision, but instead diffuses through the vacuum chamber and re-condenses on all the coldest surfaces. Technically the

angular distribution of molecular beam density n should be given by [47]

$$n(R,\theta) = n(R,0)cos^2\left(\frac{\pi\theta}{2\phi}\right) \tag{6.1}$$

where $n(r,0)$ is the longitudinal density of the beam and ϕ is the opening angle of the beam, usually $\approx 79°$. However, we are unable to verify this because we do not have the capability of tuning the IR beam alignment in a controlled way. Because the beam output is that of a lamp an not a laser, it is difficult to contain all of the beam energy with conventional optics. What is more, once optics are used to direct the beam out of the spectrometer for alignment control, it becomes much more difficult to purge the beam path, causing significant problems with background subtraction. However, all of these difficulties amount only to design challenges which could in principle be overcome to allow us to scan over the window surface and map out the dependence of molecule density on angle.

Another aspect of this experiment in need of characterization is the efficiency with which we produce molecules with ablation. Clearly ablation has the *potential* to make interesting molecules at rates high enough for us to see them. However, when we attempted to look for CH with this experiment, we were unable to detect it. The best way to characterize the ablation and entrainment of molecules within our beam would be to use a precursor whose ablation products and branching ratios are known. If the ultimate goal is detecting CH, then we need to be able to see how well we can detect molecules with very small probabilities of being created in the ablation process.

6.3.2 Reactions

The possibility of looking at reactions on the surface should be explored in more detail. The apparatus can be modified such that the addition of a reaction partner is more controlled- this can be accomplished with the addition of a second, room temperature pulsed valve, or simply tube flowing gas over the window. If a second pulsed valve is used, consideration must be given to how much space it will occupy, whether it will reduce the optical access of the beam, and how additional heat load it will provide in the form of black body radiation. The tube option obviates many of

these concerns, as it can be made much smaller, and can even be anchored to the first stage to reduce heat load (if the reaction partner does not freeze at 40 K).

6.3.3 Gas Phase Spectroscopy

One of the greatest limitations of this experiment is that it cannot tell us much about the internal temperature of the beam. Even if we could somehow do this with vibrational spectroscopy, trapping the molecules in the neon matrix removes information about their temperature in the beam, and broadens and distorts transition signatures because of (admittedly weak) interactions with the substrate. The translational and rotational temperatures can only be probed with gas phase spectroscopy, by looking at Doppler broadening and rotation state-specific detection. Although knowing these beam characteristics is not absolutely essential for our eventual goal of coupling a buffer-gas beam into a Stark decelerator, they are useful for conducting trapping experiments. In fact, our group is currently working on building a buffer-gas beam experiment in which molecules will be detected by IR absorption spectroscopy using a quantum cascade laser. The laser will be much more sensitive to gas phase molecule densities, which eliminates the need for matrix isolation.

Bibliography

[1] S. Truppe, R.J. Hendricks, S.K. Tokunaga, H.J. Lewandowski, M.G. Kozlov, Christian Henkel, E.A. Hinds, and M.R. Tarbutt. A search for varying fundamental constants using hertz-level frequency measurements of cold CH molecules. Nature Communications, 4:2600, 2013.

[2] Lincoln D Carr, David DeMille, Roman V Krems, and Jun Ye. Cold and ultracold molecules: science, technology and applications. New Journal of Physics, 11(5):055049, 2009.

[3] N. Balakrishnan. Perspective: Ultracold molecules and the dawn of cold controlled chemistry. The Journal of Chemical Physics, 145(15):150901, 2016.

[4] John M. Doyle, Bretislav Friedrich, and Edvardas Narevicius. Physics and chemistry with cold molecules. ChemPhysChem, 17(22):3581–3582, 2016.

[5] Sebastiaan Y. T. van de Meerakker, Hendrick L. Bethlem, and Gerard Meijer. Taming molecular beams. Nature Physics, 4:595–602, 2008.

[6] Justin Jankunas and Andreas Osterwalder. Cold and controlled molecular beams: Production and applications. Annual Review of Physical Chemistry, 66(1):241–262, 2015.

[7] Deborah S. Jin and Jun Ye. Introduction to ultracold molecules: New frontiers in quantum and chemical physics. Chemical Reviews, 112(9):4801–4802, 2012.

[8] N. Balakrishnan and A. Dalgarno. Chemistry at ultracold temperatures. Chemical Physics Letters, 341(56):652 – 656, 2001.

[9] E Bodo, F A Gianturco, N Balakrishnan, and A Dalgarno. Chemical reactions in the limit of zero kinetic energy: virtual states and Ramsauer minima in $F + H_2 \rightarrow HF + H$. Journal of Physics B: Atomic, Molecular and Optical Physics, 37(18):3641, 2004.

[10] Fangtong Zhang, Pavlo Maksyutenko, and Ralf I. Kaiser. Chemical dynamics of the $CH(X^2\Pi) + C_2H_4(X^1A_{1g})$, $CH(X^2\Pi) + C_2D_4(X^1A_{1g})$, and $CD(X^2\Pi) + C_2H_4(X^1A_{1g})$ reactions studied under single collision conditions. Physical Chemistry Chemical Physics, 14:529–537, 2012.

[11] Michael R. Berman, J.W. Fleming, A.B. Harvey, and M.C. Lin. Temperature dependence of the reactions of CH radicals with unsaturated hydrocarbons. Chemical Physics, 73(12):27 – 33, 1982.

[12] A. Canosa, I.R. Sims, D. Travers, I.W.M. Smith, and B.R. Rowe. Reactions of the methylidine radical with $CH_4, C_2H_2, C_2H_4, C_2H_6$, and but-1-ene studied between 23 and 295 K with a CRESU apparatus. Astronomy and Astrophysics, 323(2):644–651, 1997.

[13] Zhi-Xiang Wang and Ming-Bao Huang. Insertion of methylidyne into the CH bond of ethylene. Chemical Physics Letters, 291(34):381 – 386, 1998.

[14] Frank Filsinger, Jochen Kuepper, Gerard Meijer, Jonas Hansen, Jochen Maurer, Jens Nielsen, Lotte Holmegaard, and Henrik Stapelfeldt. Pure samples of individual conformers: The separation of stereoisomers of complex molecules using electric fields. Angewandte Chemie International Edition, 48(37):6900–6902, 2009.

[15] Daniel Roesch, Stefan Willitsch, Yuan-Pin Chang, and Jochen Kuepper. Chemical reactions of conformationally selected 3-aminophenol molecules in a beam with coulomb-crystallized Ca^+ ions. The Journal of Chemical Physics, 140(12):124202, 2014.

[16] Yuan-Pin Chang, Daniel A. Horke, Sebastian Trippel, and Jochen Kuepper. Spatially-controlled complex molecules and their applications. International Reviews in Physical Chemistry, 34(4):557–590, 2015.

[17] Roman V. Krems. Molecules near absolute zero and external field control of atomic and molecular dynamics. International Reviews in Physical Chemistry, 24(1):99–118, 2005.

[18] Roman Krems, Bretislav Friedrich, and William C Stwalley. Cold molecules: theory, experiment, applications. CRC press, 2009.

[19] Ralf I. Kaiser. Experimental investigation on the formation of carbon-bearing molecules in the interstellar medium via neutralneutral reactions. Chemical Reviews, 102(5):1309–1358, 2002.

[20] TPM Goumans, C Richard A Catlow, Wendy A Brown, Johannes Kästner, and Paul Sherwood. An embedded cluster study of the formation of water on interstellar dust grains. Physical Chemistry Chemical Physics, 11(26):5431–5436, 2009.

[21] Murray J. McEwan, Graham B. I. Scott, Nigel G. Adams, Lucia M. Babcock, R. Terzieva, and Eric Herbst. New H and H_2 reactions with small hydrocarbon ions and their roles in benzene synthesis in dense interstellar clouds. The Astrophysical Journal, 513(1):287, 1999.

[22] G. Pineau des Forets, E. Roueff, and D. R. Flower. The formation of nitrogen-bearing species in dark interstellar clouds. Monthly Notices of the Royal Astronomical Society, 244:668–674, 1990.

[23] C.M. Walmsley and H. Ungerechts. Ammonia as a molecular cloud thermometer. Astronomy and Astrophysics, 122:164–170, 1983.

[24] Michael D. Hoops and Bruce S. Ault. Matrix isolation study of the early intermediates in the ozonolysis of cyclopentene and cyclopentadiene: Observation of two Criegee intermediates. Journal of the American Chemical Society, 131(8):2853–2863, 2009.

[25] Marilyn E. Jacox. The spectroscopy of molecular reaction intermediates trapped in the solid rare gases. Chemical Society Reviews, 31:108–115, 2002.

[26] David Johnson and George Marston. The gas-phase ozonolysis of unsaturated volatile organic compounds in the troposphere. Chem. Soc. Rev., 37:699–716, 2008.

[27] T. J. Wallington, W. F. Schneider, J. Sehested, M. Bilde, J. Platz, O. J. Nielsen, L. K. Christensen, M. J. Molina, L. T. Molina, and P. W. Wooldridge. Atmospheric chemistry of HFE-7100 ($C_4F_9OCH_3$): reaction with oh radicals, UV spectra and kinetic data for $C_4F_9OCH_2$ and $C_4F_9OCH_2O_2$ radicals, and the atmospheric fate of $C_4F_9OCH_2O$ radicals. The Journal of Physical Chemistry A, 101(44):8264–8274, 1997.

[28] L. Vereecken, H. Harder, and A. Novelli. The reaction of criegee intermediates with NO, RO_2, and SO_2, and their fate in the atmosphere. Physical Chemistry Chemical Physics, 14:14682–14695, 2012.

[29] Eric R Hudson, HJ Lewandowski, Brian C Sawyer, and Jun Ye. Cold molecule spectroscopy for constraining the evolution of the fine structure constant. Physical review letters, 96(14):143004, 2006.

[30] F. Hoogeveen. The standard model prediction for the electric dipole moment of the electron. Nuclear Physics B, 341(2):322 – 340, 1990.

[31] Jonathan Engel, Michael J. Ramsey-Musolf, and U. van Kolck. Electric dipole moments of nucleons, nuclei, and atoms: The standard model and beyond. Progress in Particle and Nuclear Physics, 71:21 – 74, 2013.

[32] Edmund R Meyer and John L Bohn. Prospects for an electron electric-dipole moment search in metastable ThO and ThF^+. Physical Review A, 78(1):010502, 2008.

[33] Jacob Baron, Wesley C Campbell, David DeMille, John M Doyle, Gerald Gabrielse, Yulia V Gurevich, Paul W Hess, Nicholas R Hutzler, Emil Kirilov, Ivan Kozyryev, et al. Order of magnitude smaller limit on the electric dipole moment of the electron. Science, 343(6168):269–272, 2014.

[34] L. R. Hunter, S. K. Peck, A. S. Greenspon, S. Saad Alam, and D. DeMille. Prospects for laser cooling TlF. Physical Review A, 85:012511, 2012.

[35] V. Zhelyazkova, A. Cournol, T. E. Wall, A. Matsushima, J. J. Hudson, E. A. Hinds, M. R. Tarbutt, and B. E. Sauer. Laser cooling and slowing of CaF molecules. Physical Review A, 89:053416, 2014.

[36] E.S. Schuman, J.F. Barry, and D. DeMille. Laser cooling of a diatomic molecule. Nature, 467:820–823, 2010.

[37] Matthew T. Hummon, Mark Yeo, Benjamin K. Stuhl, Alejandra L. Collopy, Yong Xia, and Jun Ye. 2D magneto-optical trapping of diatomic molecules. Physical Review Letters, 110:143001, 2013.

[38] Mark Yeo, Matthew T. Hummon, Alejandra L. Collopy, Bo Yan, Boerge Hemmerling, Eunmi Chae, John M. Doyle, and Jun Ye. Rotational state microwave mixing for laser cooling of complex diatomic molecules. Physical Review Letters, 114:223003, 2015.

[39] Valentina Zhelyazkova, Anne Cournol, Thomas E Wall, Aki Matsushima, Jonathan J Hudson, EA Hinds, MR Tarbutt, and BE Sauer. Laser cooling and slowing of CaF molecules. Physical Review A, 89(5):053416, 2014.

[40] D Wang, J Qi, MF Stone, O Nikolayeva, H Wang, B Hattaway, SD Gensemer, PL Gould, EE Eyler, and WC Stwalley. Photoassociative production and trapping of ultracold KRb molecules. Physical review letters, 93(24):243005, 2004.

[41] K-K Ni, S Ospelkaus, MHG De Miranda, A Pe'Er, B Neyenhuis, JJ Zirbel, S Kotochigova, PS Julienne, DS Jin, and Jun Ye. A high phase-space-density gas of polar molecules. Science, 322(5899):231–235, 2008.

[42] Stephan D Kraft, Peter Staanum, Jörg Lange, Leif Vogel, Roland Wester, and Matthias Weidemüller. Formation of ultracold LiCs molecules. Journal of Physics B: Atomic, Molecular and Optical Physics, 39(19):S993, 2006.

[43] Paul D Lett, Kristian Helmerson, WD Phillips, LP Ratliff, Steven L Rolston, and Mark E Wagshul. Spectroscopy of Na_2 by photoassociation of laser-cooled Na. Physical review letters, 71(14):2200, 1993.

[44] Dima Egorov, Thierry Lahaye, Wieland Schöllkopf, Bretislav Friedrich, and John M Doyle. Buffer-gas cooling of atomic and molecular beams. Physical Review A, 66(4):043401, 2002.

[45] Hsin-I Lu, Julia Rasmussen, Matthew J Wright, Dave Patterson, and John M Doyle. A cold and slow molecular beam. Physical Chemistry Chemical Physics, 13(42):18986–18990, 2011.

[46] Wesley C Campbell and John M Doyle. Cooling, trap loading, and beam production using a cryogenic helium buffer gas. CRC press, 2009.

[47] N. R. Hutzler, H.-I Lu, , and J. M. Dolye. The buffer gas beam: An intense, cold, and slow source for atoms and molecules. Chemical Reviews, 9:4803, 2012.

[48] David Patterson, Julia Rasmussen, and John M Doyle. Intense atomic and molecular beams via neon buffer-gas cooling. New Journal of Physics, 11(5):055018, 2009.

[49] R A Phaneuf, C C Havener, G H Dunn, and A Mller. Merged-beams experiments in atomic and molecular physics. Reports on Progress in Physics, 62(7):1143, 1999.

[50] Alexander M. Mebel and Ralf I. Kaiser. Formation of resonantly stabilised free radicals via the reactions of atomic carbon, dicarbon, and tricarbon with unsaturated hydrocarbons: theory and crossed molecular beams experiments. International Reviews in Physical Chemistry, 34(4):461–514, 2015.

[51] Benjamin Bertsche, Justin Jankunas, and Andreas Osterwalder. Low-temperature collisions between neutral molecules in merged molecular beams. CHIMIA International Journal for Chemistry, 68(4), 2014.

[52] A. B. Henson, S. Gersten, Y. Shagam, J. Narevicius, and E. Narevicius. Observation of resonances in penning ionization reactions at Sub-Kelvin temperatures in merged beams. Science, 338(6104):234–238, 2012.

[53] Pavlo Maksyutenko, Fangtong Zhang, Xibin Gu, and Ralf I. Kaiser. A crossed molecular beam study on the reaction of methylidyne radicals $CH(X^2\Pi)$ with acetylene $C_2H_2(X^1\Sigma^{g+})$-competing $C_3H_2 + H$ and $C_3H + H_2$ channels. Physical Chemistry Chemical Physics, 13:240–252, 2011.

[54] Edvardas Narevicius and Mark G. Raizen. Toward cold chemistry with magnetically decelerated supersonic beams. Chemical Reviews, 112(9):4879–4889, 2012.

[55] Yuval Shagam and Edvardas Narevicius. Sub-kelvin collision temperatures in merged neutral beams by correlation in phase-space. The Journal of Physical Chemistry C, 117(43):22454–22461, 2013.

[56] Sebastiaan Y. T. van de Meerakker, Nicolas Vanhaecke, and Gerard Meijer. Stark deceleration and trapping of OH radicals. Annual Review of Physical Chemistry, 57:159–190, 2006.

[57] N. J. Fitch and M. R. Tarbutt. Principles and design of a Zeeman Sisyphus decelerator for molecular beams. ChemPhysChem, 17(22):3609–3623, 2016.

[58] S. Chervenkov, X. Wu, J. Bayerl, A. Rohlfes, T. Gantner, M. Zeppenfeld, and G. Rempe. Continuous centrifuge decelerator for polar molecules. Physical Review Letters, 112:013001, 2014.

[59] J. R. Bochinski, Eric R. Hudson, H. J. Lewandowski, Gerard Meijer, and Jun Ye. Phase space manipulation of cold free radical OH molecules. Physical Review Letters, 91:243001, 2003.

[60] Brian C. Sawyer, Benjamin L. Lev, Eric R. Hudson, Benjamin K. Stuhl, Manuel Lara, John L. Bohn, and Jun Ye. Magnetoelectrostatic trapping of ground state OH molecules. Physical Review Letters, 98:253002, 2007.

[61] Kirstin Wohlfart, Frank Filsinger, Fabian Grätz, Jochen Küpper, and Gerard Meijer. Stark deceleration of OH radicals in low-field-seeking and high-field-seeking quantum states. Physical Review A, 78:033421, 2008.

[62] Steven Hoekstra, Markus Metsälä, Peter C. Zieger, Ludwig Scharfenberg, Joop J. Gilijamse, Gerard Meijer, and Sebastiaan Y. T. van de Meerakker. Electrostatic trapping of metastable NH molecules. Physical Review A, 76:063408, 2007.

[63] J. Riedel, S. Hoekstra, W. Jäger, J. J. Gilijamse, S. Y. T. van de Meerakker, and G. Meijer. Accumulation of stark-decelerated NH molecules in a magnetic trap. The European Physical Journal D, 65(1):161–166, 2011.

[64] L. P. Parazzoli, N. J. Fitch, P. S. Żuchowski, J. M. Hutson, and H. J. Lewandowski. Large effects of electric fields on atom-molecule collisions at millikelvin temperatures. Physical Review Letters, 106:193201, 2011.

[65] J. Peter Toennies and Andrey F. Vilesov. Superfluid helium droplets: A uniquely cold nanomatrix for molecules and molecular complexes. Angewandte Chemie International Edition, 43(20):2622–2648, 2004.

[66] M. Y. Choi, G. E. Douberly, T. M. Falconer, W. K. Lewis, C. M. Lindsay, J. M. Merritt, P. L. Stiles, and R. E. Miller. Infrared spectroscopy of helium nanodroplets: novel methods for physics and chemistry. International Reviews in Physical Chemistry, 25(1-2):15–75, 2006.

[67] Vladimir E. Bondybey, Alice M. Smith, and Juergen Agreiter. New developments in matrix isolation spectroscopy. Chemical Reviews, 96(6):2113–2134, 1996.

[68] James A. de Haseth Peter R. Griffiths. Fourier Transform Infrared Spectrometry. Wiley, 2007.

[69] Ian R Dunkin. Matrix-isolation techniques: a practical approach. Oxford University Press, 1998.

[70] Isaac F Silvera. The solid molecular hydrogens in the condensed phase: Fundamentals and static properties. Reviews of Modern Physics, 52(2):393, 1980.

[71] Marilyn E. Jacox. The spectroscopy of molecular reaction intermediates trapped in the solid rare gases. Chem. Soc. Rev., 31:108–115, 2002.

[72] Martin T Bell and Timothy P. Softley. Ultracold molecules and ultracold chemistry. Molecular Physics, 107(2):99–132, 2009.

[73] Richard A. Brownsword, Ian R. Sims, Ian W. M. Smith, David W. A. Stewart, André Canosa, and Bertrand R. Rowe. The radiative association of CH with H_2: A mechanism for formation of CH_3 in interstellar clouds. Astrophys. J., 485(1):195, 1997.

[74] Ian W.M. Smith. Laboratory astrochemistry: Gas-phase processes. Annual Review of Astronomy and Astrophysics, 49(1):29–66, 2011.

[75] Jean-Christophe Loison and Astrid Bergeat. Rate constants and the h atom branching ratio of the reactions of the methylidyne CH($X^2\Pi$) radical with C_2H_2, C_2H_4, C_3H_4 (methylacetylene and allene), C_3H_6 (propene), and C_4H_8 (trans-butene). Physical Chemistry Chemical Physics, 11:655–664, 2009.

[76] Gerhard Herzberg. The Spectra and Structures of Simple Free Radicals. Dover, 1971.

[77] John M. Brown and Alan Carrington. Rotational Spectroscopy of Diatomic Molecules. Cambridge University Press, 2003.

[78] M.I. Fabrikant, Tian Li, N.J. Fitch, N. Farrow, Jonathan D. Weinstein, and H. J. Lewandowski. Method for traveling-wave deceleration of buffer gas beams of CH. Physical Review A, 90:033418, 2014.

[79] J. Brzozowski, P. Bunker, N. Elander, and P. Erman. Predissociation effects in the A, B, and C states of CH and the interstellar formation rate of CH via inverse predissociation. Astrophysical Journal, 207:414–424, 1976.

[80] Detection of CH in an expanding argon/acetylene plasma using cavity ring down absorption spectroscopy. Chemical Physics Letters, 310(56):405 – 410, 1999.

[81] Linda G. Blevins, Michael W. Renfro, Kent H. Lyle, Normand M. Laurendeau, and Jay P. Gore. Experimental study of temperature and CH radical location in partially premixed CH_4 air coflow flames. Combustion and Flame, 118(4):684 – 696, 1999.

[82] K.P. Huber, G. Herzberg (data prepared by J.W. Gallagher, and R.D. Johnson III). NIST Chemistry WebBook, NIST Standard Reference Database Number 69, chapter Constants of Diatomic Molecules. National Institute of Standards and Technology, Gaithersburg MD, 20899, 2017.

[83] Igor Derzy, Vladimir A. Lozovsky, and Sergey Cheskis. Absolute CH concentration in flames measured by cavity ring-down spectroscopy. Chemical Physics Letters, 306:319–324, 1999.

[84] Yumin Wang, Leping Li, and William A. Chupka. (2+1) resonance-enhanced multiphoton ionization studies of the CH $D^2\Pi$(v = 2) state. Chemical Physics Letters, 192:348–352, 1992.

[85] Joseph M. Beames, Fang Liu, Marsha I. Lester, and Craig Murray. Communication: A new spectroscopic window on hydroxyl radicals using UV + VUV resonant ionization. The Journal of Chemical Physics, 134(24):241102, 2011.

[86] Travis Crain Briles. Production, Deceleration, and Detection of OH Radicals. PhD thesis, University of Colorado, 2015.

[87] Karl K. Irikura. Experimental vibrational zero-point energies: Diatomic molecules. Journal of Physical and Chemical Reference Data, 36(2):389–397, 2007.

[88] Thanh Lam Nguyen, Alexander M. Mebel, Sheng H. Lin, and Ralf I. Kaiser. Product branching ratios of the C(3P) + C_2H_3(2A) and CH($^2\Pi$) + C_2H_2($^1\Sigma_g^+$) reactions and photodissociation of $H_2CCCH(^2B_1)$ at 193 and 242 nm: an ab initio/RRKM study. The Journal of Physical Chemistry A, 105(51):11549–11559, 2001.

[89] Yuri P Raizer and John E Allen. Gas discharge physics, volume 2. Springer Berlin, 1997.

[90] Michael S. Brown and Robert A. Forlines. Measurement of CH density in a pulsed-dc hydrocarbon-gas-mixture discharge. Journal of Applied Physics, 97:103302, 2005.

[91] A. Tanabashi, T. Hirao, T. Amano, and P. F. Bernath. The swan system of C_2: A global analysis of fourier transform emission spectra. The Astrophysical Journal, 169:472–484, 2007.

[92] Li Sheng-Qiang, Xu Liang, Chen Yang-Qin, Deng Lian-Zhong, and Yin Jian-Ping. Production of CH($A^2\Delta$) by multi-photon dissociation of $(CH_3)_2CO, CH_3NO_2, CH_2Br_2$, and $CHBr_3$ at 213 nm. Chinese Physics B, 23(8):083701, 2014.

[93] C. Romanzin, S. Boye-Peronne, D. Gauyacq ad Y. Benilan, M.-C. Gazeau, and S. Douin. CH radical production from 248nm photolysis or discharge-jet dissociation of $CHBr_3$ probed by cavity ring-down absorption spectroscopy. Journal of Chemical Physics, 125:114312, 2006.

[94] Mark A. Blitz, Daniel G. Johnson, Michelle Pesa, Michael J. Pilling, Struan H. Robertson, and Paul W. Seakins. Reaction of CH radicals with methane isotopomers. J. Chem. Soc., Faraday Trans., 93:1473–1479, 1997.

[95] DH Phelps and FW Dalby. Experimental determination of the electric dipole moment of the ground electronic state of CH. Physical Review Letters, 16(1):3, 1966.

[96] Noah Fitch. Traveling-Wave Stark-Decelerated Molecular Beams for Cold Collision Experiments. PhD thesis, University of Colorado, 2013.

[97] L P Parazzoli, N Fitch, D S Lobser, and H J Lewandowski. High-energy-resolution molecular beams for cold collision studies. New Journal of Physics, 11(5):055031, 2009.

[98] Sebastiaan Y. T. van de Meerakker, Nicolas Vanhaecke, Hendrick L. Bethlem, and Gerard Meijer. Transverse stability in a stark decelerator. Physical Review A, 73:023401, 2006.

[99] David Patterson. Buffer Gas Cooled Beams and Cold Molecular Collisions. PhD thesis, Harvard University, 2010.

[100] Hsin-I Lu. Magnetic Trapping of Molecules via Optical Loading and Magnetic Slowing. PhD thesis, Harvard University, 2013.

[101] Nick Hutzler. A New Limit on the Electron Dipole Moment. PhD thesis, Harvard University, 2014.

[102] Jonathan David Weinstein. Magnetic Trapping of Atomic Chromium and Molecular Calcium Monohydride. PhD thesis, Harvard University, 2001.

[103] Xianglei L. Mao, Mark A. Shannon, Alberto J. Fernandez, and Richard E. Russo. Temperature and emission spatial profiles of laser-induced plasmas during ablation using time-integrated emission spectroscopy. Applied Spectroscopy, 49(7):1054–1062, 1995.

[104] Richard E. Russo. Laser ablation. Applied Spectroscopy, 49(9):14A–28A, 1995.

[105] B.H. Bransden and C.J. Joachain. Physics of Atoms and Molecules. Pearson, 2003.

[106] L.D. Landau and E.M. Lifshitz. Course of Theoretical Physics Vol. 3: Quantum Mechanics. Pergamon Press, 1977.

[107] Seymour Rosin and I. I. Rabi. Effective collision cross sections of the alkali atoms in various gases. Physical Review, 48:373–379, 1935.

[108] Robert W Molof, Henry L Schwartz, Thomas M Miller, and Benjamin Bederson. Measurements of electric dipole polarizabilities of the alkali-metal atoms and the metastable noble-gas atoms. Physical Review A, 10(4):1131, 1974.

[109] Erhard W Rothe, PK Rol, and Richard B Bernstein. Interaction potentials from the velocity dependence of total atom-atom scattering cross sections. Physical Review, 130(6):2333, 1963.

[110] Fernando Pirani, Simona Brizi, Luiz F. Roncaratti, Piergiorgio Casavecchia, David Cappelletti, and Franco Vecchiocattivi. Beyond the Lennard-Jones model: a simple and accurate potential function probed by high resolution scattering data useful for molecular dynamics simulations. Physical Chemistry Chemical Physics, 10:5489–5503, 2008.

[111] F. Thibault, D. Cappelletti, F. Pirani, G. Blanquet, and M. Bartolomei. Molecular-beam scattering and pressure broadening cross sections for the acetylene-neon system. The European Physical Journal D, 44(2):337–344, 2007.

[112] Vincenzo Aquilanti, Elena Cornicchi, Marc Moix Teixidor, Nadja Saendig, Fernando Pirani, and David Cappelletti. Glory-scattering measurement of water- Noble-gas interactions: The birth of the hydrogen bond. Angewandte Chemie International Edition, 44(16):2356–2360, 2005.

[113] R.H. Tipping and R.M. Herman. Impact theory for the noble gas pressure-induced HCl vibration-rotation and pure rotation line widthsi. Journal of Quantitative Spectroscopy and Radiative Transfer, 10(8):881 – 896, 1970.

[114] Petr Slavek, Pavel Jungwirth, Marius Lewerenz, N. Hendrik Nahler, Michal Frnk, and Udo Buck. Pickup and photodissociation of hydrogen halides in floppy neon clusters. The Journal of Physical Chemistry A, 107(39):7743–7754, 2003.

[115] L. Pang and F. Brisse. Endohedral energies and translation of fullerene-noble gas clusters G@Cn (G = helium, neon, argon, krypton and xenon; n = 60 and 70). The Journal of Physical Chemistry, 97(33):8562–8563, 1993.

[116] Erhard W. Rothe and Richard B. Bernstein. Total collision cross sections for the interaction of atomic beams of alkali metals with gases. The Journal of Chemical Physics, 31(6):1619–1627, 1959.

[117] D. G. Henshaw. Atomic distribution in liquid and solid neon and solid argon by neutron diffraction. Physical Review, 111:1470–1475, 1958.

[118] Sefik Szer and Lester Andrews. Ftir spectra of ammonia clusters in noble gas matrices. The Journal of Chemical Physics, 87(9):5131–5140, 1987.

[119] Sefik Süzer and Lester Andrews. FTIR spectra of ammonia clusters in noble gas matrices. The Journal of chemical physics, 87(9):5131–5140, 1987.

[120] Jacob Bigeleisen and Etienne Roth. Vapor pressures of the neon isotopes. The Journal of Chemical Physics, 35(1):68–77, 1961.

[121] J. Moore, C. Davis an M. Coplan, and S. Greer. Building Scientific Apparatus. Cambridge University Press, 2009.

[122] Eric A. Rohlfing, D. M. Cox, and A. Kaldor. Production and characterization of supersonic carbon cluster beams. The Journal of Chemical Physics, 81(7):3322–3330, 1984.

[123] Jan Szczepanski, Scott Ekern, and Martin Vala. Vibrational spectroscopy of small matrix-isolated linear carbon cluster anions. The Journal of Physical Chemistry A, 101(10):1841–1847, 1997.

[124] Alan Van Orden and Richard J. Saykally. Small carbon clusters: spectroscopy, structure, and energetics. Chemical Reviews, 98(6):2313–2358, 1998.

[125] Patrick Freivogel, Jan Fulara, Michael Jakobi, Daniel Forney, and John P. Maier. Electronic absorption spectra of linear carbon chains in neon matrices. II. C_{2n}^-, C_{2n}, and $C_{2n}H$.

[126] William Weltner and Richard J. Van Zee. Carbon molecules, ions, and clusters. Chemical Reviews, 89(8):1713–1747, 1989.

[127] Donald S. Bethune, Gerard Meijer, Wade C. Tang, Hal J. Rosen, William G. Golden, Hajime Seki, Charles A. Brown, and Mattanjah S. de Vries. Vibrational raman and infrared spectra of chromatographically separated C_{60} and C_{70} fullerene clusters. Chemical Physics Letters, 179(1):181 – 186, 1991.

[128] W. Krtschmer, N. Sorg, and Donald R. Huffman. Spectroscopy of matrix-isolated carbon cluster molecules between 200 and 850 nm wavelength. Surface Science, 156:814 – 821, 1985.

[129] Daniel Forney, Jan Fulara, Patrick Freivogel, Michael Jakobi, Daniel Lessen, and John P. Maier. Electronic absorption spectra of linear carbon chains in neon matrices. I. C_6^-, C_6, and C_6H. The Journal of Chemical Physics, 103(1):48–53, 1995.

[130] J. Bernholc and J. C. Phillips. Kinetics of cluster formation in the laser vaporization source: Carbon clusters. The Journal of Chemical Physics, 85(6):3258–3267, 1986.

[131] Jan ML Martin, Jamal El-Yazal, and Jean-Pierre François. Structure and vibrational spectra of carbon clusters C_n (n= 2–10, 12, 14, 16, 18) using density functional theory including exact exchange contributions. Chemical physics letters, 242(6):570–579, 1995.

[132] A Van Orden, RA Provencal, FN Keutsch, and RJ Saykally. Infrared laser spectroscopy of jet-cooled carbon clusters: The ν_5 band of linear C_9. The Journal of chemical physics, 105(15):6111–6116, 1996.

[133] A. O'Keefe, M.M. Ross, and A.P. Baronavski. Production of large carbon cluster ions by laser vaporization. Chemical Physics Letters, 130(1):17 – 19, 1986.